Fall 12-2021

Protection and Disturbance Mitigation of Next Generation Shipboard Power Systems

Marounfa Djibo
Old Dominion University, marounfad@gmail.com

PROTECTION AND DISTURBANCE MITIGATION OF NEXT GENERATION SHIPBOARD POWER SYSTEMS

by

Marounfa Djibo
B.S. May 2010, University of South Alabama
M.S May 2013 University of South Alabama

A Dissertation Submitted to the Faculty of
Old Dominion University in Partial Fulfillment of the
Requirements for the Degree of

DOCTOR OF PHILOSOPHY

ELECTRICAL AND COMPUTER ENGINEERING

OLD DOMINION UNIVERSITY
December 2021

Approved by:

Chung Hao Chen (Director)

Paul Moses (Co-Director)

Isaac Flory (Member)

Chunsheng Xin (Member)

Shu Xiao (Member)

ABSTRACT

PROTECTION AND DISTURBANCE MITIGATION OF NEXT GENERATION SHIPBOARD POWER SYSTEMS

Marounfa Djibo
Old Dominion University, 2021
Director: Dr. Chung Hao Chen

Today, thanks to modern advances mainly in the power electronics field, megawatt-level electric drives and magnetic levitation are being integrated into the marine power grids. These technologies operate based on Direct Current (DC) power which require Alternating Current (AC) to DC conversion within the current grid. Medium-voltage Direct Current (MVDC) and Flywheel Energy Storage Systems (FESS) are the next state-of-the-art technologies that researchers are leaning on to produce, convert, store, and distribute power with improved power quality, reliability, and flexibility. On the other hand, with the extensive integration of high-frequency power electronic converters, system stability analysis and the true system dynamic behaviors assessment following grid disturbances have become a serious concern for system control designs and protection.

This dissertation first explores emerging shipboard power distribution topologies such as MVDC networks and FESS operation with charge and discharge dynamics. Furthermore, the important topic of how these systems perform in dynamic conditions with pulsed power load, faults, arc fault and system protection are studied.

Secondly, a communication-based fault detection and isolation system controller that improves upon a directional AC overcurrent relay protection system is proposed offering additional protection discrimination between faults and pulsed-power Load (PPL) in MVDC

systems. The controller is designed to segregate between system dynamic short-circuit fault and bus current disturbances due to a PPL.

Finally, to validate the effectiveness of the proposed protection controller, different bus current disturbances are simulated within a time-domain electromagnetic transient simulation of a shipboard power system including a PPL system operating with different ramp rate profiles, pulse widths, peak powers, and fault locations.

This overarching goal of this work is to address some of the critical issues facing the US Navy as warfighter mission requirements increase exponentially and move towards advanced and sophisticated pulsed power load devices such as high energy weapon systems, high energy sensor and radar systems. The analyses and proposed solutions in this dissertation support current shipbuilding industry priorities to improve shipboard power system reliability and de-risk the integration of new power system technologies for next generation naval vessels.

Co-Director: Dr. Paul Moses

This dissertation is dedicated to my parents

ACKNOWLEDGEMENTS

My deep gratitude is first given to the almighty God for bestowing his mercy and blessing on me with success and with the erudition of several people whose constant assistance, guidance, and encouragement held me up throughout this endeavor.

I would like to express my sincere appreciation to my advisor, Prof. Paul Moses, for his endless support and help. His immense knowledge, guidance and patience inspired the completion of this dissertation. I am very humble and grateful for having the opportunity to work with him.

My deep appreciation also goes to my graduate program committee members: Prof. Chung Hao Chen, Prof. Isaac Flory, Prof. Chunsheng Xin, and Prof. Shu Xiao for their tremendous support, help and valuable advice throughout the length of this dissertation.

I am very grateful to my company Newport News Shipbuilding for fully sponsoring the cost of my doctoral program. Many thanks go to members of the Newport News Shipbuilding company: CEO of the company, Mike Peter, company President, Jennifer Boykin, Department Manager, Russel Kyte, Department Supervisors, Tony Tillet, John W Edwards, AL Rea, & Ed Martin, supervisors. Special thanks also extended to my colleague, Jason Little, who assisted with editing throughout my writing process.

I would like to extend my sincere appreciation to my friends: Amadou Mounkaila Adamou, Seini Issaka Souley, Souleymane H Kimba, Soumail Saidou, and Issoufou Moumouni for your tireless support during this effort.

Great acknowledgment is extended to Dr. Mahammad El-sharkh for his guidance and coaching during my earlier research, Dr. Abdelmageed El-Moustafa for providing his guidance, and support throughout this dissertation. To the greatest professor, advisor, and mentor, Dr. Arifur Rahman, may you rest in peace I cannot thank you enough. Your assistance and guidance will remain in me for the rest of my life.

Last but not least, I would like to thank my beloved wife, Nadia H Oumarou, for being present when I needed her the most, your love, compassion, and tireless physical and moral support have carried me up throughout the course of this work. I also thank you for sparing time to read this dissertation entirely and edit it to the best of your ability. To my beautiful little princesses Mouhanna and Assiah, my parents, my brothers and sisters thank you for your devotion, patience, care and endless support. I am very grateful to my father, Djibo Dourfaye, for believing in me, your tremendous financial, mental, and physical support has finally paid off. Your prayers convolved with my dearest mother, Nana Aissata Mahaman, prayers have brightened my future. Mom, words cannot describe or express your tremendous support and love, from the bottom of my heart I thank you and I praise the almighty for making me one of your sons.

NOMENCLATURE

AC	Alternating Current
AIS	Artificial Immune System
ARM	Arc Resistance Method
ATG	Auxiliary Turbo Generator
AVM	Average-Value Modeling
BESS	Battery Energy Storage System
CS	Cable Section
DC	Direct Current
D-Q	Park Transformation
E	stored kinetic energy
EI	Energy Incident
EMC	Electromagnetic Compatibility
EMI	Electromagnetic Interference
ESD	Energy Storage Device
ESS	Energy Storage Systems
FESS	Flywheel Energy Storage system
FFL	Feed-Forward Loop
J	Moment of Inertia
KCL	Kirchoff's Current Law
KVL	Kirchoff's Voltage Law
LIFP	Local Information-based Fault Protection

LVAC	Low Voltage Alternating Current
MG	Motor Generator
MPM	Maximum Power Method
MTDC	Multi-Terminal DC
MTG	Main Turban Generator
MVDC	Medium voltage Direct Current
NFPA	National Fire Protection Association
OCR	Overcurrent Relay
PCM	Power Conversion Module
PGM	Power Generation Module
PID	Proportional Integral Derivative
PMSM	Permanent Magnet Synchronous Generator
PPL	Pulsed-Power Load
PPM	Propulsion Motor Module
PPT	Pulsed-Power Technoloy
PWM	Pulsed Width Modulation
RMS	Root Mean Square
SCES	Super-Capacitor Energy Storage
SMES	Superconducting Magnetic Energy Storage
SSCB	Solid State Circuit Breakers
SWB	Switchboard
IEC	International Electrotechnical Commission
I_t	Transition Current

TCCC	Time-Current Characteristic Curve
TCR	Thyristor Controlled Rectifier
TMS	Time Multiplier Setting
UPS	Un-interruptible Power Supply
VSC	Voltage Source Converters

TABLE OF CONTENTS

LIST OF TABLES

LIST OF FIGURES

CHAPTER 1

INTRODUCTION

1.1 SHIPBOARD POWER SYSTEM

Marine power has seen a significant paradigm shift in supplying electrical power to naval vessels as capability requirements have more demanding applications for new and dynamic hotel and propulsion loads for next generation of ships. The generated energy is expected to supply variable loads such as propulsion drives, propulsion monitoring and control systems, high energy sensors, radar, weaponry, and pulsed-power systems. Conventionally, these loads are interfaced with a transformer for galvanic isolation and/or impedance or voltage scaling. Even though these transformers are vital for both classical and modern marine power distribution systems, their size and weight represent a big concern for proper ship operation in terms of boat stability, limited compartment space and hydrodynamic performance [1].

Depending on the application, different Energy Storage Devices (ESD) such as: batteries, capacitors, flywheels suitable for high power-density application, and super-capacitors can be used to maintain power stability. A Flywheel Energy Storage System (FESS) stores energy mechanically and is suitable for high power-density application such as pulsed-power. When compared to batteries, flywheels require less energy to stay charged and to be cooled where batteries require air conditioning to avoid thermal instabilities, which is especially critical in emerging lithium-based battery technologies. Electromagnetic Launch System requirements on an ESD are low impedance, long discharge times, and a large amount of stored energy [2]. Consequently, a suitable energy storage element for a launch system will be inductive because it stores its energy in the form of magnetic field. New developments have revealed that the integration of an ESD into an electrical power system can have a positive impact on the overall system stability and efficiency [2], [3]. The stored energy can be used in the form of a spinning reserve to compensate for sudden peak demands [4] above generator capabilities.

On the other hand, historically, particularly during the 20th century, Edison's push for DC generation, distribution and utilization lost the battle against Westinghouse and Tesla's AC electrical system. Back then, it was discovered that DC circuit breakers, unlike AC circuit breakers cannot make use of zero crossing points to assist in clearing faults, and therefore must be oversized to do the same duty as its equivalent AC circuit breaker. Furthermore, DC distribution systems lacked protection which capped its distribution system to 1000 v ratings on naval vessels. Today, thanks to modern advances mainly in the power electronics field, electric drives and magnetic levitation are being integrated into the marine power grids. These innovations operate based on DC power which, depending on the grid type, may require a power conversion module within the existing grid. In addition, more low-level end DC load users have evolved including combat systems, computer control equipment in many subsystems, lighting, heating, and many others which raise the question of AC marine power systems becoming obsolete. To address these issues a re-evaluation of future shipboard power grid layouts and current installation practices is inevitable [5].

DC networks, which serves as a platform for many DC based processes [6] and an additional layer of infrastructure between the transmission and distribution systems has attracted the attention of many researchers. Its implementation not only facilitates the integration of renewable energy and energy storage into the shipboard power grid, but also aims to increase the reliability, efficiency, and reduction in weight from dispensing with bulky AC equipment such as transformers. Low level consumer units may need to use dedicated power conversion modules on demand basis. These new paradigm shifts in shipboard applications are migrating away from the established knowledge and experiences in conventional AC distribution system design. Therefore, significant work is needed to understand and de-risk these new design evolutions especially considering the integration risks and complex interactions of these power conversion modules and energy storage behavior with new dynamic behavior and fault signatures.

1.2 DISSERTATION AIMS

Shipboard power systems can be considered as micro grids due to their size and limited number of fixed generators. Despite the many advancements in power systems over the past century, the old legacy AC system is still the most prevalent in both the terrestrial and marine power fields. This dissertation aims to address the question of how future shipboard power system architectures should be developed for improved system dynamic response with emerging energy storage requirements and fault protection. Moreover, it also aims to highlight and propose a solution to some of the outstanding challenges that have been left out in the literature concerning FESS operation and Medium Voltage DC (MVDC) systems during dynamic transient disturbances.

1.3 RESEARCH OBJECTIVES

In Chapter 2, a comprehensive literature review on FESS and shipboard MVDC is discussed. The prevalent applications and features are described for power systems ranging from medium to high power (kW to MW) where energy discharges within a short period are necessary. The potential technological challenges and features of the widely used Low Voltage AC (LVAC) distribution in ships migrating towards MVDC are discussed.

In Chapter 3, a FESS model based on a permanent magnet synchronous machine mathematical equation were derived using a Direct-Quadrature (D-Q) rotational reference frame transformation. The FESS problem formulation and control strategy is explained in order to develop a better understanding of the system performance.

In Chapter 4, the proposed shipboard FESS and MVDC systems were implemented and demonstrated in the MATLAB Simscape package. In the FESS system, a mechanical discharge/charge mechanism is implemented in the design. In addition, a shipboard MVDC system is simulated, and a variety of DC bus fault dynamics were studied through different case scenarios. The intent of this chapter is to provide a clearer understanding of potential issues that may impact the design of future system protection and fault mitigation strategies.

In Chapter 5, a novel communication-based fault detection and isolation system controller that improves upon a directional ac overcurrent relay protection system is proposed offering additional protection discrimination between faults and Pulsed-Power Load (PPL) in MVDC systems. The controller is designed to segregate between system dynamic short-circuit fault and bus current disturbances due to a PPL.

In Chapter 6, the main conclusions of the dissertation are drawn, and future work and research directions are discussed.

CHAPTER 2

A CRITICAL REVIEW OF SHIPBOARD POWER SYSETEMS

2.1 INTRODUCTION

This chapter presents a critical review of key emerging technologies and technical barriers in the next generation of shipboard power systems. Firstly, a leading energy storage technology most viable for shipboard power systems operating with highly dynamic pulsed-power loads, the FESS, is discussed. In conjunction with this, the evolutionary trends of traditional low voltage AC shipboard power system architectures to medium voltage and DC networks are also examined. An important technological barrier of protecting the power system from faults and transients considering these new developments is assessed. These topics are interrelated and are of fundamental importance in achieving more resilient and flexible shipboard power system performance in future warfighters.

2.2 AN OVERVIEW OF SHIPBOARD POWER TOPOLOGIES

Unlike traditional terrestrial-based utility grids, shipboard power system is isolated and distributed over a short distance with fewer power generation resources. In this section, the most common shipboard power system architectures are reviewed. These architectures can be categorized into three groups: radial, ring or zonal distribution systems.

2.2.1 Radial Distribution System

In this distribution system, electrical power is radially distributed from a single connection node. In almost every electrical distribution architecture, there is always some portion that exhibits radial distribution. For instance, on the DDG 51 class ships, the radial distribution point starts at either a switchboard, or a load center. This way, the closer the central access point, shorter cables are needed to feed larger loads [7]. Figure 1 below, displays a Cruise ship radial distribution system. These type of distribution systems are simplest from a protection system coordination point of view. As it can be seen below, the fault current can only have one direction and one source, unlike a ring or a zonal bus system.

In [8], Weibull probability density function is applied to a radial "utility grid" distribution system to analyze system transformers failure rate. The expected cost of interruptions of these failure rates were then computed using survey data obtained from four diverse consumers. Based on the interruption cost and the energy not served rate of the transformers, the authors suggested a schedule maintenance and replacement timetable for these transformers to boost the reliability of the radial distribution system.

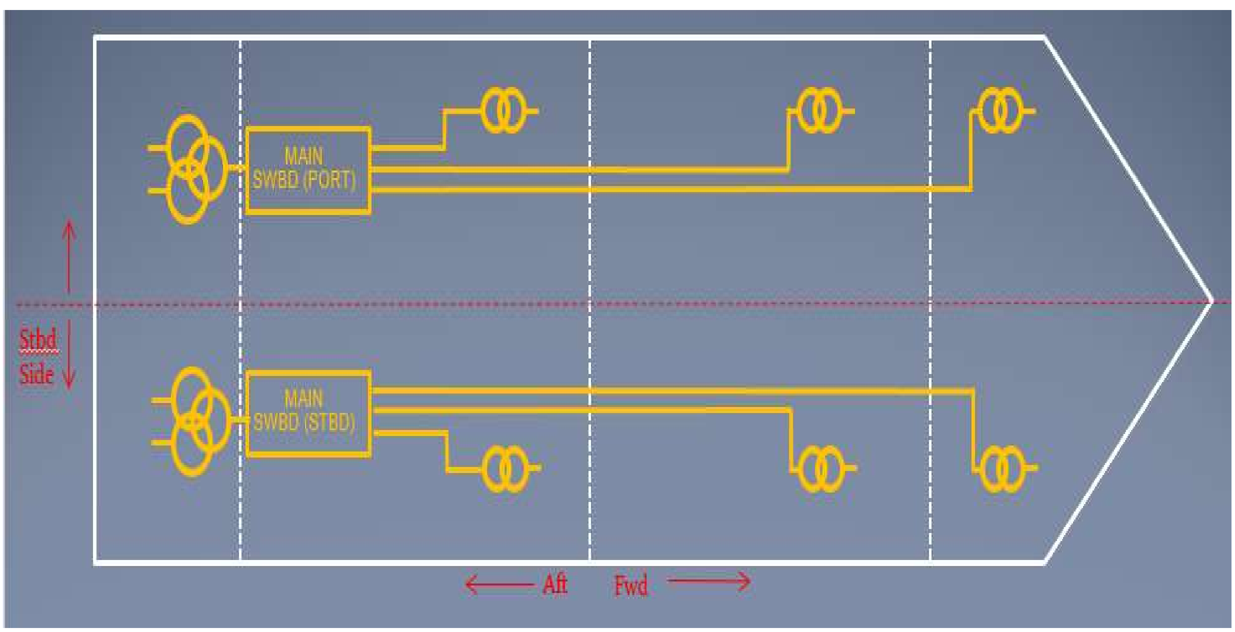

Figure 1: Radial Distribution System

2.2.2 Ring Bus Distribution System

The aim of this distribution technique is to form a solo main power bus loop as shown in Figure 2. This implies that a load can receive power from multiple generators using different paths, thereby improving the redundancy and reliability of the system. This technique is used on the DDG 51 class ships and the cruise liners. In these types of distribution systems, the fault protection coordination is complex because a fault can be fed from multiple sources and from two directions.

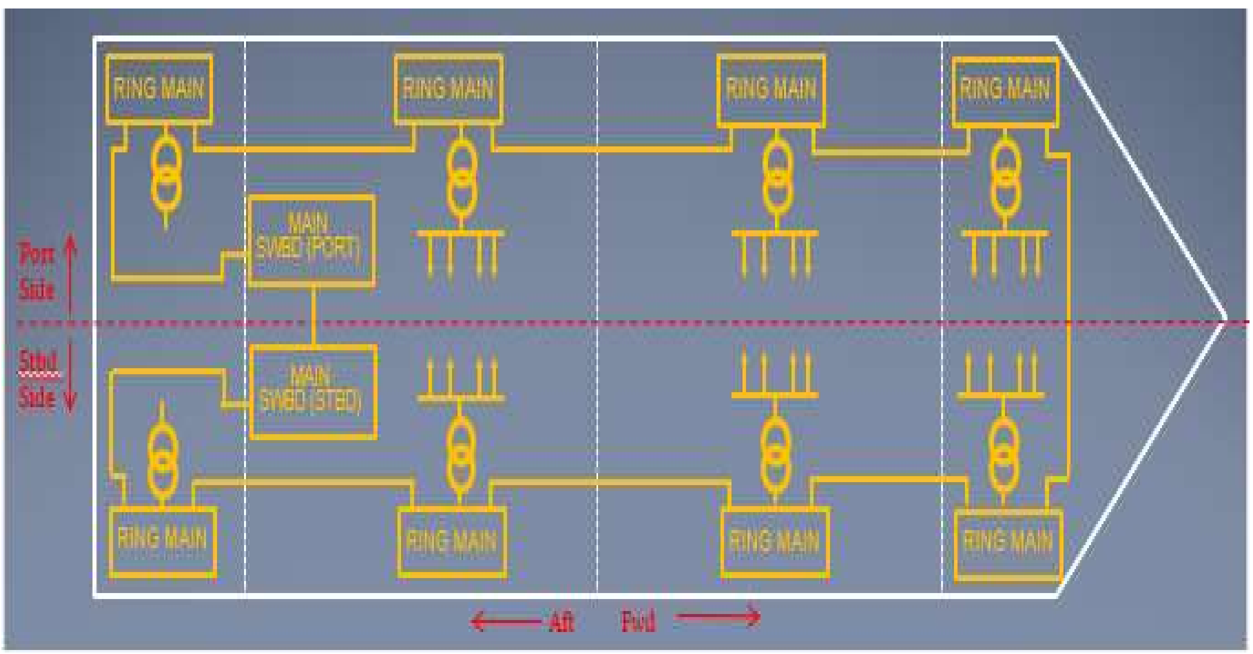

Figure 2: Ring and Zonal Distribution System

2.2.3 Zonal Distribution System

This system consists of having two parallel load buses running longitudinally along the port and starboard side of the ship with one above the water line and the other below it. The advantage of this configuration is that it can be configured as a radial or ring configuration. However, to maintain survivability using zonal distribution system, a redundant alternate power source path is required. In [9], to reduce the AC-DC zonal distribution power loss as shown in Figure 3, the switch between the common bus and the power supply is removed and three switches were placed between the converters of each zone. According to the authors, the probability of power loss in one zone is decreased by a factor of 1/3rd. This technique can also be seen as a hybrid technique. The removal of the switch between Power Supply PS1 and PS2 lead to a closed loop which is a ring configuration.

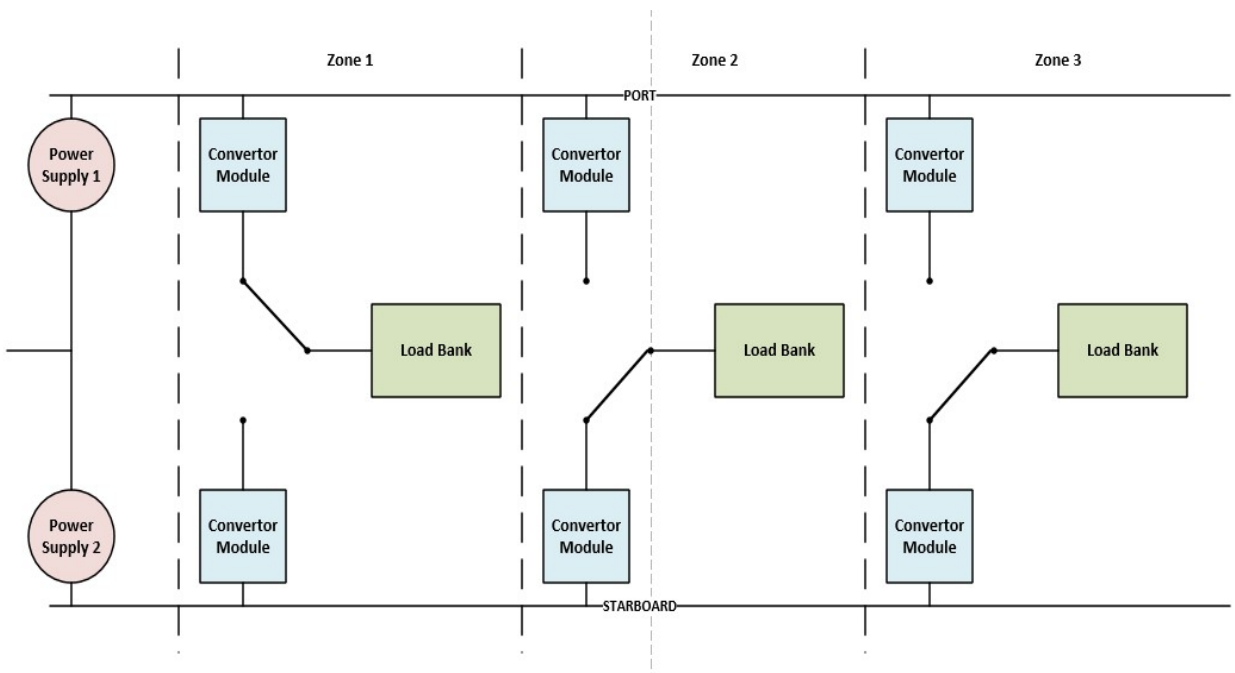

Figure 3: Zonal Distribution System

Consequently, any transients on any of the distribution system models can impact the entire system. Furthermore, critical loads such as close-in weapon systems, medical and dental operation rooms, fire control, radar systems, boilers, cooling pumps and feed pumps, and computers are of grand importance for ship survival during battle. Any voltage interruption or transient due to a pulsed load or fault during operation can hinder ship operation. However, because the system has deeper redundancy, it exhibits even more complexity in the protection design compared to the radial and ring bus topologies.

2.3 ENERGY STORAGE FOR SHIPBOARD POWER SYSTEMS

Pulsed-Power Technology (PPT) is prevalent in many industries and used in a variety of applications. In the medical field, PPT is extensively used in power supplies for linear accelerators and X-ray diagnostic machine sets requiring high energy discharge of electromagnetic radiation. An interesting application of the use of pulsed-power is in the food industry, which uses PPT to generate pulsed electric fields for neutralizing microorganisms, bacteria, and pathogens in liquid foods. Material sciences have also made important uses of PPT for high precision ablation of thin-film manufacturing. In the maritime domain, PPT is becoming an important issue in shipboard power systems for supplying high-powered radar systems, directed-energy weapons technologies and electromagnetic aircraft launching systems. This has precipitated research on many fronts to improve upon conventional shipboard power system designs for increased resiliency in next generation warfighters with PPTs operating in harsh combat conditions. The most important aspect of integrating PPTs into a shipboard power system is managing the large delivery of energy in a very short time. Therefore, high ramp-rate energy storage is necessary to meet future PPT requirements which cannot be met by slow responding conventional generator sets.

2.3.1 Battery Energy Storage System (BESS)

Batteries are generally differentiated by their electrolyte and electrode characteristics. These characteristics enable batteries to have high energy density, affordable design cost, high pollution rate, short life, and low efficiency when compared to other ESD. BESS consists of 1) a battery that converts electrical energy into chemical energy, 2) a power electronic that converts between AC to DC for charging and discharging energy, and 3) a control system for battery management. In [10], a battery-inductor pulsed power system was proposed to provide energy to a "conceptual 2-MJ muzzle energy Electro-Magnetic Launch System (EMALS)."

In [11], a BESS is proposed to reinforce wind plant system reliability and efficiency by providing voltage and frequency support. During wind plant operation, voltage and frequency may deviate due to wind intermittency. Integrating BESS in the smart power grid allows a fast response to the deviation by having the BESS output power to operate in a manner similar to that of a droop control. For utility application, battery capacities in the single-digit megawatt-hour range have been recently commissioned in some countries such as Australia. These are not quite in the range of PPT duty cycles but are still required to compensate power fluctuations in the same time scale. The difference between this application and PPTs is that the latter application is likely to completely discharge the ESD upon use, which is not ideal for batteries. While large-scale batteries have progressed from lead-acid to lithium-based chemistry, there is a risk of thermal runaway issues and excessive life-cycle loss if applied to highly demanding PPT profiles. Therefore, this technology is not yet mature enough for shipboard military applications.

2.3.2 Super-Capacitor Energy Storage (SCES)

Originally known as a condenser because of their ability of storing high density energy, a capacitor consists of two conductors separated with a non-conductive region or dielectric. Capacitances in the super or ultra-capacitor range vary from about 10 F to 3400 F. These ESDs may have different series-parallel arrangements when matching requirements for the high current/ high voltage ratings of the system.

Compared to the BESS, capacitors have a long cycle life, long energy storage time, fast recharge-discharge cycles, less maintenance, but low energy density. In [12], a 35kJ/s 25kV capacitor charger was designed based on a 3-phase resonant inverter, and an air-insulated transformer. Based on the experiment results, the authors, claimed that the use of an air-insulated transformer on the proposed technique has improved the stability and maintenance of the capacitor charger. Furthermore, they claimed that the proposed technique has a simple structure, low cost, and ease to control. For naval applications, however, the technology is deemed not technologically ready because of material reliability issues.

2.3.3 Superconducting Magnetic Energy Storage (SMES)

Unlike capacitors, which have an upper limit on voltage due to dielectric breakdown limiting their storage capacity, inductors are mainly limited by magnetic saturation in the steel core. This can result in at least 15,000 times greater energy storage density than is achievable in capacitor technology. A coil wound in air with no magnetic steel theoretically has no saturation limit. The higher the coil current, the more energy that can be stored in the field. In a conventional inductor or reactor, the coil current and Joule I^2R heating impose a thermal limit. However, if the resistance could be eliminated using superconductors (Figure 4), SMES can achieve very high levels of energy storage [13]. SMES has reached the prototype stage in terrestrial utility applications. However, the extra engineering to achieve super-cooling below the critical temperature imposes high cost and reliability issues for it to be suitable in shipboard applications. Nonetheless, the navy is still pursuing research along these lines in the hopes of maturing the technology for improved resilience for PPT applications.

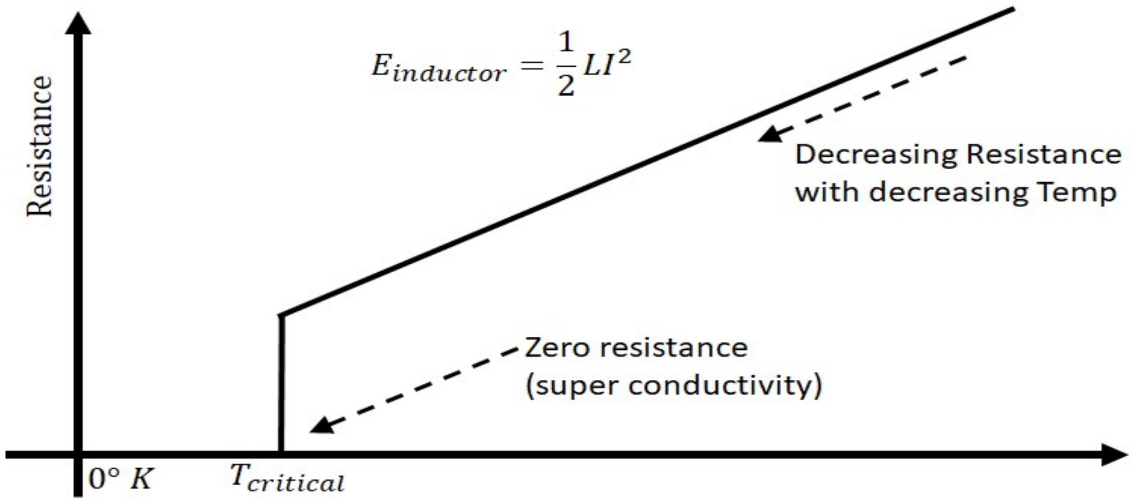

Figure 4: Superconductivity Characteristic in an Inductor

2.3.4 Flywheels Energy Storage System (FESS)

Flywheels were initially used to smooth out rotor speed fluctuations and to supply mechanical energy. Later, it was discovered that coupling the flywheel with a power electronic converter and an electrical machine can lead to a fast energy storage source [14], [15]. FESS generally consists of a rotating flywheel mass that stores kinetic energy spinning up to tens of thousands of rpms. The assembly is mounted on magnetic bearings to reduce friction loss in maintaining the flywheel in standby charged state. A power electronic converter is used to charge the flywheel by motoring it to high speeds and then later extract the kinetic energy by changing into regenerative braking mode as shown in Figure 5. FESS has been used to provide voltage and frequency support, power leveling and smooth AC power transmission [16]. During operation, energy is stored in the flywheel whenever the power supply exceeds power demand, and energy is supplied from the flywheel when the demand exceeds the supply to compensate for the difference. Flywheels have been used for low-speed applications where the stored energy is required over a longer period such as an Un-interruptible Power Supply (UPS), as well as for high-speed application where high density of energy is required over a short time. Flywheels have the unique advantage of having virtually no environmental effect. The consensus in the naval community is that FESS is the most matured technology in terms of reliability and simplicity to be a candidate for supporting PPTs such as high-powered radar or directed energy weapons.

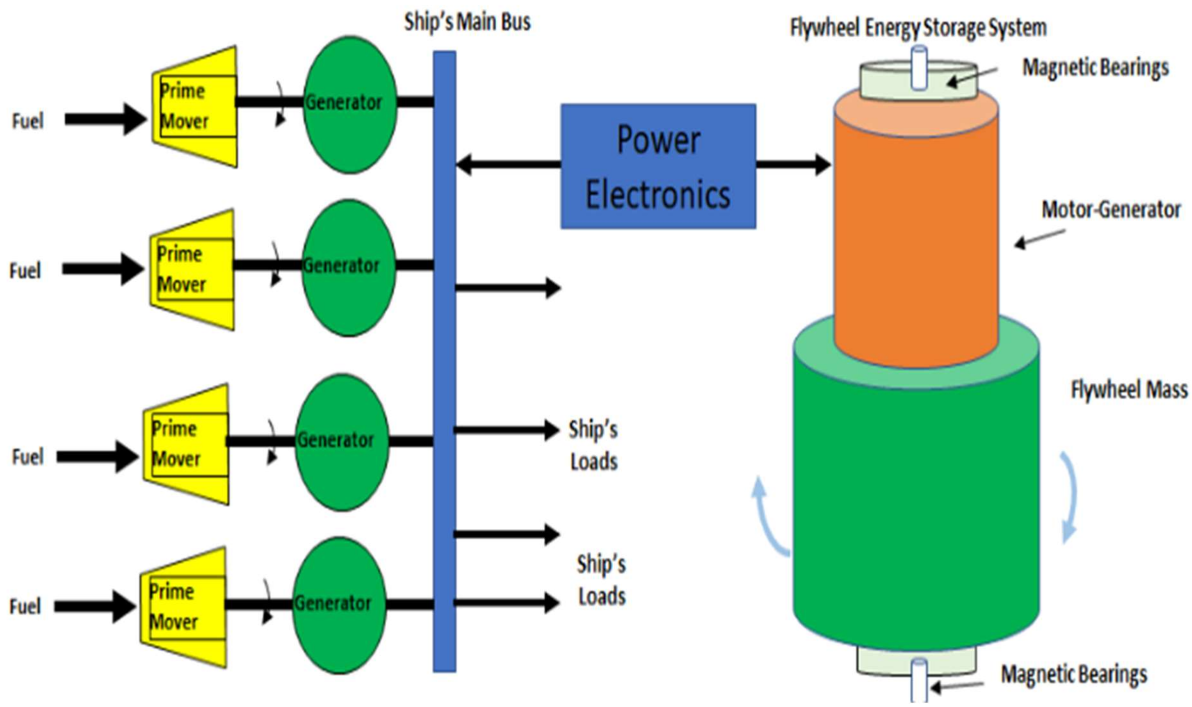

Figure 5: An Example of a Shipboard Flywheel Energy Storage System

To maximize ship survivability during combat, the US Navy is looking into effective ways to mitigate voltage sags [17]. One way is to compensate for voltage sags by using Energy Storage Systems (ESS).

2.4 FLYWHEEL ENERGY STORAGE SYSTEM

The concept of the Flywheel Energy Storage System (also known as "FESS") can be traced back several hundred years. As an example, the potter's wheel that uses stored mechanical energy to aid in the shaping of earthenware as described in [18]. However, the word "flywheel" was introduced at the beginning of industrial revolution. During that time, the iron-based flywheel design replaced the wood-based flywheel. Soon enough, flywheel utilization expanded to other applications such as steam engines, trains, and energy accumulators in factories [19]. Years later, there became a growing interest with the possibility of being able to increase the amount of kinetic energy that the FESS could store rather than its speed. This possibility would attract the attention of many researchers.

During the 1960's, it was discovered that when power electronics are coupled to an electrical machine and a flywheel, a new technique of energy storage can be obtained [20], [21]. This is achieved by using the power electronics to control the frequency [22] and amplitude of the voltage. The emergence of composite materials [23], [24] and magnetic bearings technologies [25], [26] during the same era have resulted in an increase of the density of energy that can be stored [27].

2.4.1 Overview of Flywheel Energy Storage System Theory

A FESS stores energy based on a rotating mass principle. It is a mechanical energy storage device, which imitates an electrical energy storage device. FESS stores energy in the flywheel in the form of kinetic energy. During the charging (motoring) mode, input power or excess power is supplied to the FESS. The excess power is the difference between the generated and demanded power from either a grid or another source of electrical energy. The charging mode is also characterized by an increase in the speed of the flywheel, which will then saturate when the maximum speed is reached. On the other hand, the discharging (generating) mode of the FESS will be a deceleration in the speed of the flywheel. The discharging mode is generally triggered when the demand power exceeds the generated power [20], [21].

2.4.2 Elements of a Flywheel Energy Storage System

A FESS consists of a rotor, motor/generator (MG), rotor bearings, power electronics, controllers and a housing as shown in Figure 6. These components constituents are vital for effective extraction and releasing of the stored kinetic energy. A brief description of each subsystem component is given below.

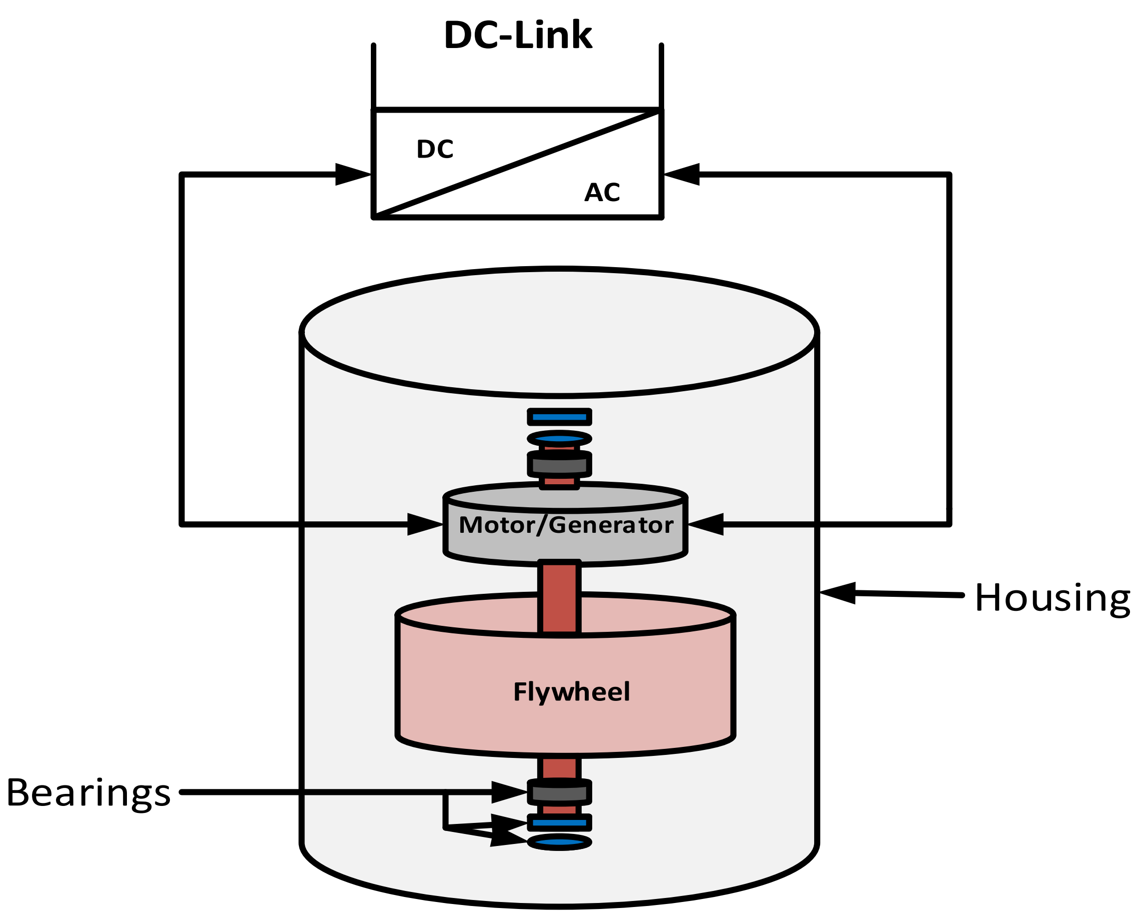

Figure 6: Flywheel Energy Storage System Assembly

2.4.2.1 FESS Rotor

The kinetic energy stored in a flywheel depends on the shape and material of the rotor. The rotor consists of a hub, the motor rotor, and the rim. The mass of the rotor is concentrated on the rim and represents the energy storage element [28]. The amount of stored kinetic energy is linearly proportional to the rotor moment of inertia and its angular speed as shown in Equation (1) [29],

$$E = \frac{1}{2} J\omega^2, \tag{1.1}$$

where *E* is the stored kinetic energy, *J* is the moment of inertia and ω is the angular speed. The useful stored energy which is the energy obtained between the minimum and maximum rotational speed is given by Equation (2),

$$E = \frac{1}{2} J({\omega_{max}}^2 - {\omega_{min}}^2) = \frac{1}{2} J{\omega_{max}}^2 \left(1 - \frac{{\omega_{min}}^2}{{\omega_{max}}^2}\right), \tag{1.2}$$

The moment of inertia of the rotor depends on the geometry and mass of the flywheel as shown in Equation (3),

$$J = mr^2, \tag{1.3}$$

where *m* is the mass of the rotor and *r* is the outer radius.

Taking into consideration the tensile (σ) of the material used in the design of the flywheel, as shown in Equation (4), the stored energy can be rewritten as in Equation (5):

$$\sigma = \rho r^2 \omega^2, \tag{1.4}$$

$$E = \frac{1}{2} m \frac{\sigma}{\rho}, \tag{1.5}$$

where ρ is the material density.

From Equation (5), an increase in the σ and a decrease in the ρ increase the amount of energy that the flywheel can store. In [30], it is stated that composite material with a high $\frac{\sigma}{\rho}$ ratio can significantly increase the speed of the flywheel. As a result, the capacity of energy stored within the system will increase. In [31], an assessment was conducted on the maximum specific energy (energy per mass unit) between metals and composite materials used in the flywheel design based on Equation (5). The specific strength of both metals and composite materials were analyzed first. Based on material properties, metal materials such as Carbon Steel, Aluminum Alloy, Titanium Alloy and Maraging Steel were found to have specific energies of 12, 46, 63 and 66 Wh/kg respectively. Composite materials such as unidirectional Glass, Kevlar and Graphite reinforced plastics were found to have specific energies of 180, 230, and 240 Wh/kg respectively. Thus, composite based flywheels have 4 to 5 times higher specific energy than metal-based flywheels. In [32], an exhaustive study was performed on the specific energy and energy density (energy per volume unit) of a flywheel as shown in Equation (6) and Equation (7),

$$\frac{E}{m} = k \frac{\sigma_{max}}{\rho} \left[\frac{J}{kg}\right], \tag{1.6}$$

$$\frac{E}{V} = k\sigma_{max} \left[\frac{J}{m^3}\right], \tag{1.7}$$

where k is the flywheel shape factor and a measurement of the flywheel material utilization as shown in Figure 7.

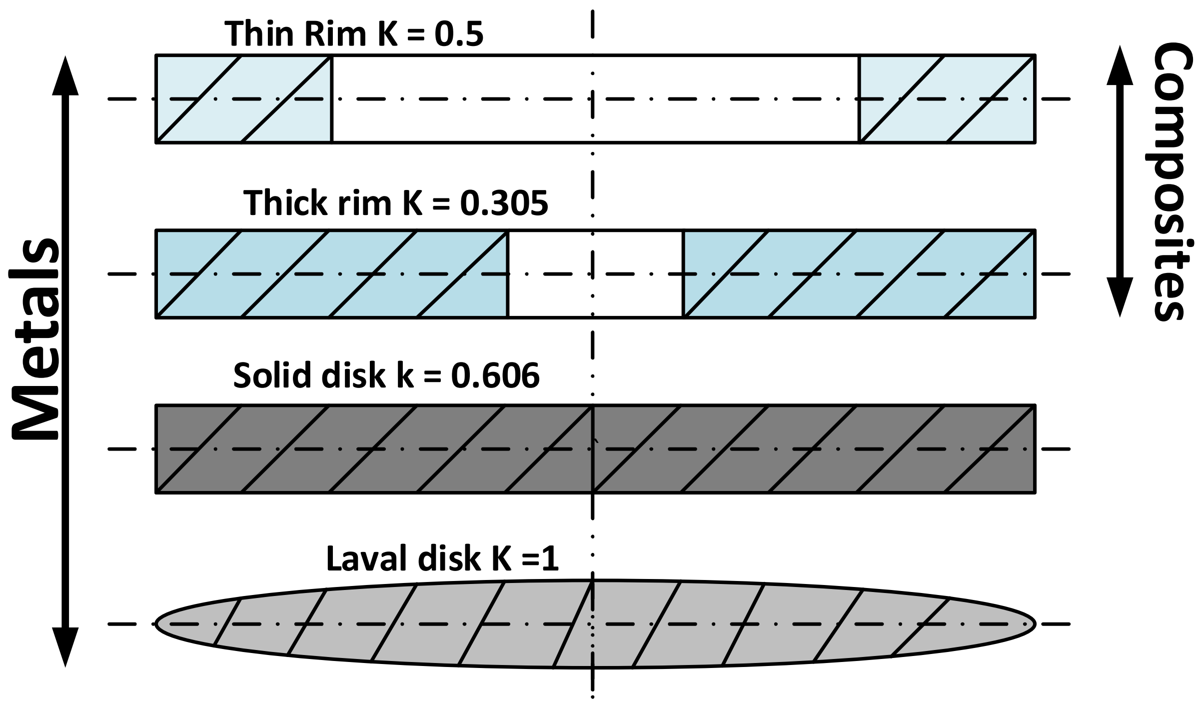

Figure 7: Different Types of Flywheel Cross Sections

From Equation (1), energy stored in a flywheel can be increased by choosing a mass with a larger moment of inertia which was discussed above through the tensile and density ratio. The stored energy can also be improved by increasing the angular speed. The literature has presented two basic schemes of FESS operation based off the angular speed range application. For low-speed applications generally with a speed range of 10,000 rpm or less, metallic materials are used in the rotor design as discussed above [33]. These rotors are then supported by classical or in some cases magnetic bearings [25], [26]. Their low speed is the result of the material and type of bearing used in their design. Low speed flywheels are seen in applications where stored energy needs to be discharged over a long period of time for components such as un-interruptible power supplies

[33], [34]. On the other hand, high speed flywheel rotors with speeds that range from 10,000 RPM up to 100,000 RPM are made of composite material as exemplified above. The rotors are then supported with either magnetic or superconducting bearings which makes the whole assembly compact [35]. High speed flywheels are seen in applications that require energy to be discharged over a short period of time [34], [36].

Comparing the losses in the rated power, it was stated in [35] that between 0.5% to 1% of rated power is lost with low-speed flywheels. On the other hand, only 0.1% of the rated power can be lost with high-speed flywheels. In [36], [37], it is stated that high speed flywheels cost more than low speed and require more maintenance.

2.4.2.2 FESS Motor-Generator (MG)

As stated earlier, a machine is coupled to a flywheel to allow energy to be stored in the form of kinetic energy. Furthermore, when energy is being stored in the flywheel, the system behaves as a motor, and when energy is being extracted, the system behaves as a generator. According to the literature, different machines can be used in FESS design.

Permanent Magnet Synchronous Machines (PMSM) are known for their high energy density because of their sturdy rotor design and low rotor flux losses. As a result of these qualities, their efficiency is very high [25], [31], [38], [39]. PMSMs are mostly used in high-speed applications [38]. The main draw backs with the PMSMs are their high cost and idle losses due to the stator eddy current [39], [40].

In [41], a novel flywheel array energy storage system with Series Connection PMSMs is proposed to enhance the stored energy capacity. Traditionally, to boost the voltage capacity, FESS units are connected in parallel. In this novel technique, according to the authors, both the power level as well as the voltage ratings could be increased to accommodate variable systems.

Induction Machines (IM) are seen in high power applications such as wind turbines because of their higher torque and ruggedness. To enable power smoothing in wind turbine generation, IMs are being widely used in wind turbine applications [40]. The drawbacks with the IMs are higher maintenance requirements, complex control, and speed limitations [35]. Doubly Fed Induction Machines (DFIM) have emerged in the literature as a solution to the later machine control complexity and higher power conversion rating [35], [42].

2.4.2.3 FESS Power Electronic Converters

For FESS applications, two converters are generally used. A grid side converter (rectifier) is attached between the grid and the DC-link followed by the machine side converter (inverter). The converters play a vital role in the operation of the FESS. They are used for converting AC to DC and DC to AC voltage. Furthermore, they are used to rectify and maintain both the DC-link and AC voltage. This topology of the converters is called a Back-to-Back converter. Back-to-Back converters are the most used technique in FESS applications [31], [38], [42].

In [43], a flywheel fast charging energy storage system was proposed using an enhanced Artificial Immune System (AIS) to support a transportation electrification grid. The designed energy storage system aimed to avoid grid overload, handle peak power demand, and reduce system charging cost. During the process, a computational AIS is applied to the system Proportional Integral Derivative (PID) controller output error signal to tune and minimize its driving dynamic gains. The effectiveness of the proposed algorithm when compared to the traditional technique yield an improved performance handle grid dynamic transient.

2.5 SHIPBOARD MVDC POWER SYSTEM

MVDC power systems are being heavily considered by the U.S. Navy for the next generation of ships for many reasons. A generic MVDC power system that displays a zonal distribution system is shown below in Figure 8. The system is comprised of four power generation sources: two Main Turbine Generators (MTGs) and two auxiliary turbine generators (ATGs). These turbine generators serve as the four main power conversion units that convert the generated AC current to DC which feed into the main DC bus. DC to AC power electronics is also used to supply two propulsion loads and four zonal loads. Additionally, a DC-to-DC conversion unit is used to feed a pulsed load such as a radar system or solid-state laser armaments. The system is also equipped with DC switches and breakers to facilitate fault isolation. It is worth mentioning that these MVDC systems are yet to be built, thus there are no MVDC electric ships.

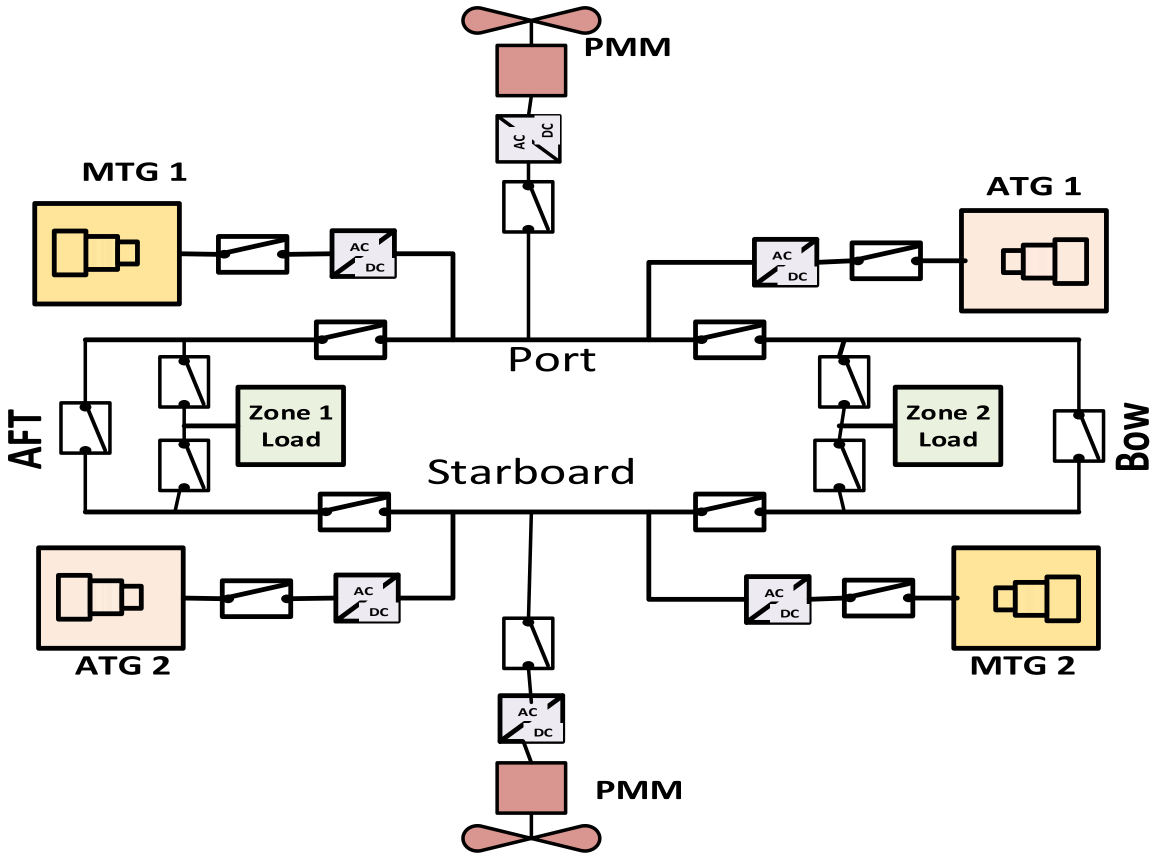

Figure 8: Shipboard MVDC Power System

2.5.1 Potential Benefits of Shipboard MVDC Systems

MVDC shipboard power distribution systems have amassed wide interest in the research community for realizing the next generation of "all-electric" naval vessels [44]. Some of the advantages of a DC micro-grid over an AC micro-grid are:

- Power systems are free of bulky high voltage transformers
- They require less stages of power conversion for loads connected to the DC bus [45], particularly, motor drive loads for propulsion, HVAC equipment, deck machinery, etc. [46], [47]

- They decouple the bond between the prime mover speed and the distribution bus frequency. Thus, the generator performance can be optimized for various types of prime movers without reduction or speed increasing gears. The restriction of the generator to a given number of poles is not of concern [48].
- DC current flows through the entire cable rather than the outer surface of the cable (skin effect) [49], which also results in cabling weight reduction.
- Electromagnetic Interference (EMI) and Electromagnetic Compatibility (EMC) requirements are reduced due to the absence of ac frequency components [48].
- Synchronization of generator sets is simplified [50] by not having to match their frequencies, phase rotation and AC phase angles. When paralleling generators with MVDC, only matching the voltage is required [48].
- Some studies show moderate fuel savings can be achieved when converting to DC distribution systems [50], [51]. Moreover, DC micro-grids are deemed to have higher energy density [52] and can deliver more power with lower losses than their AC counterparts [53].

On the other hand, when compared to an AC micro-grid, DC-grids are far away from technical readiness and maturity, particularly in the fault protection system aspects [54]. Overall, there are very few DC systems in use in terrestrial and marine applications to draw experience such as the underground railway traction systems and diesel-electric submarines. These are mostly in the low voltage range (less than 1000 volts) and do not carry the same complexity as the medium voltage situation.

2.5.2 MVDC Fault Protection

Even though DC distribution systems offer much better opportunities when compared to the counterpart AC systems, providing fault protection continues to be a great challenge [54]. In [55], for AC micro grids there is a standard Institute of Electrical and Electronic Engineers (IEEE) and International Electrotechnical Commission (IEC) fault protection system that can easily be used. However, current standards of protection on MVDC grids do not exist. The system lacks a standard of protection against ground faults, short-circuit faults and open-circuit faults for multisource and multi-terminal DC lines distribution systems.

For enhanced system protection and fault identification, it is important to review the fault current transient behavioral differences between AC and DC systems. In traditional AC distribution systems, the alternating current has a natural crossing transition through zero at every half cycle as shown in Figure 9. Fault extinction occurs when current transitions at that point during the opening of the circuit.

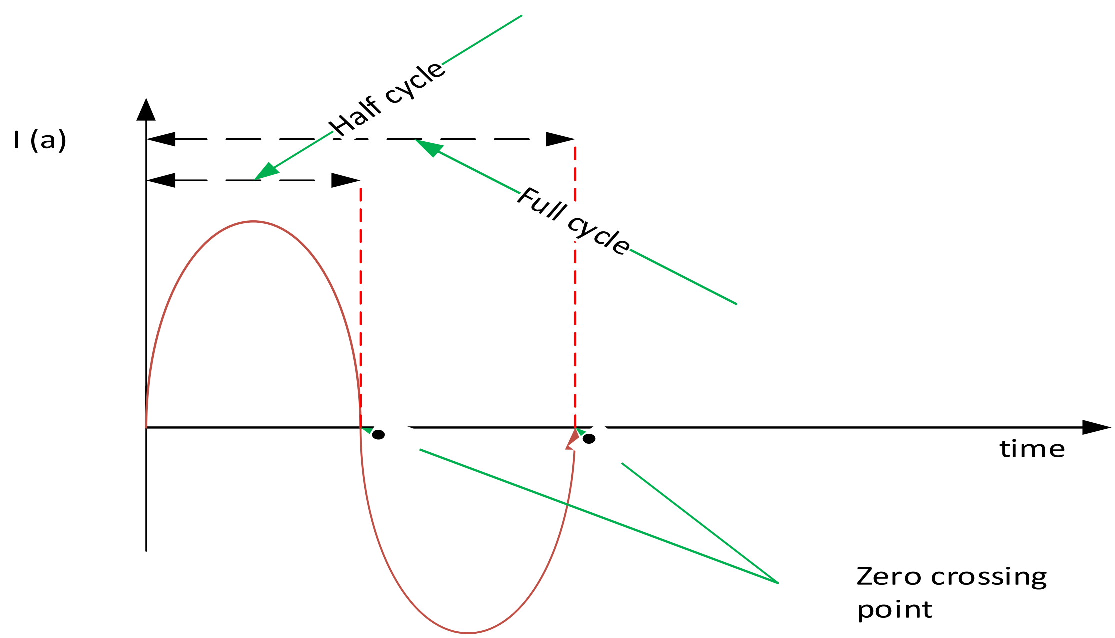

Figure 9: AC Sine Wave Showing the Zero-Crossing Point

In direct current distribution systems, zero crossing transition does not exist as shown in Figure 10. The main option is to force or decrease the current down to zero to secure a fault. This can be achieved using fault current limiter technology or oversized switchgear to break the arc.

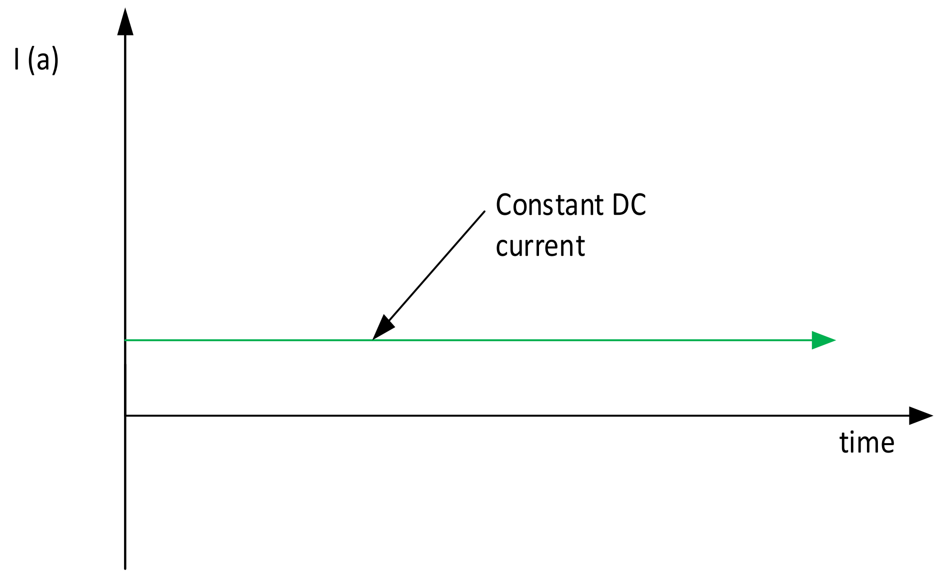

Figure 10: Constant DC Current

Reference [56] establishes the standard to understand the above concept. A simplified representation of an equivalent DC line circuit can be seen in Figure 11, which estimates an arc fault extinction.

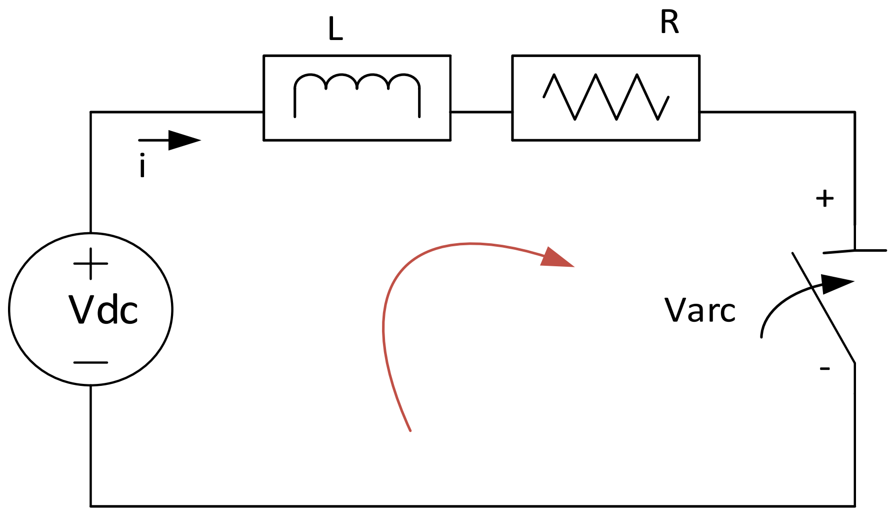

Figure 11: Equivalent DC Circuit

V_{dc} is the DC source voltage, L and R are the inductance and resistance, V_{arc} is the arc voltage. KVL of Figure 11 yield the following:

$$V_{dc} = L\frac{di}{dt} + Ri + V_{arc}, \tag{2.1}$$

Solving for $\frac{di}{dt}$ yield

$$L\frac{di}{dt} = V_{dc} - Ri - V_{arc}, \tag{2.2}$$

To guarantee arc extension according to [56], the following relationship should hold

$$\frac{di}{dt} < 0, \tag{2.3}$$

This relation should be checked when V_{arc} is high, because at this point, the inductance in Equation (2.2) will become negative. Taking the derivative of Equation (2.2) with respect to i and t, one can conclude that the arc extinction time of an MVDC system fault is proportional to the time constant of the circuit $T = \frac{L}{R}$ and to the difference between the circuit supply voltage and the arc voltage. Figure 12 below, displays an oscillogram relative to a short circuit test carried out by the ABB power testing lab

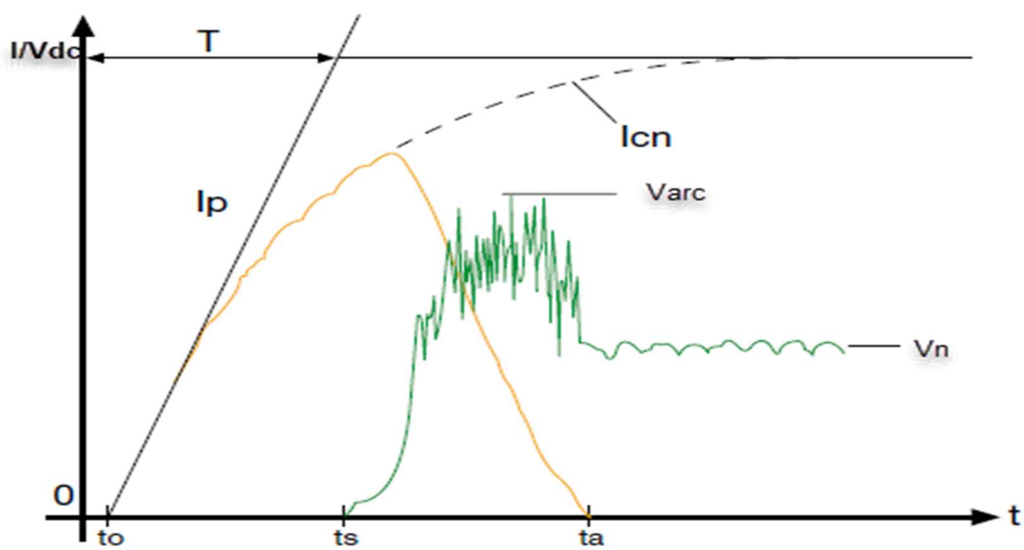

Figure 12: Short Circuit Oscillogram

where I_p is the short-circuit making current, I_{Cn} is the prospective short-circuit current, V_{arc} the maximum arc voltage, V_n is the network voltage, T is the time constant, t_0 short circuit starting time, t_s is the instant that separation begins of the circuit breaker contact, and t_a is the instant of quenching the fault current.

Upon occurrence of a short circuit at t_0 as shown in Figure 12 the current starts increasing according to the circuit time constant. To nullify the fault current, the circuit breaker contacts start separating from their contact point. This initiates an arc at t_s as shown in the Figure 12. It is worth mentioning that even though the circuit breaker contacts start opening, the current keeps increasing for a short period and then decreases. The decrease of the current is proportional to the amount of arc resistance introduced into the circuit from the opening of the contacts. To obtain a gradual extinction of the fault current, it is vital to cool and extend the arc, so that a gradual arc resistance is introduced in the circuit. The figure also highlights an important factor during the interruption, where the arc voltage remains higher than the supply voltage of the circuit. As shown in the same Figure 12, at t_a, the fault current is completely quenched. Furthermore, the fault current is extinguished without abrupt interruptions which is a result of an abrupt voltage peak. The lesson learned from Figure 12, is that in order to design a reliable fault protection system for a DC system, it is vital that the design meets the following conditions: 1) fast tripping response with adequate breaking capacity, 2) high fault current limiting capacity, 3) overvoltage reduction effect.

To further study grid DC fault signatures with a reliable protection system, in [57], an MVDC system with two 5 Megavolt Ampere (MVA), 60 Hz, 4160 V AC generators was designed to investigate the various fault dynamics. The study simulated the effects of line to ground, line to line and rectifier internal faults after steady state. It was discovered that the generator sub-transient and transient fault current are much different with the MVDC system when compared to the AC micro-grid. The paper suggested that when designing a reliable shipboard MVDC protection system, there are two important factors that should be considered: 1) a careful and precise consideration on DC bus faults and 2) always account for converter failures. Reference [58] conducted a DC arc flash risk assessment. The assessment was based on two techniques: 1) the maximum power method for computing the Incident Energy (IE) of an arc and 2) the arc resistance method. Both techniques aimed in computing the incident energy caused by the arc flash.

The Maximum Power Method (MPM) can be solved using the National Fire Protection Association 70E technique (NFPA 70E), which is a technique that uses a linear DC source as a voltage behind an impedance as shown in Figure 13. This technique stems from the application of maximum power transfer theorem in DC circuits. According to the theorem, the maximum power transfer occurs when the resistance of the system equals the resistance of the load. This technique considers the arc as a load that is applied to the DC power source and the system resistance as a combination of the internal resistance of the DC power source and the conductor resistance connecting to the load.

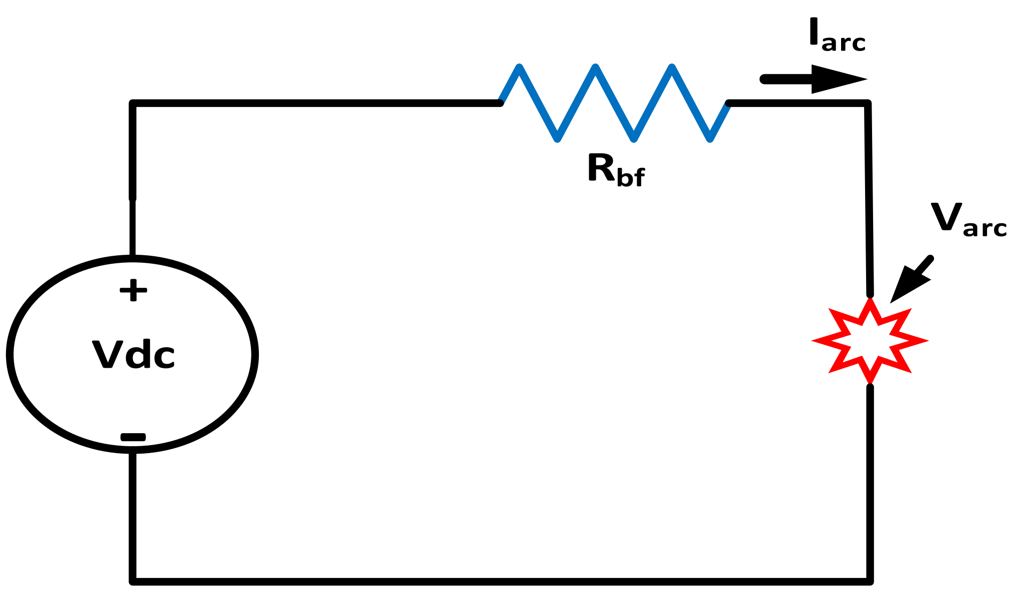

Figure 13: NFPA 70E Maximum Power Method DC Fault Circuit

In the circuit of Figure 13,

Vdc = the open circuit voltage source

R_{bf} = the bolted fault resistance

I_{arc} = the fault current through the arc fault contact points

V_{arc} = the voltage across the arc-fault contacts points

For [58] and [59], due to the non-linearity of the arc resistance, the adoption of 50% of the standard bolted current fault is a convenient approach rather than calculating the actual arc resistance. As a result, both papers concluded that 50% of the bolted current should reflect the maximum power transfer to the arc, thus:

$$V_{arc} = 0.5V_{dc}, \tag{2.4}$$

$$I_{arc} = 0.5I_{bf}, \tag{2.5}$$

where V_{sys} is the system voltage or open circuit voltage and I_{bf} is the bolted faulted current. Note that the bolted fault current is different from the short-circuit current. It is given by the maximum prospective short-circuit current in the faulted circuit and has zero impedance.

The incident energy within an enclosure using the MPM is given as follows:

$$IE = 3 * 0.02 * V_{arc} * I_{arc} * \frac{T_{arc}}{D^2}, \tag{2.6}$$

For open space the 3 is omitted.

T_{arc} is the time before the fault is cleared with an overcurrent protection system or a standard time of two seconds can be used instead, if no overcurrent is included in the design. D is the working distance or can be represented by the constant 18 inches.

The Arc Resistance Method (ARM), as stated in [60], is the most accurate and potentially less conservative technique for calculating arc flash incident energy. It is based on equations by A.D. Stokes and W.T. Oppenlander [61]. The equations were derived from an empirical study of free-burning horizontal and vertical arcs between series anodes and cathodes in open air. The equations are summarized as follow:

$$I_t = 10 + 0.2 * Z_g, \tag{2.7}$$

$$V_{arc} = \left(20 + 0.5348 * Z_g\right) * I_{arc}^{0.12}, \tag{2.8}$$

$$R_{arc} = \frac{\left(20 + 0.5348 * Z_g\right)}{I_{arc}^{0.88}}, \tag{2.9}$$

where: I_t is the transition current and Z_g is the gap between the conductors.

Figures 14 and 15 show that as the arc voltage V_{arc} decreases, the arc current I_{arc} increases for both the horizontal and vertical Open Air DC arc voltage.

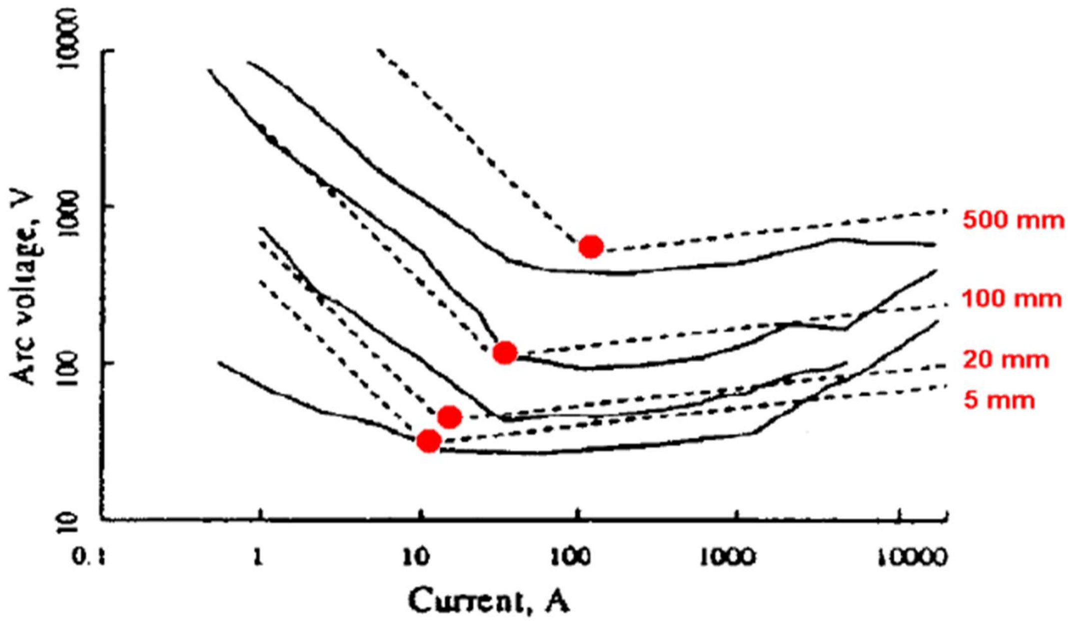

Figure 14: Horizontal Open-Air DC Arc Voltage V-I Curve [61]

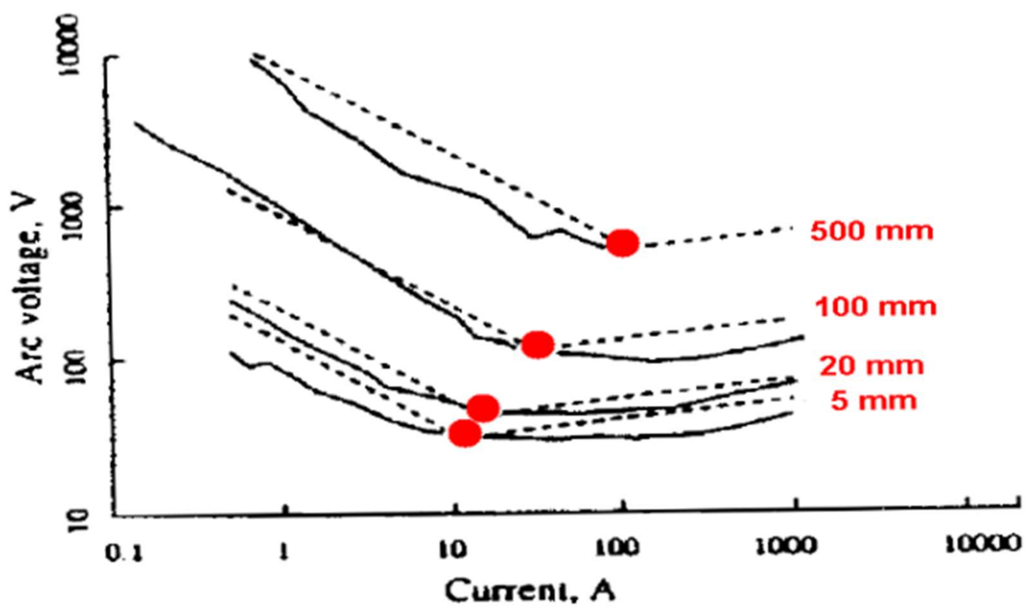

Figure 15: Vertical Open-Air DC Arc Voltage V-I Curve [61]

These two figures highlight another important issue regarding the use of DC breakers for fault isolation. For DC breakers to open, the nominal voltage of the system must be lower than the arc voltage between the breaker terminals.

Some other protection systems proposed installing a protection system on the AC side of the grid instead of the DC bus. The reason behind that, is that a fault on the DC bus is reflected on the AC sides, which has a well-established protection technique to clear the fault. However, this is not applicable for larger DC networks [62]. Furthermore, most digital AC protection relays will not accurately process the distorted waveform as they use only the filtered 60 Hz fundamental component. Some other published work proposed the introduction of an artificial zero crossing to force the fault current to zero and others proposed to induce an oscillating current to lead the current to zero [63], [64]. Reference [65] displays Table 1, which summarizes the current trend types of fault protection techniques.

	Differential protection	Directional protection	Impedance protection	Overcurrent protection	Current derivative protection
Procedure	KCL (Current summation equal to 0)	Current reverses direction during fault	Apparent impedance drops into the tripping interval during fault	Current goes over threshold during fault	I derivative goes over threshold during fault
Networking	Dependent	Dependent	Independent	Independent	Independent
Signal Control Area	Global	Global	Local	Local	Local
Transient Sensitivity	communication dependent	Sensitive to dynamic interactions at transients; communication dependent	Sensitive to fault impedance	Sensitive to distorted fault current waveforms	Sensitive to system noise

Table 1: Different Fault Localization Techniques

From Table 1, the MVDC fault protection techniques can be classified into two groups: communication-dependent and communication-independent protection system.

Communication-dependent protection techniques depend on an exchange of information at different zones of the system via wide area communication. In the literature, two methods of this technique have been proposed, which are differential based protection and directional protection. The first technique, a differential based protection system, uses Kirchoff's Current Law (or KCL), which considers that the summation of the current entering and leaving a node to be equal to zero. Once the error is compared to zero, if it is too high, a fault flag is raised to initiate the protection algorithm. The second technique, a directional protection system, states that upon occurrence of a fault the direction of the current entering a relay should reverse. The differential and the directional based protection systems are supplemented with an overcurrent protection system to provide a robust protection to the system.

Communication-independent techniques rely on the local information to protect the DC system against fault currents. Three types of communication-independent techniques are proposed in the literature as shown in Table 1. First, there is impedance protection, which protects the system from local switch voltage and current readings. The apparent resistance is computed based on the switch readings and then compared to a tripping threshold to determine the presence of a fault within the area. Secondly, there is overcurrent protection, which measures the current going through a switch and then compares it to a tripping threshold to define the existence of an overcurrent. Third, there is a current derivative protection, which compares the current derivative to a tripping threshold and sets a tripping flag if a fault is detected

Current trends on DC fault protection system also presented two tools used in the design of DC grid protection. Some of the proposed techniques make use of Voltage Source Converters (VSC) as a crowbar along with disconnect switches. During operation, once a fault is detected, the built-in current limitation device inside the VSC shorts out the VSC input to protect it and the source side of the grid is isolated from the fault by an AC circuit breaker or switch. Other techniques are taking advantage of the advancements in power electronics by using state of the art Solid State Circuit Breakers (SSCB) instead of AC or DC circuit breaker. One of the advantages that SSCBs offer, is that they have a faster fault interruption response. However, the SSCBs are more expensive. In the design, the SSCBs are generally placed at the DC terminal of the VSCs or downstream of the DC-DC converter [55], [63].

2.5.3 MVDC Fault Detection and Isolation Techniques

The notion of fault protection encompasses two parts. The first part is to detect in a timely manner that a fault exists within the system. The second part is to localize and isolate the fault to protect the overall grid stability. Various kinds of classical fault location techniques for AC distribution systems have been presented in the literature. For instance, some techniques are based on monitoring system reactance from one terminal of a line [64], [66], while other proposed solutions use fault traveling waves as index for fault localization [67], [68]. Furthermore, some proposed techniques use phasor measurement unit or phasor information [69], [70]. Even though some of the classical techniques are applicable to DC grids, they were designed for longer AC distribution systems, which means several miles of cables.

In [71], the Average-Value Modeling (AVM) technique is based on analytical time-domain modeling. This technique was developed to assess shipboard MVDC power system dynamic behaviors following bus disturbance. AVM is a technique used to reduce system numerical analysis complexities, while at the same time, increasing the overall system efficiency. The literature presents two types of AVM: analytical and parametric AVM modeling. The main idea behind AVM is to set a frequency range of interest. System(s) or sub-system(s) whose frequencies are within range are kept and the rest are neglected. Thus in [71], the prime mover and field exciter control loops are neglected. The developed AVM model was then tested on a single and double generator MVDC model. The system responses were then compared to a developed steady state model. The AVM response was deemed to have a better system behavior analysis according to the authors.

In [72], a centralized protection technique with two communication assisted fault detection methods were developed. During grid operation, the proposed technique by means of a set of differential relays, monitors the MVDC system current flow through junction points between the voltage source converter and the micro-grid. Each zonal differential relay will receive the DC current readings of its corresponding line. A fault is detected and localized if the difference of the measured current is not closed and greater to a set threshold to prevent maloperation of the relay. If a fault is detected, a trip signal is issued to the corresponding DC breaker to isolate the fault. The restoration of the network is followed by a self-healing technique to maintain overall system stability. A backup protection system was also designed in case a communicated protection system fails.

In [73], Tang and Ooi presented a Multi-Terminal DC power system (MTDC). The system consists of DC circuit breakers and switches for fault isolation, power electronics for power conversion and a hybrid power distribution system. The handshaking technique is used to define a DC current fault. During the handshaking process, it is assumed that a fault in a line has already been detected. The difference between the pre-fault line measurement and the post-fault line measurement defines the existence of a DC fault current. The direction of the DC fault is summarized as follows:

- During line-to-line DC faults, the grid side is characterized by low voltages and the presence of an overcurrent. The DC side is defined by a low DC voltage and a high DC current.
- During a line-to-ground DC fault, the grid side is also defined by a low voltage and a presence of an overcurrent, and the DC side is defined by an unbalanced DC voltage.

In either case, the direction of the fault is well defined and the terminal switches corresponding to the concerned VSCs are opened.

In [62], a communication based differential protection scheme with DC breakers has been proposed for a remote mine site based on a high-resistance fault in the MVDC system. Three protection systems were designed to maintain the reliability and security of the overall grid. 1) Based on the understanding of KCL, the synchronous current measurement technique was used to measure the current entering and leaving the line nodes. A fault is declared in the transmission line when the summation of the measured current is different than zero. A trip signal follows instantaneously to isolate the fault. A backup transmission line protection system (overcurrent) was also added to boost the robustness of the system. The backup overcurrent protection is trigged 0.5 s after if the primary protection system fails to respond to the fault. 2) A DC directional overcurrent protection system was used to provide protection to the voltage sources. This protection monitors the system for sag. Upon the detection of sag due to a fault, the protection system sends a trip signal to the breaker and notifies the source to stop feeding the fault. 3) The same DC directional protection system described in 2) was also used to provide protection to the loads. The only difference between the two protection systems is, in the case of a high-impedance fault, the fault is fed for a short period instead of tripping the breaker right away. If the system is designed to instantly trip the breaker, then an extra protection should be designed to protect the load according to the authors. In [49], a Local Information-based Fault Protection (LIFP) technique was proposed to detect, isolate, and then reconfigure a fault in an MVDC system. This technique is based on the apparent resistance technique which falls in the communication-independent group.

2.6 CONCLUSION

In this chapter, a comprehensive literature review on FESS and shipboard MVDC was presented. The review covers important aspects of future shipboard power systems including energy storage requirements, transitions from LVAC to MVDC distribution, system fault detection and fault protection.

FESS is the leading technology suitable for shipboard distribution systems to rapidly discharge energy as desired when ordinary generators cannot respond to fast dynamic loads. Their application extends to distribution systems where medium to high power (kW to MW) discharges within a short period are necessary. Well-designed FESS will not only guarantee shipboard power stability but will also ensure that the overall system is more reliable. The literature has presented tremendously well-designed systems techniques. However, their dependency on the smart grid automation makes them vulnerable to any unforeseen network or control system error or failure. On the other hand, medium voltage DC systems are the new emerging distribution systems being considered by many industries, especially the U.S. Navy. Literature has presented numerous advantages for implementing MVDC over AC grids, however, many challenges remain to be addressed. Despite the vast amount of published information, it is obvious that there is a significant knowledge gap in designing shipboard MVDC systems with effective fault protection, especially considering entanglements with system dynamics from pulsed power activity that may obscure the detection of genuine faults or cause maloperation of protective devices. Chapter 3, Section 1 will highlight the literature push of the proposed model and discuss its mathematical formulation. Section 2 will demonstrate arc fault detection techniques that are suitable for the shipboard MVDC systems as well as propose a short new circuit technique to the system.

CHAPTER 3

SHIPBOARD FLYWHEEL ENERGY STORAGE SYSTEM FORMULATION

3.1 FLYWHEEL ENERGY STORAGE FOR PULSED-POWER APPLICATIONS

FESS plays a key role in maintaining shipboard power system stability and reliability which result in a higher overall system efficiency. For conventional applications, power system stability is maintained through system voltage, frequency, and generator angle control. For MVDC, since the AC power distribution frequency is decoupled from the prime movers (generators) angles, therefore maintaining generators angle stability is not of concern. The integration of FESS into a power grid will prevent oversizing generators to serve momentary pulsed power loads.

Pulsed-power technology consists of electrical hardware relying on the storing and discharging of electrical energy in very short time periods (in the order of several minutes, seconds or less). During the process, energy storage devices such as batteries, capacitors or flywheels are charged over a long period and then rapidly discharged to supply an electrical system. PPT load demands typically exceed the total available generation capacity of a system and require ESDs to supplement their draw. The co-existence of PPTs and ESDs is a developing art form in modern power system design, especially in shipboard applications. In this section, one promising form of ESDs, the flywheel energy storage system (FESS), is studied and modeled for a shipboard power system.

3.2 CHALLENGES IN REPORTED RESEARCH

After a thorough literature review presented in Chapter 2, it was discovered that this (FESS) important energy storage system lacks an alternate or back up system. In a military application, FESS requires a backup mode of operation should the automatic control system fail. The challenge regarding the FESS is to enable this system with a local or alternate charge and discharge mechanism. Doing so will prevent shipboard power system disturbance from an automation network glitch, freeze, error or even failure. Furthermore, the integration of the developed FESS into the degraded shipboard power system caused by a pulsed power load should exhibit some transient stability improvement on the following:

- A very low stress or disturbance on the generator electrical and mechanical power because of their natural response to loading increase. Generators tend to slow down so that enough power can be generated to supply the over demand. Consequently, an improvement in the system efficiency should be noted because of decrease in fuel consumption and emission. For a larger grid, a reduction in unit commitment should also be noted.
- On the distribution side, the developed FESS should exhibit a smooth short-term power variation caused by the pulsed-power load.

3.2.1 FESS Problem Formulation

Consider the FESS shown in Figure 16

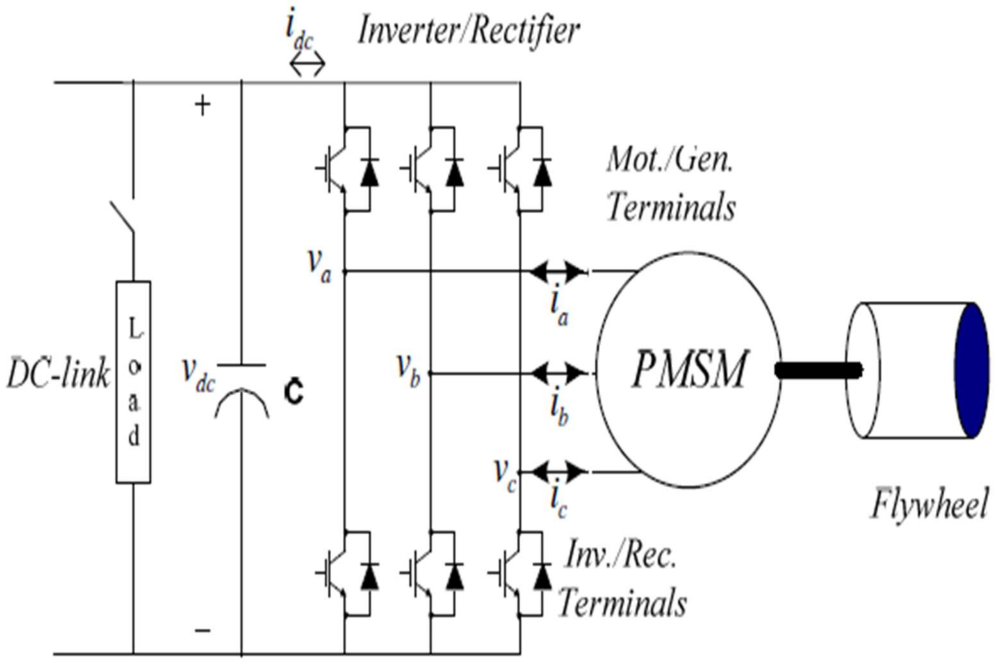

Figure 16: Flywheel Energy Storage System.

The above figure is comprised of a flywheel, a PMSM as a motor generator, a three-phase Pulsed Width Modulation (PWM) inverter/rectifier, a DC bus, and a load. To reduce the problem control complexity, the D-Q rotational reference frame called Park transformation was used to derive the system mathematical equations.

Consider a Permanent Magnet Synchronous Machine (PMSM) axes representation as shown in Figure 17 below,

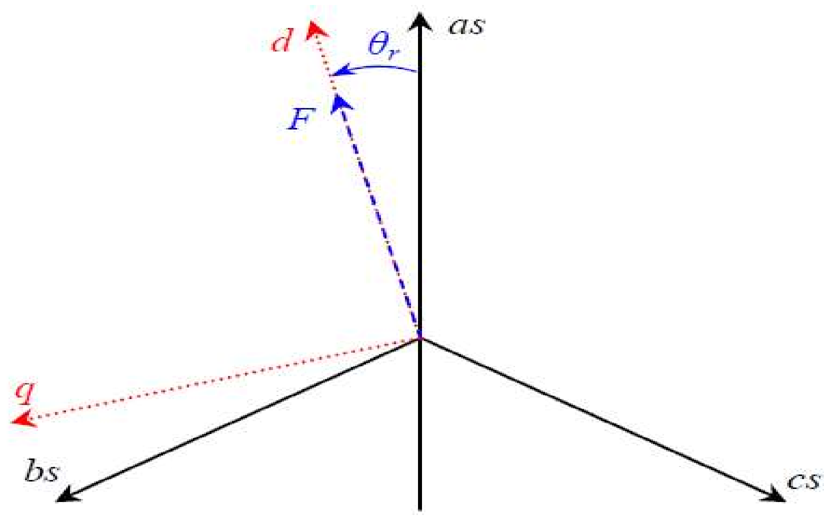

Figure 17: PMSM D-Q Frame Representation

where Θ_r is the rotor position which displays the angular speed w_r direction; as, bs, and cs are the stationary winding axis, and D-Q the Park transformation axis.

Let

$$f_{qdo} = P_s f_{abc}, \tag{3.1}$$

where P_s is the park transformation as shown in Equation (3.2)

$$P_s = \begin{bmatrix} \cos(\Theta) & \cos\left(\Theta - \frac{2\pi}{3}\right) & \cos\left(\Theta - \frac{4\pi}{3}\right) \\ -\sin(\Theta) & -\sin\left(\Theta - \frac{2\pi}{3}\right) & -\sin\left(\Theta - \frac{4\pi}{3}\right) \\ \frac{1}{\sqrt{2}} & \frac{1}{\sqrt{2}} & \frac{1}{\sqrt{2}} \end{bmatrix}, \tag{3.2}$$

where Θ is the angle between the D axis and the a_s for the stationary reference frame and a_r for the rotational reference frame.

The PMSM can be defined as:

$$V_{abcs} = R_s i_{abcs} + p\lambda_{abcs}, \tag{3.3}$$

where V_{abcs}, R_s, i_{abcs}, p, and λ are the voltage, stator resistance, current, number of poles, and the flux linkages respectively.

Let the flux linkages be defined as follow:

$$\lambda_{abcs} = L_{ss} i_{abcs} + \Lambda_m \ , \tag{3.4}$$

where

$$L_{ss} = \begin{bmatrix} L_{SL} + L_{sm} & -\frac{1}{2}L_{sm} & -\frac{1}{2}L_{sm} \\ -\frac{1}{2}L_{sm} & L_{SL} + L_{sm} & -\frac{1}{2}L_{sm} \\ -\frac{1}{2}L_{sm} & -\frac{1}{2}L_{sm} & L_{SL} + L_{sm} \end{bmatrix}, \qquad \Lambda_m = \sqrt{\frac{2}{3}}\lambda_m \begin{bmatrix} \sin(\theta) \\ \sin\left(\theta - \frac{2\pi}{3}\right) \\ \sin\left(\theta + \frac{2\pi}{3}\right) \end{bmatrix}, \tag{3.5}$$

L_{ss} is the stator self-inductance matrix, L_{SL} is the stator leakage inductance, L_{sm} is the stator magnetize inductance, Λ_m the PM flux linkage, and λ_m the mutual flux.

By applying the Park transformation Equation (3.2) to the PM Equation (3.3) yield Equation (3.6):

$$V_{qd0} = R_s i_{qd0} + p\lambda_{qd} - [pP_s]P_s^{-1}\,\lambda_{qd} \ , \tag{3.6}$$

where

$$[pP_s]P_s^{-1} = \begin{bmatrix} 0 & -w_r & 0 \\ w_r & 0 & 0 \\ 0 & 0 & 0 \end{bmatrix} = -w_r\, X, with\, X = \begin{bmatrix} 0 & 1 & 0 \\ -1 & 0 & 0 \\ 0 & 0 & 0 \end{bmatrix}, \tag{3.7}$$

Applying Equation (3.6) to Equation (3.5) yield

$$V_{qd0} = R_s i_{qd0} + p\lambda_{qd0} + w_r X \lambda_{qd0}, \tag{3.8}$$

Applying Park transformation Equation (3.2) to Equation (3.4) yield in:

$$\lambda_{abcs} = P_s L_{ss} P_s^{-1} i_{qd} + P_s \Lambda_m = L_{qd0} i_{qd0} + \Lambda_{qd0}, \tag{3.9}$$

where

$$L_{qd0} = \begin{bmatrix} L_{SL} + \frac{3}{2}L_{sm} & 0 & 0 \\ 0 & L_{SL} + \frac{3}{2}L_{sm} & 0 \\ 0 & 0 & L_{SL} \end{bmatrix}, \Lambda_{qd0} = \lambda_m \begin{bmatrix} -\sin(\theta) \\ \cos(\theta) \\ 0 \end{bmatrix}, \tag{3.10}$$

with the D-Q magnetizing inductance defined as

$$L_{md} = L_{mq} = \frac{3}{2} L_{sm}, \tag{3.11}$$

Such that $L_{qs} = L_{mq} + L_{SL}$ and $L_{ds} = L_{md} + L_{SL}$. By assuming that the PM is surface mounted, the D-Q inductances will be equal to L, L_{qd0} then become:

$$L_{qd} = \begin{bmatrix} L & 0 & 0 \\ 0 & L & 0 \\ 0 & 0 & L_{SL} \end{bmatrix}, \tag{3.12}$$

Substituting Equation (3.9) and Equation (3.10) into Equation (3.8) yield the following:

$$V_{qd} = R_s i_{qd0} + L_{qd0} p\left(i_{qd0}\right) + w_r X L_{qd0} i_{qd} + w_r X \Lambda_{qd0}, \tag{3.13}$$

since

$$i_a + i_b + i_c = 0 => i_0 = v_0 = 0 \text{ Thus}$$

$$\begin{cases} v_{ds} = r_s i_{ds} + Lpi_{ds} - \omega_r L i_{qs} + e_{ds} \\ v_{qs} = r_s i_{qs} + Lpi_{qs} + \omega_r L i_{ds} + e_{qs} \ , \\ v_0 = 0 \end{cases} \tag{3.14}$$

where $e_{ds} = \omega_r \lambda_m sin\,(\theta)$ and $e_{qs} = \omega_r \lambda_m cos\,(\theta)$ are the PM D-Q back EMF voltages.

Using Equation (3.14), and by applying the Gyrator model, the generating mode equivalent circuit can be derived for the PMSM in the rotor reference as shown in Figure 18.

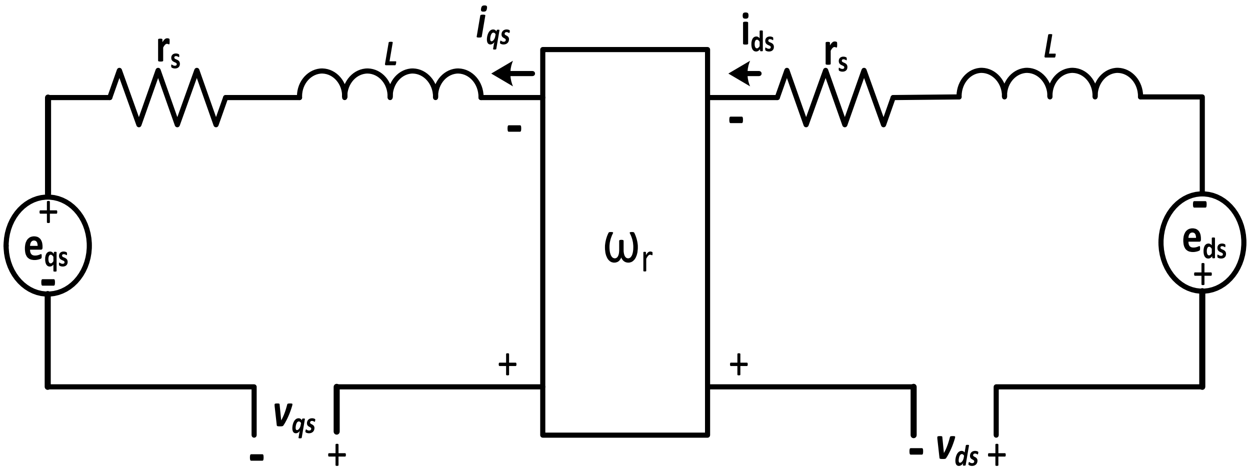

Figure 18: PMSM Equivalent Circuit in the Rotor Reference Frame

By using the mechanical differential Equation (3.15) of a flywheel, an equivalent circuit can be derived for the flywheel as shown below in Figure 19.

$$T_e = Jp\omega_m + f_m\omega_m, \tag{3.15}$$

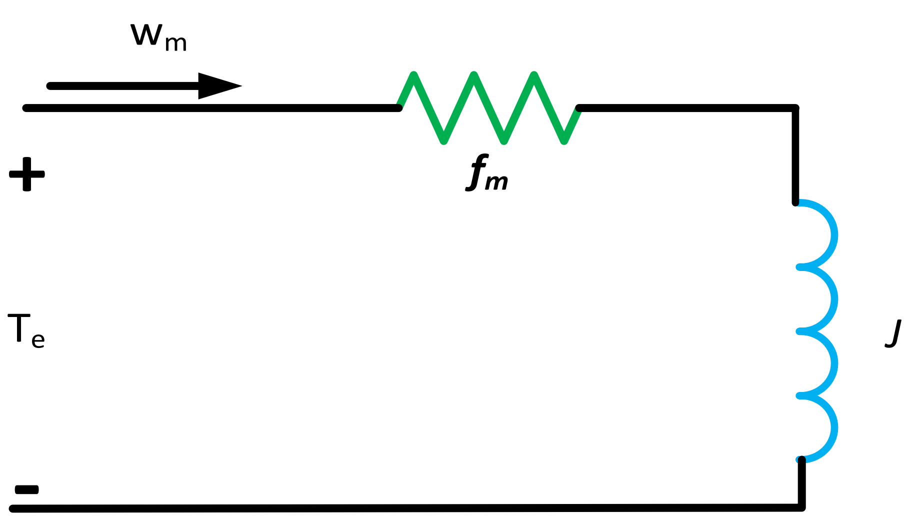

Figure 19: Flywheel Equivalent Circuit

The integration of the flywheel and the PMSM yield Figure 20 as shown below.

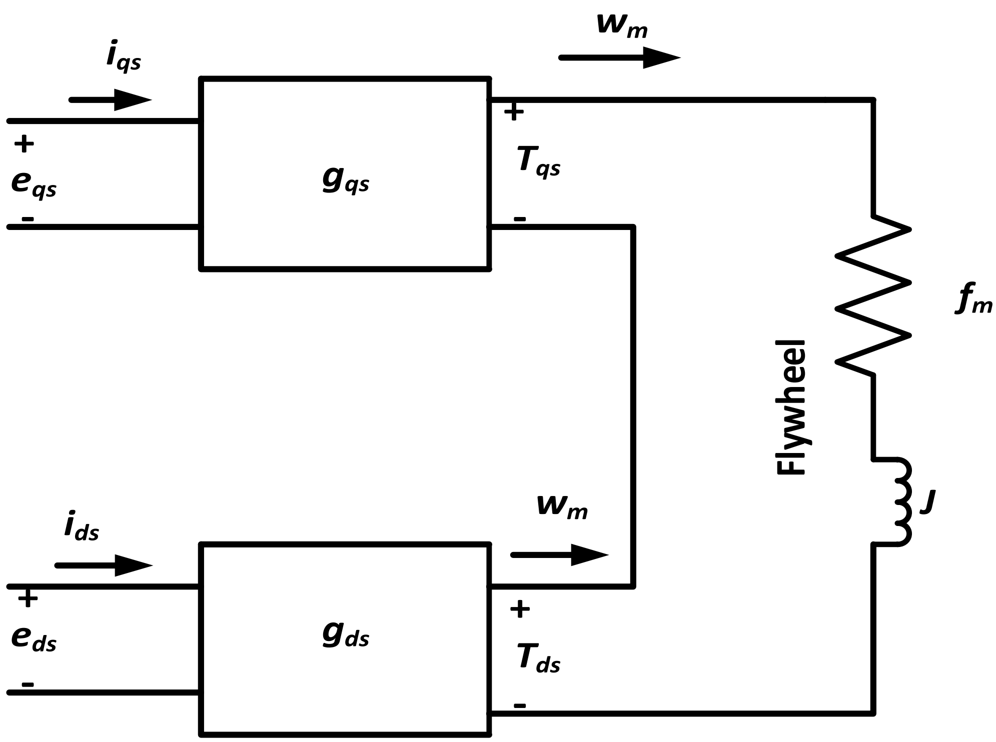

Figure 20: Flywheel Based on a PMSM

As stated earlier, during the charging mode the input power to the FESS comes from either a grid or other power source. During this mode, the DC bus can be modeled as a DC power source in parallel with a capacitor as shown in Figure 21 (a). Once the flywheel reached rated speed or is charged, the required "housekeeping" power is very small to keep it rotating due to near frictionless bearings. On the other hand, during the generating mode, the kinetic energy is extracted and then feeds into the rectifier and then to the DC link. During this mode, the DC bus is a combination of a load in parallel with a capacitor as shown in Figure 21 (b).

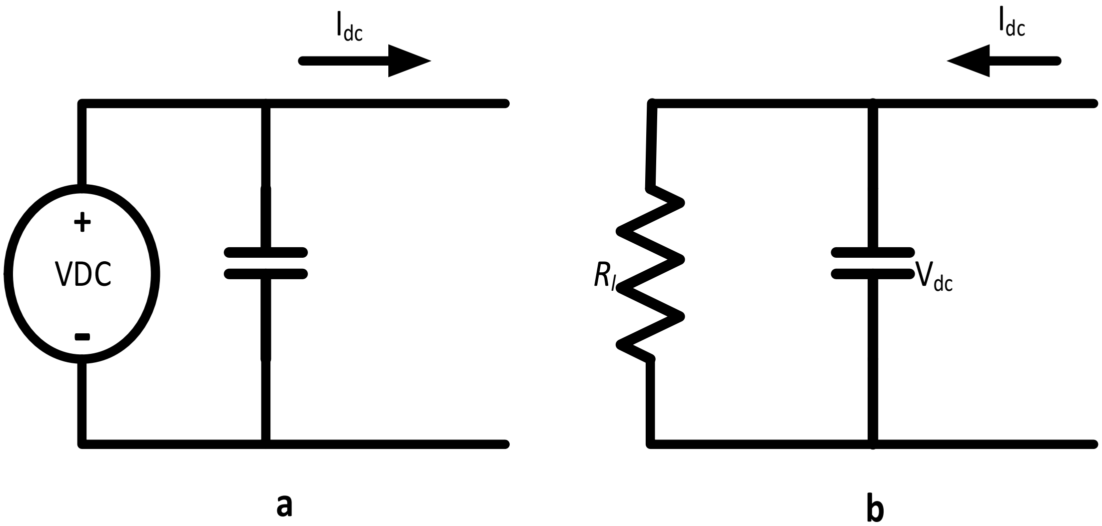

Figure 21: FESS DC Bus Model (a) Motoring Mode, (b) Generating Mode

In addition, whenever the DC bus is connected to the DC source this mode can also be called the inverting or charging mode. In this mode, the DC bus voltage remains constant. In the rectifying (generating) mode, the DC bus voltage can fluctuate, therefore it needs to be controlled. As a result of that, the switching set of the controller is transformed from stationary reference frame to D-Q synchronous reference frame Equation (3.16).

$$V_{abcs} = Sv_{dc}$$

$$V_{qd0} = P_s V_{abcs} = P_s S v_{dc} = m v_{dc}[-sin\,(\theta)\;\; cos\,(\theta)\;\; 0\,], \qquad (3.16)$$

where S is the switching function, and m the modulation index with,

$$S = \sqrt{\frac{2}{3}} m \begin{bmatrix} \sin(\theta) \\ \sin\left(\theta - \frac{2\pi}{3}\right) \\ \sin\left(\theta + \frac{2\pi}{3}\right) \end{bmatrix}, \theta = \theta_r + \varphi_2, \tag{3.17}$$

The PWM is used to control the power electronics as shown in Figure 22.

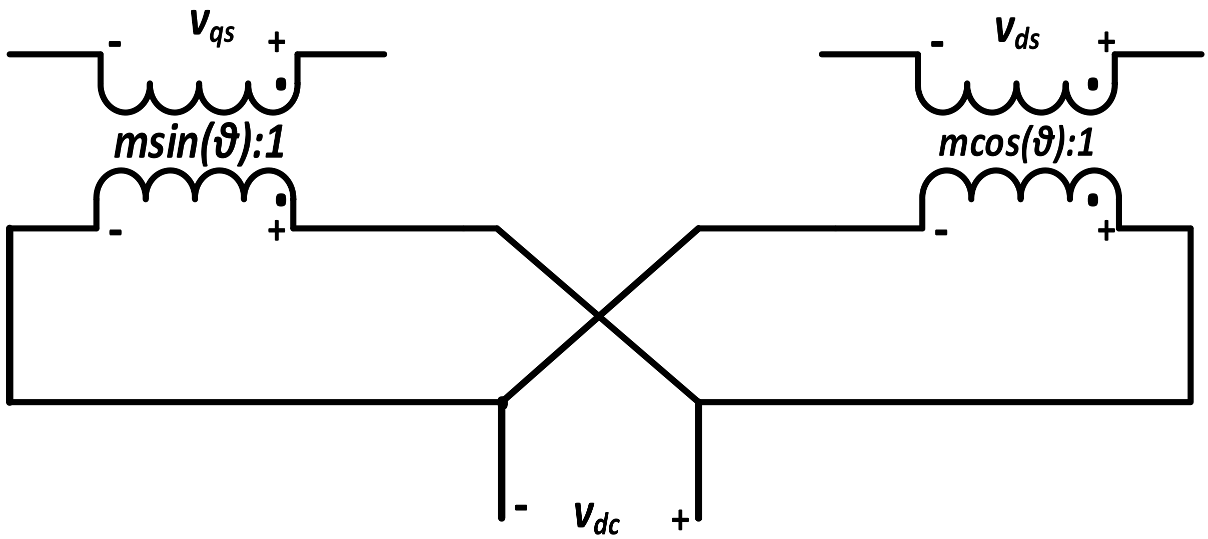

Figure 22: D-Q Representation of the PWM

3.2.2 FESS Control Strategy

Vector control is one of the control techniques used in FESS. The aim is to control the instantaneous grid's active and reactive currents independently. As discussed above, the independent control is given through the D-Q transformation. During the charging and discharging modes, the following control loops are carried out. An inner or faster stator current control loop, and a slower or outer control (speed and voltage) loops. These controls loops are displayed in Figure 23.

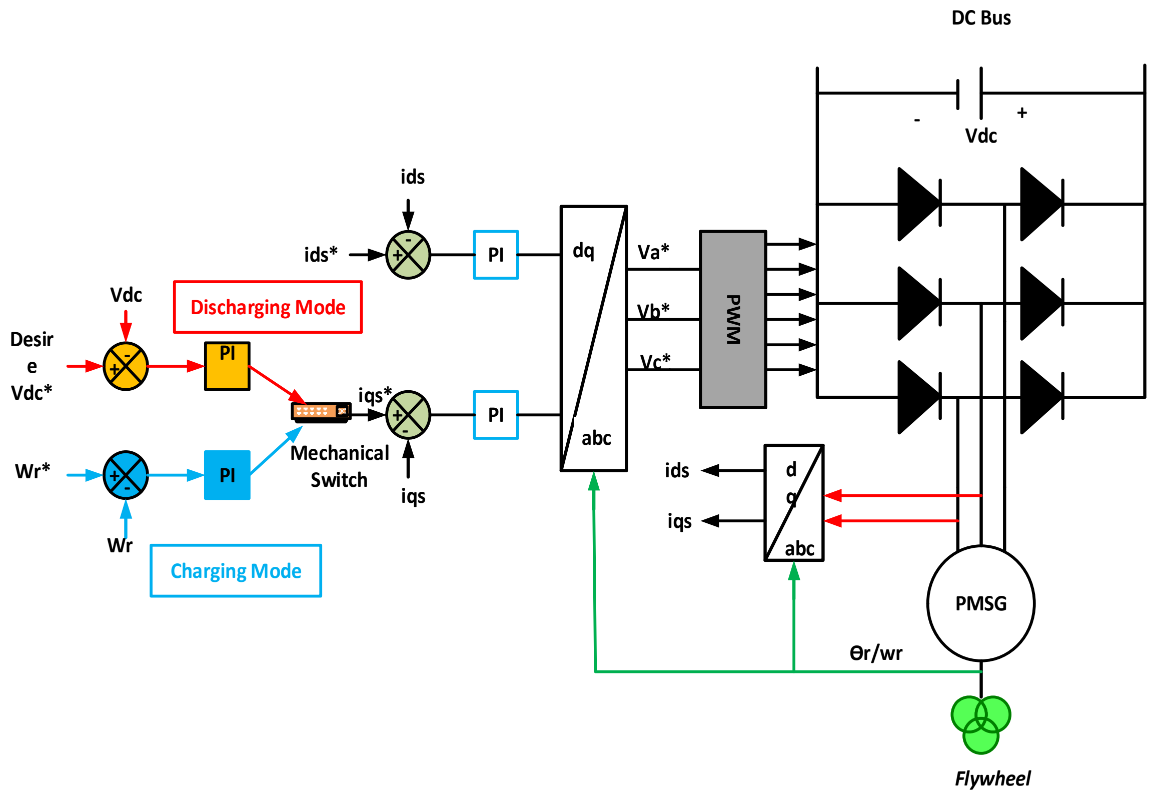

Figure 23: Overall FESS Control System

The inner control loop as shown in Figure 23, takes as input the error between the reference current and the measured stator current. The error is then fed into a Proportional Integral (PI) controller. The output signals from the PI controllers are compensated by a Feed-Forward Loop (FFL) to achieve the desire converter D-Q output voltage. The feed-forward minimizes the system's slow dynamic response thus making the inner control loop the fastest control loop. Note that the slow response is mainly caused by the PI controller. The PI controller must wait for a signal error before a signal correction can be made. To override the PI controller's slow response, FFL is used. This FFL is achieved by setting the stator active current i_{ds} in Equation (3.14) to zero. The structure of the feed-forward and the inner current loop are displayed in Figure 24.

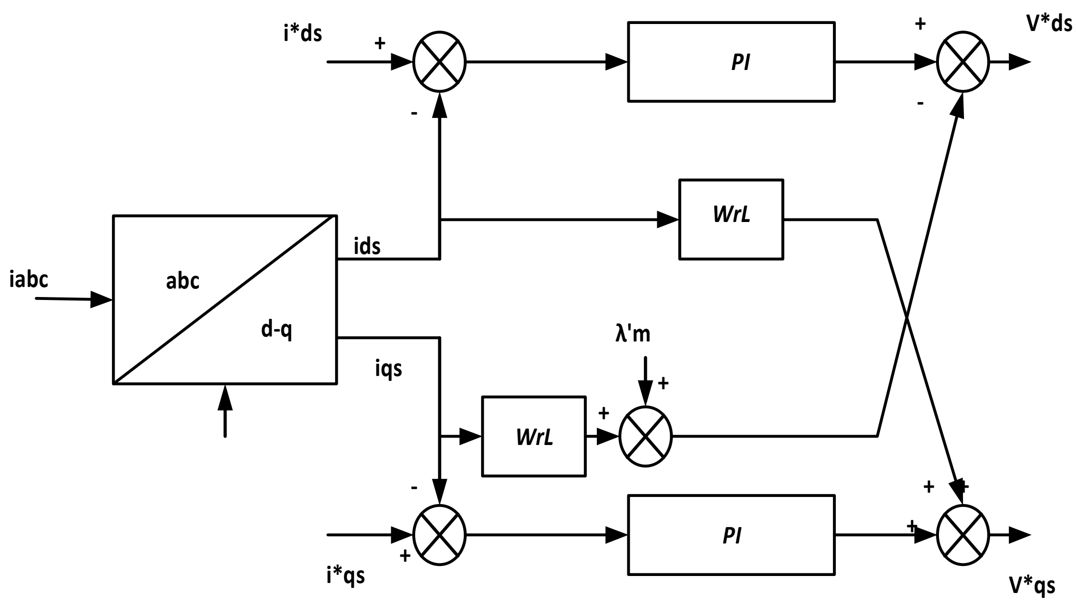

Figure 24: Inner Control Loops Feed-Forward

The outer speed controller shown in Figure 23 above, takes as input the error between the reference speed and the measured speed. The resultant signal is fed into a PI regulator to generate the desired reactive current used during the charging mode. It is worth mentioning that this controller only operates during the motoring mode.

The outer voltage controller shown in Figure 23 above, takes as input the error between the reference DC voltage and the measure DC voltage. The resultant signal is then fed into a PI regulator to generate the desired reactive current used during the generating mode. From Equation (3.14), the generating mode equations will be derived.

3.2.2.1 Charging Mode Control Formulation

The D-Q vector presentation of the PMSM during the motoring mode is shown in Figure 25.

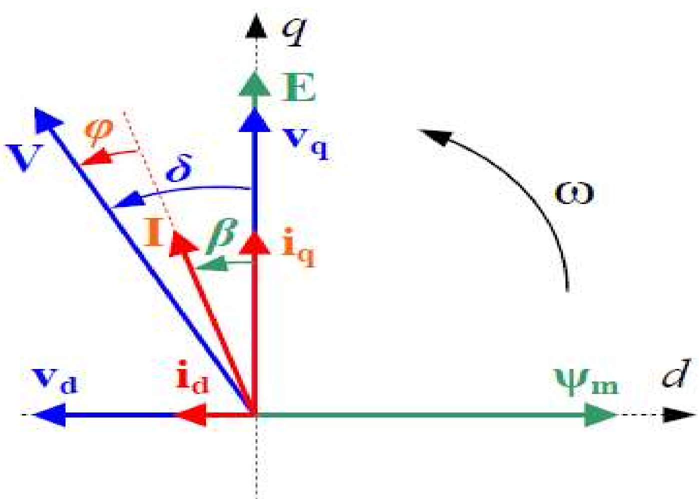

Figure 25: D-Q Motoring Vector Representation of the PMSM

where *V* and *I* are the stator voltage and current, *E* is the induce voltage, φ is the phase shift between the *V* and *I*. Assuming the q axis as the reference axis, β is the phase shift between i_{qs} and the *I*, and δ the phase between the induce voltage and *V*.

From Figure 25, the D-Q stator currents Equations (3.18) can be obtained such that:

$$i_{ds} = -Isin\,(\beta) \;\; and \; i_{qs} = Icos(\beta), \tag{3.18}$$

where $I = \sqrt{{i_{ds}}^2 + {i_{qs}}^2}$

During the motoring mode *cos* (φ) = 1, as a result of that $\beta = \delta$. Once the value of β is known, the reference D-Q stator currents can be obtained for unity power factor. According to the D-Q transformation derived above in Equation (3.14), substituting the back EMF equation and solving for the motoring mode equations result in Equation (3.19):

$\begin{vmatrix} v_{ds} \\ v_{qs} \end{vmatrix} = \begin{vmatrix} r_s + Lp - \omega_r L \\ r_s + Lp + \omega_r L \end{vmatrix} \begin{vmatrix} i_{ds} \\ i_{qs} \end{vmatrix} + \begin{vmatrix} 0 \\ \omega_r \lambda_m \end{vmatrix}$ Substituting (3.18) yield

$$\begin{vmatrix} v_{ds} \\ v_{qs} \end{vmatrix} = \begin{vmatrix} r_s + Lp - \omega_r L \\ r_s + Lp + \omega_r L \end{vmatrix} \begin{vmatrix} -I\sin(\beta) \\ Icos(\beta) \end{vmatrix} + \begin{vmatrix} 0 \\ \omega_r \lambda_m \end{vmatrix}, \tag{3.19}$$

δ can now be calculated as follow: $tan\ (\delta) = \frac{v_{ds}}{v_{qs}}$

$$\tan(\delta) = \frac{Isin(\beta)r_s + Icos(\beta)\omega_r L}{Icos(\beta)r_s - \omega_r LIsin(\beta) + \omega_r \lambda_m}, \tag{3.20}$$

Neglecting the stator current yield:

$$\tan(\delta) = \frac{Icos(\beta)\omega_r L}{-\omega_r LIsin\,(\beta)\ +\ \omega_r \lambda_m}, \tag{3.21}$$

Since $\beta = \delta$ during the motoring mode we get:

$$\frac{\sin(\beta)}{\cos(\beta)} = \frac{Icos(\beta)\omega_r L}{-\omega_r LIsin\,(\beta)\; + \;\omega_r \lambda_m}, \tag{3.22}$$

Assuming

$$i = \frac{IL_d}{\lambda_m} \; and \; \rho = \frac{L_q}{L_d}, \tag{3.23}$$

where $L_q = L_{qs}$ & $L_{d=} L_{ds}$, the stator inductances.

$$\frac{\sin(\beta)}{\cos(\beta)} = \frac{\rho icos(\beta)}{1 - isin\,(\beta)}, \tag{3.24}$$

For simplicity assume $(\beta) = x \; such \; that$

$$-i(1 - \rho\lambda_m)x^2 + x - i\rho\lambda_m = 0, \tag{3.25}$$

The solution to Equation (3.24) are:

$$x_{1,2} = \frac{1 \pm \sqrt{1 - 4\rho i^2\,(1 - \rho)}}{-2i(1 - \rho)} = \beta_{1,2}, \tag{3.26}$$

$$\sin(\beta) = \frac{1 - \sqrt{1 - 4\frac{L_d L_q I^2}{{\lambda_m}^2}\left(1 - \frac{L_q}{L_d}\right)}}{2\left(1 - \frac{L_q}{L_d}\right)\frac{IL_d}{\lambda_m}}, \tag{3.27}$$

From Equations (3.18) and (3.27), the charging mode can now be derived as follows:

$$\begin{cases} v_{ds} = r_s i_{ds} + Lpi_{ds} - \omega_r L i_{qs} \\ v_{qs} = r_s i_{qs} + Lpi_{qs} + \omega_r L i_{ds} + \omega_r \lambda_m \end{cases}, \tag{3.28}$$

with an electric torque

$$T_e = \pm \frac{P}{2}\lambda_m i_{qs} = J\frac{d}{dt}\omega_r + f_m \omega_r, \tag{3.29}$$

where f_m, and w_m are mechanical friction and speed, and P is the electric power.

The control diagram is given in Figure 26.

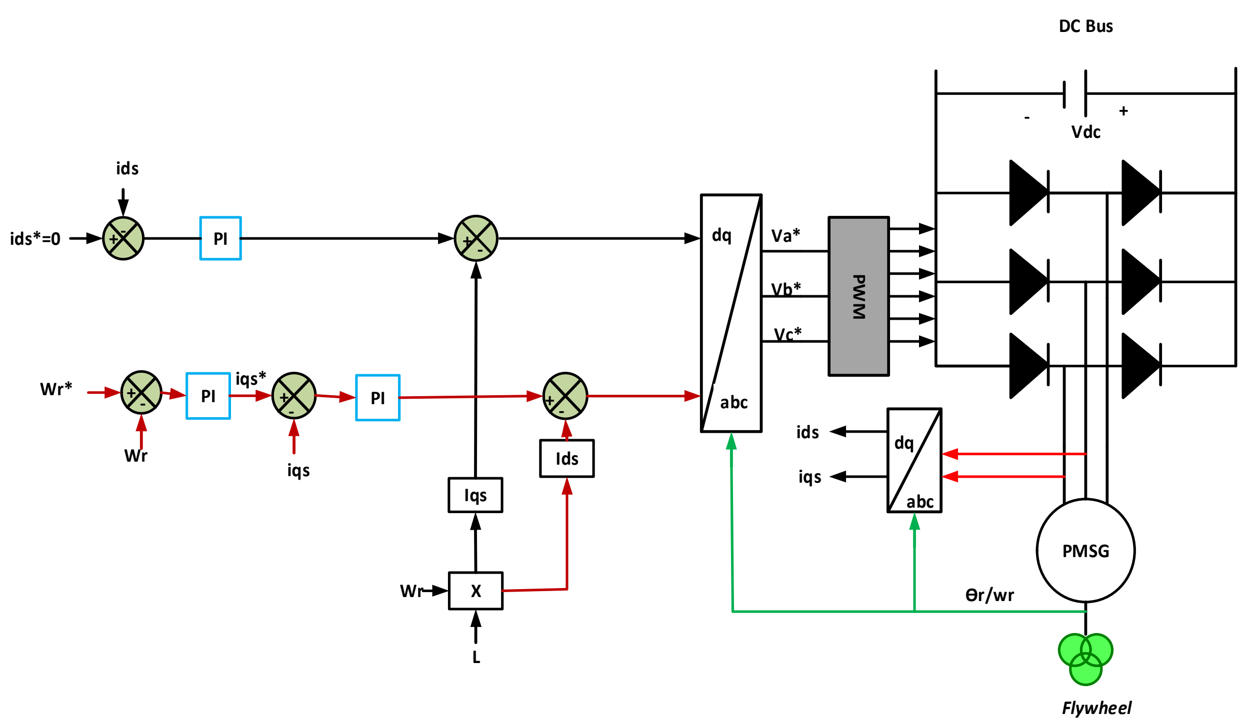

Figure 26: FESS Motoring Mode with Feed-Forward Loops

where $\lambda'_m = \sqrt{2/3}\lambda_m$ is the amplitude of the flux linkage established by the PMSM.

3.2.2.2 Discharging Mode Control Formulation

The D-Q vector presentation of the PMSM during the generating mode is shown in Figure 27.

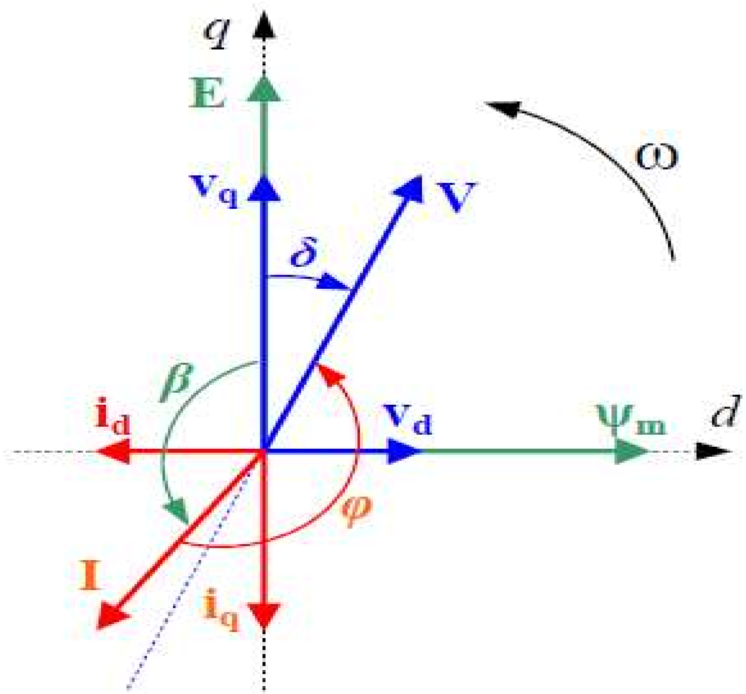

Figure 27: D-Q Generating Vector Representation of the PMSM

During the generating mode *cos (φ)* = -1, because of that $\beta = \pi + \delta$. The same process of the motoring section is repeated below:

$\begin{vmatrix} -v_{ds} \\ -v_{qs} \end{vmatrix} = \begin{vmatrix} r_s + Lp - \omega_r L \\ r_s + Lp + \omega_r L \end{vmatrix} \begin{vmatrix} i_{ds} \\ i_{qs} \end{vmatrix} + \begin{vmatrix} 0 \\ \omega_r \lambda_m \end{vmatrix}$, substituting Equation (3.18) yield

$$\begin{vmatrix} -v_{ds} \\ -v_{qs} \end{vmatrix} = \begin{vmatrix} r_s + Lp - \omega_r L \\ r_s + Lp + \omega_r L \end{vmatrix} \begin{vmatrix} -I\sin(\beta) \\ Icos(\beta) \end{vmatrix} + \begin{vmatrix} 0 \\ \omega_r \lambda_m \end{vmatrix}, \tag{3.30}$$

δ can now be calculated as follow:

$$\tan(\delta) = \frac{-Isin(\beta)r_s - Icos(\beta)\omega_r L}{Icos(\beta)r_s - \omega_r LIsin(\beta) + \omega_r \lambda_m}, \tag{3.31}$$

Neglecting the stator current yield:

$$\tan(\delta) = \frac{-\,Icos(\beta)\omega_r L}{-\omega_r LIsin\,(\beta)\ +\ \omega_r \lambda_m}, \tag{3.32}$$

Since $\beta = \delta$ during the motoring mode we get:

$$\frac{\sin(\beta - \pi)}{\cos(\beta - \pi)} = \frac{-Icos(\beta)\omega_r L}{-\omega_r LIsin\,(\beta)\ +\ \omega_r \lambda_m}, \tag{3.33}$$

Assuming

$$i = \frac{IL_d}{\lambda_m}\ and\ \rho = \frac{L_q}{L_d}\,, \tag{3.34}$$

$$\frac{\sin(\beta - \pi)}{\cos(\beta - \pi)} = \frac{\rho icos(\beta)}{1 - isin\,(\beta)}, \tag{3.35}$$

For simplicity assume $(\beta)\ = x\ such\ that$

$$-i(1-\rho\lambda_m)x^2 + x - i\rho\lambda_m = 0, \tag{3.36}$$

The solution to Equation (33) are:

$$x_{1,2} = \frac{1 \pm \sqrt{1-4\rho i^2\,(1-\rho)}}{-2i(1-\rho)} = \beta_{1,2}, \tag{3.37}$$

$$in\,(\beta-\pi) = \frac{1-\sqrt{1-4\frac{L_d L_q I^2}{{\lambda_m}^2}\left(1-\frac{L_q}{L_d}\right)}}{-2\left(1-\frac{L_q}{L_d}\right)\frac{IL_d}{\lambda_m}}, \tag{3.38}$$

From Equations (3.18) and Equation (3.38) i_{ds} and i_{qs} thus the charging mode can now be as follows:

$$\begin{cases} 0 = r_s i_{ds} + Lpi_{ds} - \omega_r L i_{qs} + v_{ds} \\ \omega_r\lambda_m = r_s i_{qs} + Lpi_{qs} + \omega_r L i_{ds} + v_{qs} \end{cases}' \tag{3.39}$$

With an electric torque

$$T_e = \pm \frac{P}{2}\lambda_m i_{qs} = J\frac{d}{dt}\omega_r + f_m\omega_r, \tag{3.40}$$

where f_m, and w_m are mechanical friction and speed, and *P* is the electric power.

The control diagram is given in Figure 28.

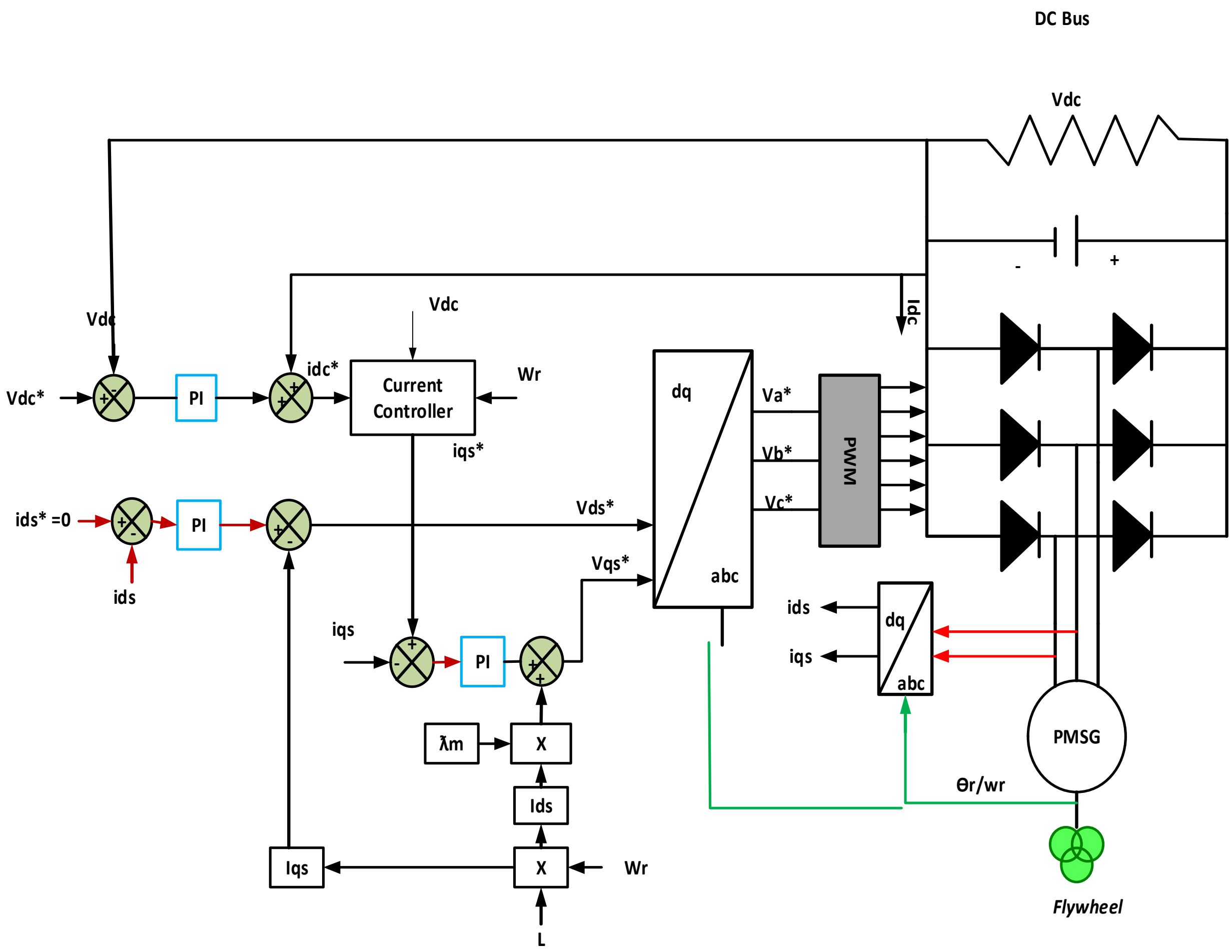

Figure 28: FESS Generating Mode with Feed-Forward Loops

3.3 DEVELOPED FESS PERFORMANCE AND VALIDATION

In this section, the developed FESS model is demonstrated in a MATLAB time-domain simulation of a shipboard power system. For studying the dynamics and disturbances, it is vital to include this crucial element into the simulation. A 2 MVA, three-phase, 400 V AC, 50 Hz, 1500 rpm synchronous generator coupled to a diesel engine is used to charge the FESS through a DC link via bidirectional back-to-back voltage source converters. This system is used because it represents a common naval ship distribution system. The simulation set points of the grid side are tabulated in Table 2.

Number of Phases	3
Number of Poles	2
Operating Speed Range	0 to 10000 RPM
Bus Nominal No Load Voltage	900 V DC at 10,000 RPM
Winding Resistance	2.875 Ω
Winding Inductance	0.00085151 H
Moment of Inertia	0.0063

Table 2: FESS PMSG Set Points

The grid side converter (rectifier) regulates the DC link voltage to a 900 V DC bus voltage. During operation, the DC link voltage is controlled to regulate the main AC voltage level during the charging and discharging of the FESS. On the flywheel side, another voltage source converter is used to make the PMSM behave as a motor during the charging mode or as a generator during the discharging mode. The system schematic in Simulink is shown in Figure 29.

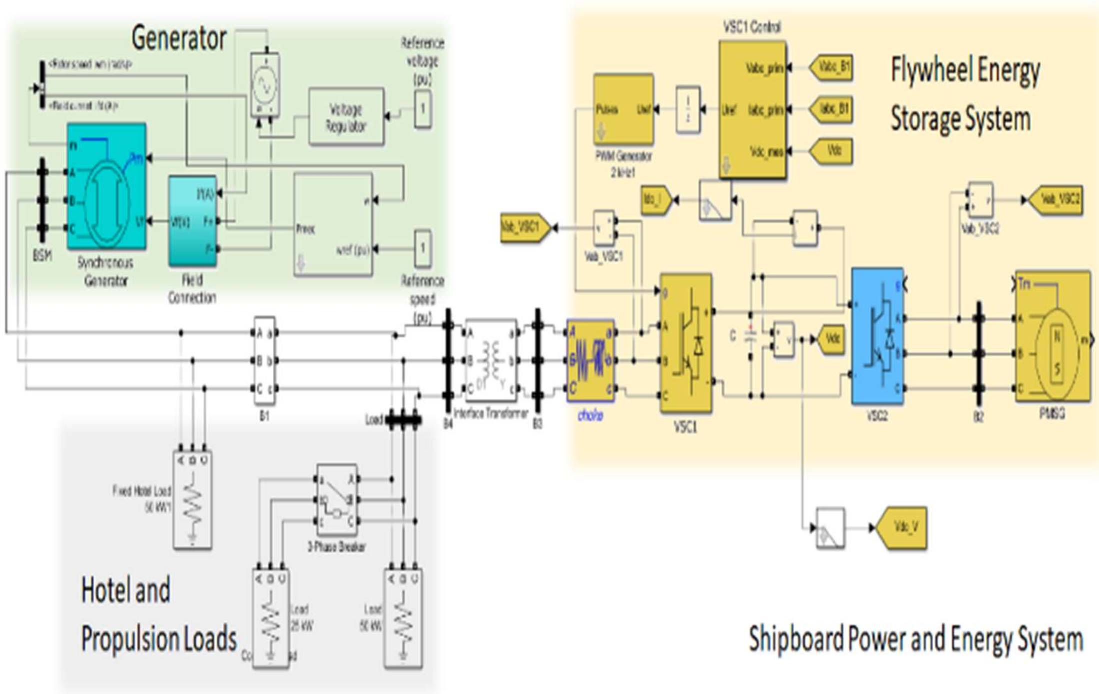

Figure 29: MATLAB-Simulink Model of a FESS

The control of both bidirectional converters is done through Clark and Park synchronous frame transformation called D-Q axis control. Using this transformation, grid side current vectors (active and reactive current) are decoupled and controlled independently using vector control. Here, the D-Q transform is explored further with the addition of a charge/discharge mechanical switch to the FESS. This switch enables the operator at any time to discharge energy back to the grid. This is achieved by the mechanical switch as shown in Figure 30 effecting a step change in the commanded torque signal inside the control loop to transition between modes.

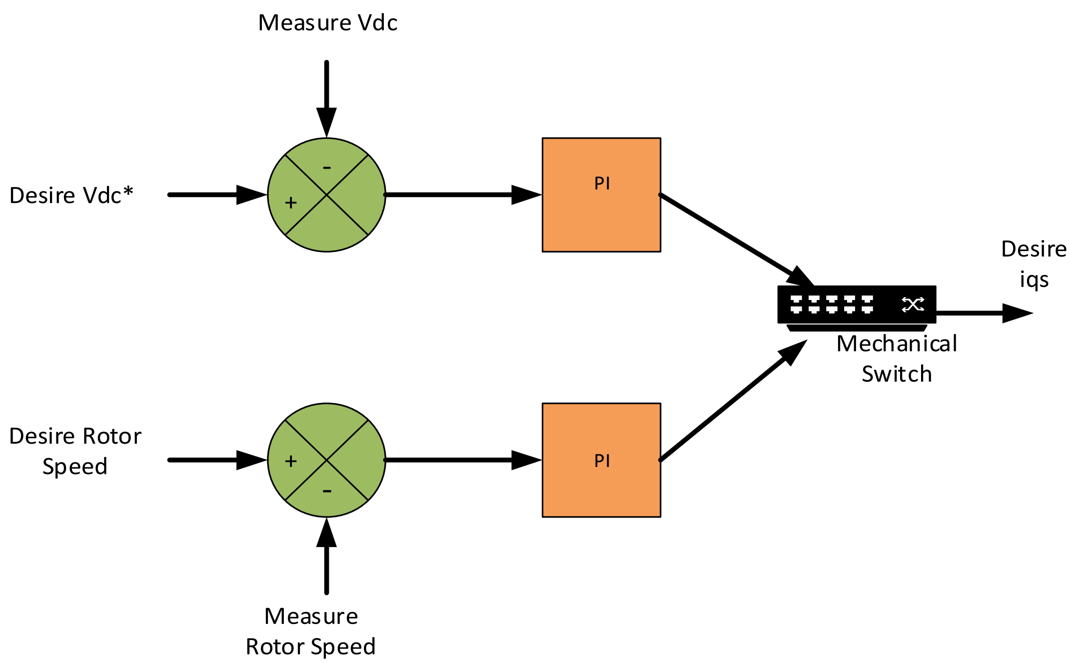

Figure 30: FESS Mechanical Charge/Discharge Switch

3.3.1 FESS Test Performance and Validation

To validate the performance of the developed FESS, three different case scenario tests were carried out. The tests are as follow:

1. Performance of the developed FESS on a shipboard power system under normal condition.
2. Performance of the shipboard power distribution system without FESS under pulsed-power load disturbance.
3. Performance of the shipboard distribution system with the developed FESS under pulsed-power load disturbance.

Case 1: FESS Normal Operation Run Performance

In the first case, the simulation was run for 10 seconds without switching the charge/discharge mechanical switch and leaving it in the charge position. Figure 31 shows the grid side synchronous machine voltage, and current, the grid side rectifier voltage, the DC-link voltage and the modulation index schematic during the charging mode.

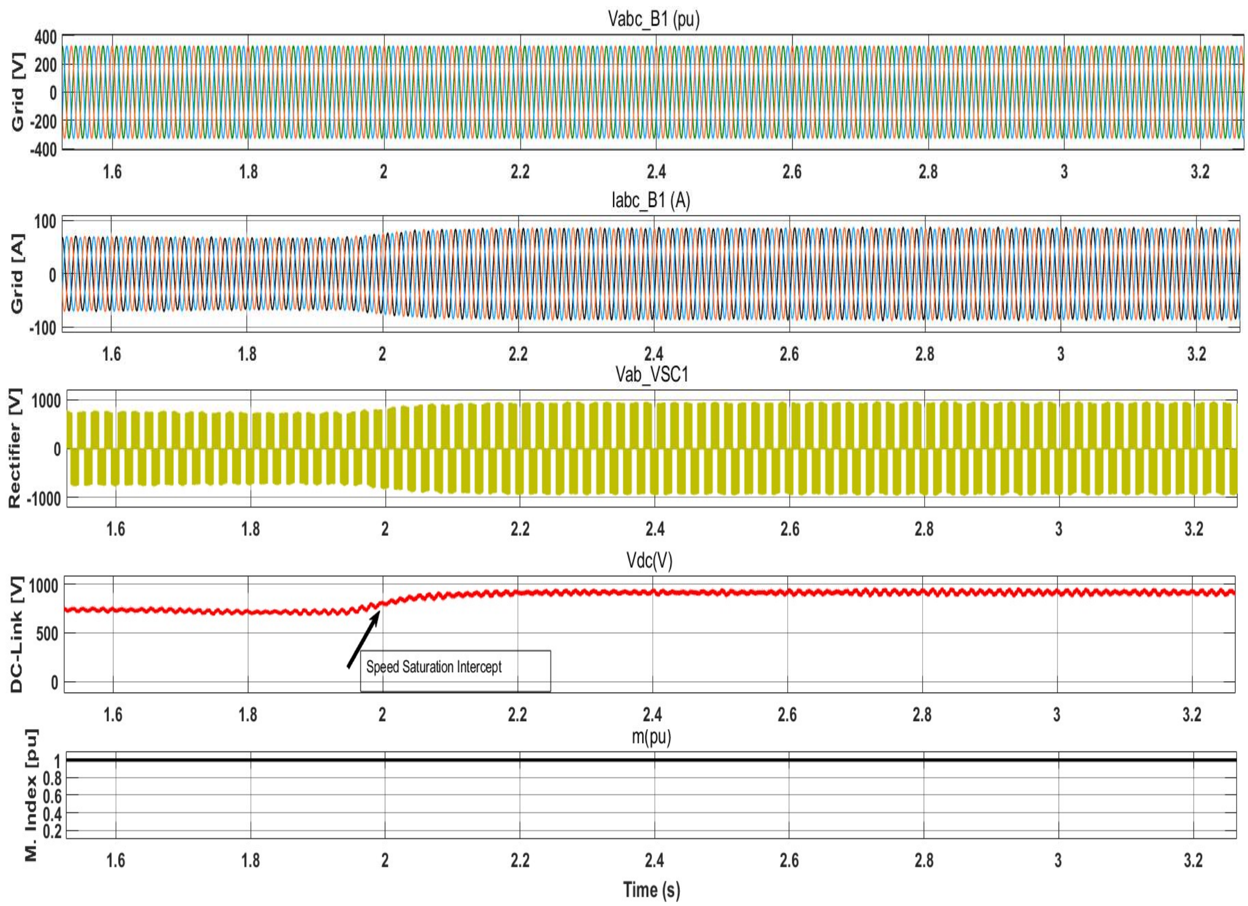

Figure 31: FESS Grid Side Voltage and Current

The output power of the grid side generator is fed into a three-phase controlled rectifier. The three-phase rectifier converts the AC voltage to a 900 VDC bus voltage as stated earlier. As shown in Figure 32, the FESS system reached steady-state speed at 2 seconds which corresponds to the maximum set point speed of 10000 rpm. The PMSG torque is shown to be a positive torque during the charging mode. This shows that the FESS is acting as a motor. At 2 seconds, after reaching the maximum set speed, the torque dropped and settled to nearly zero. Since the set-point speed and the desired stored kinetic energy is reached, no more torque is needed to keep charging or accelerating the FESS. This is also observed in PMSG rotational power plot which confirms the flow direction of energy by taking the product of torque and speed.

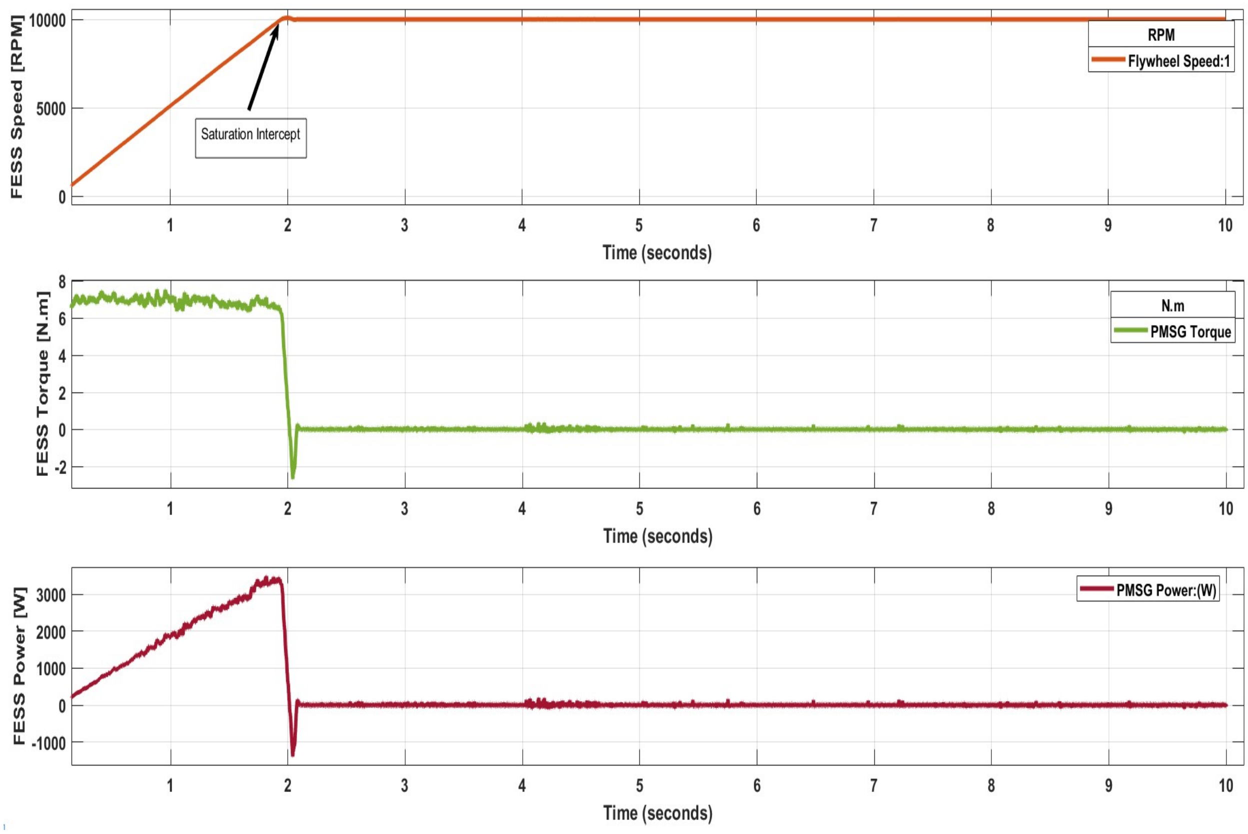

Figure 32: Simulated FEES Motoring Mode Parameters:

(a) Speed

(b) Torque

(c) Rotational Power

On the grid side synchronous machine, the exciter field current which control the amount of DC voltage applied to the machine voltage, the nominal DC field voltage induce, the machine terminal voltage along with the mechanical and electrical power waveforms are displayed in Figure 33. These waveforms will be used as guides in the remaining two test cases to display the impact of the pulsed load on the grid side machine with and without the FESS.

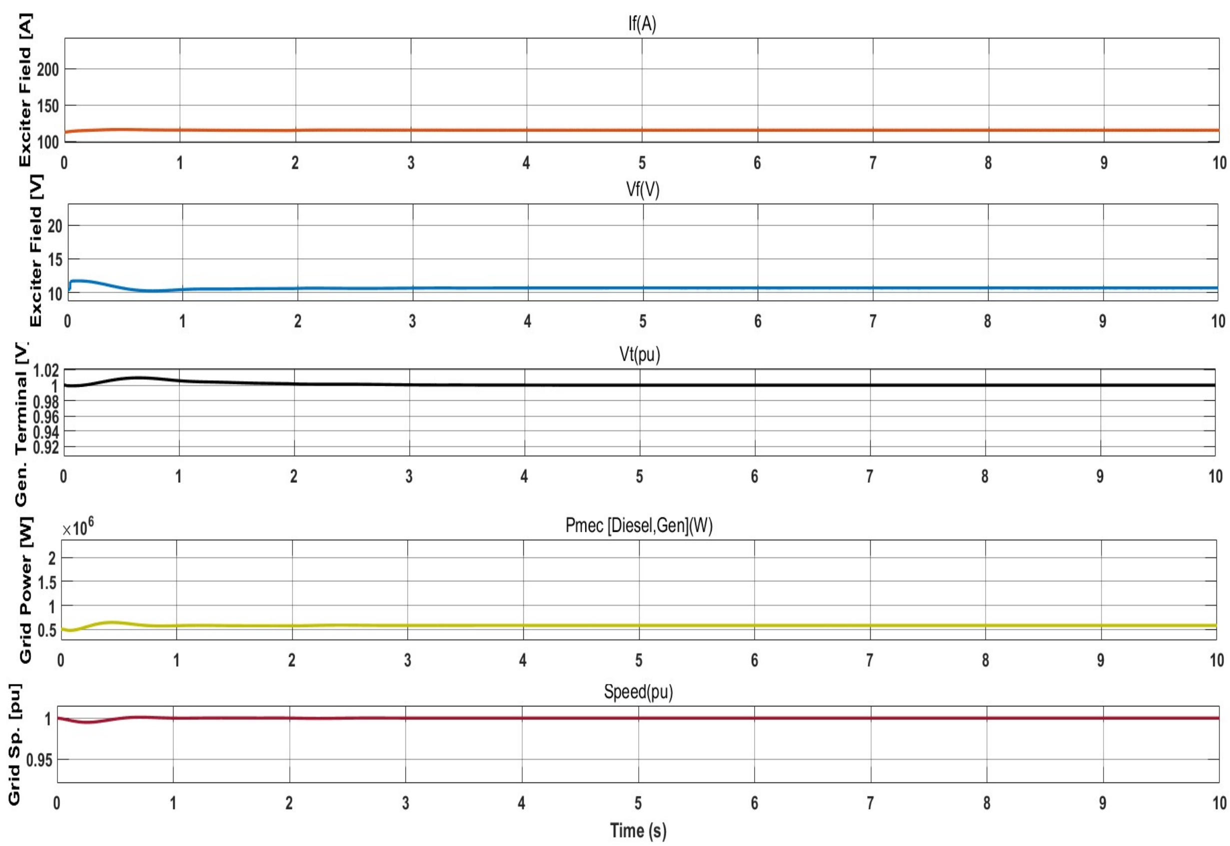

Figure 33: Synchronous Machine and Exciter Nominal Parameters:

(a) Current
(b) Voltage
(c) Mechanical Power
(d) Electrical Power

Case 2: Performance of the shipboard power distribution system without the FESS under pulsed-power load disturbance

In the second case, the simulation was repeated for another 10 seconds. At approximately 2.5 seconds after reaching steady state, a pulsed load was triggered. The charge/discharge switch remains on the charging mode which means that the FESS is still not supporting the grid. The impact of the pulsed load on the grid bus voltage and current, the grid side rectifier output voltage and the DC-link voltage are displayed in Figure 34 (a) and Figure 34 (b). All of these waveforms exhibited some severe disturbances for about 1.5s. Consequently, the entire system was unstable during the length of the operation of the pulsed load. This is unacceptable, especially during a critical mission or battle because it could be fatal to both humans and the entire ship.

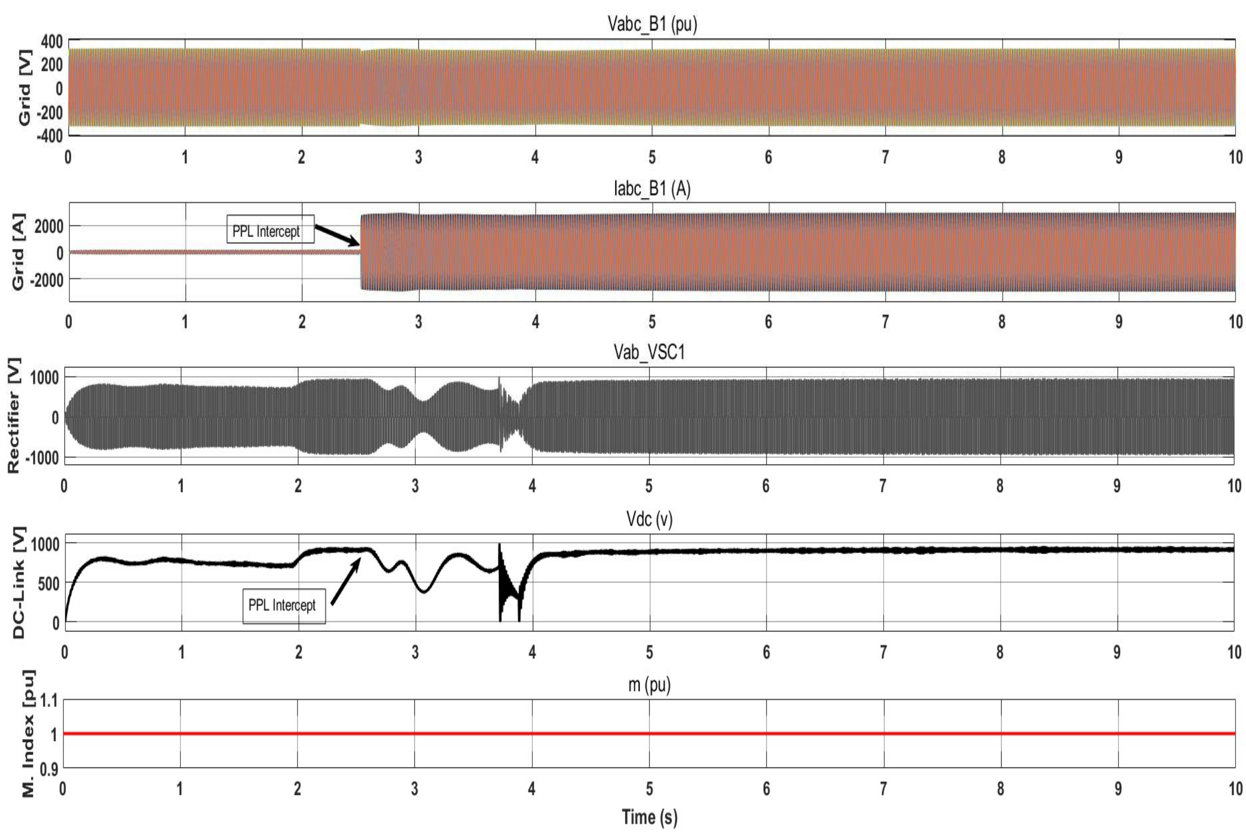

Figure 34: (a) Grid Disturbance under Pulsed-Power Load without FESS

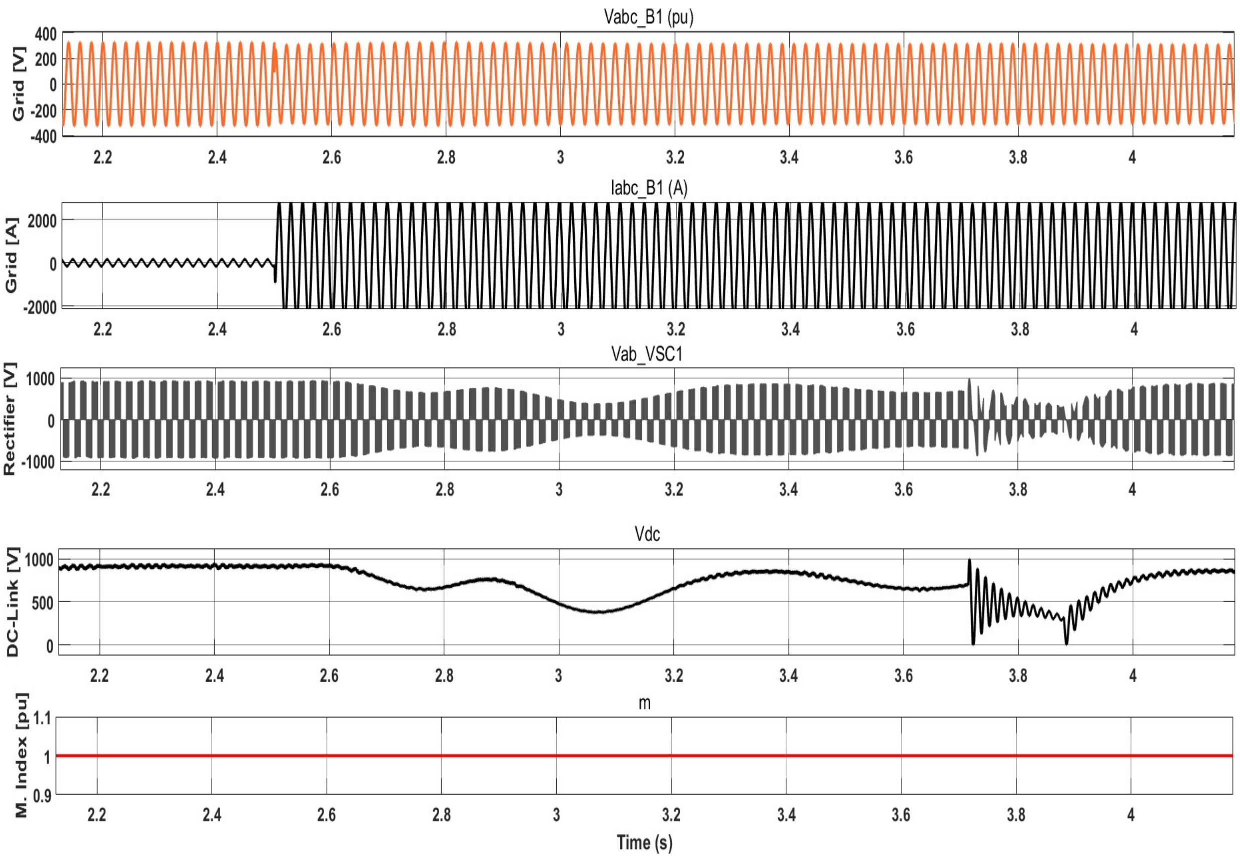

Figure 34: (b) Grid Disturbance under Pulsed-Power Load without FESS

On the machine flywheel coupling shown in Figure 35, a small disturbance is depicted only on the input torque and input power to the assembly. This could be a result of the disturbed DC-link voltage controller trying to adjust the energy going into the machine flywheel assembly. The flywheel speed exhibited no visible disturbance. This confirms what has been stated earlier. Once a flywheel reach saturation or the desired speed no other force is needed to keep the mass spinning.

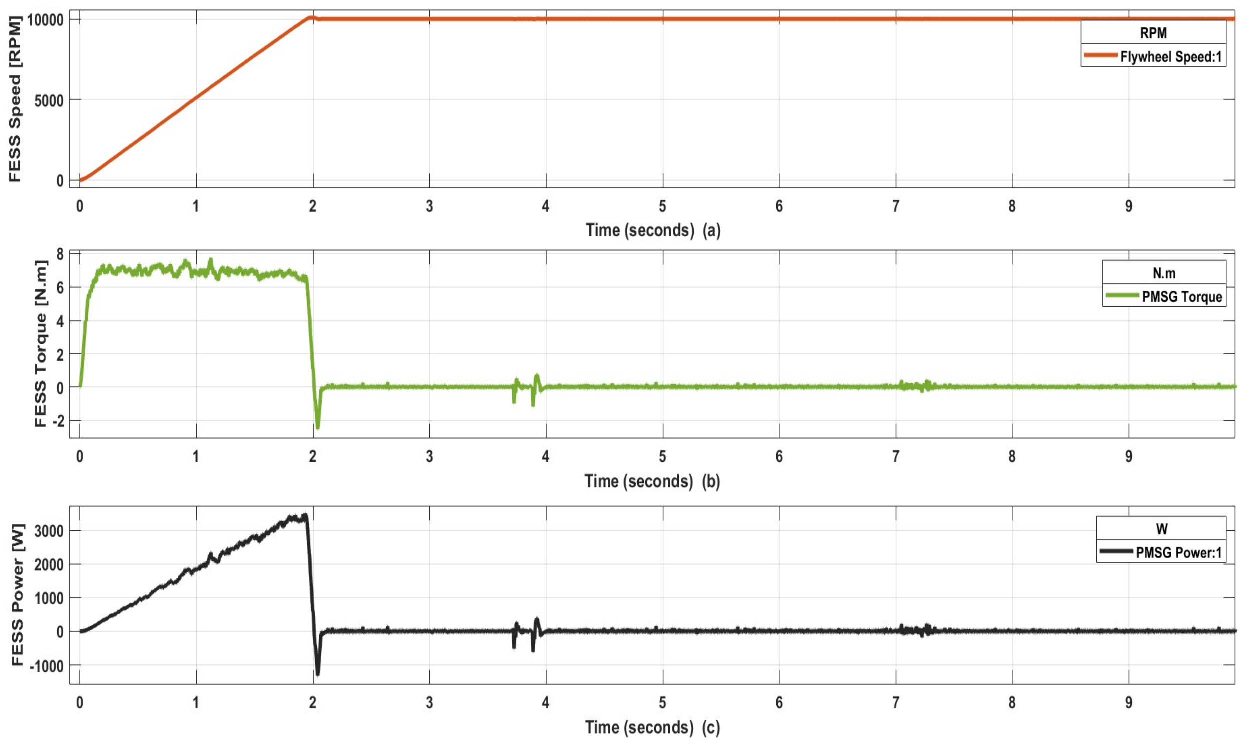

Figure 35: Simulated FEES under Pulsed-Power Load Motoring Mode:

On the grid side synchronous machine, the exciter nominal voltage and current, the synchronous machine terminal voltage, the mechanical and electrical power exhibited severe disturbances as shown in Figure 36. Earlier, it was stated that under increased loading conditions a generator tend to slow down so that more energy can be generated to balance the new power demand. Generating more power than the designed average limit results in more fuel consumption and carbon dioxide (CO2) emission as depicted in the exciter nominal field current and voltage in the figure below. This may in some cases degrade the overall system efficiency.

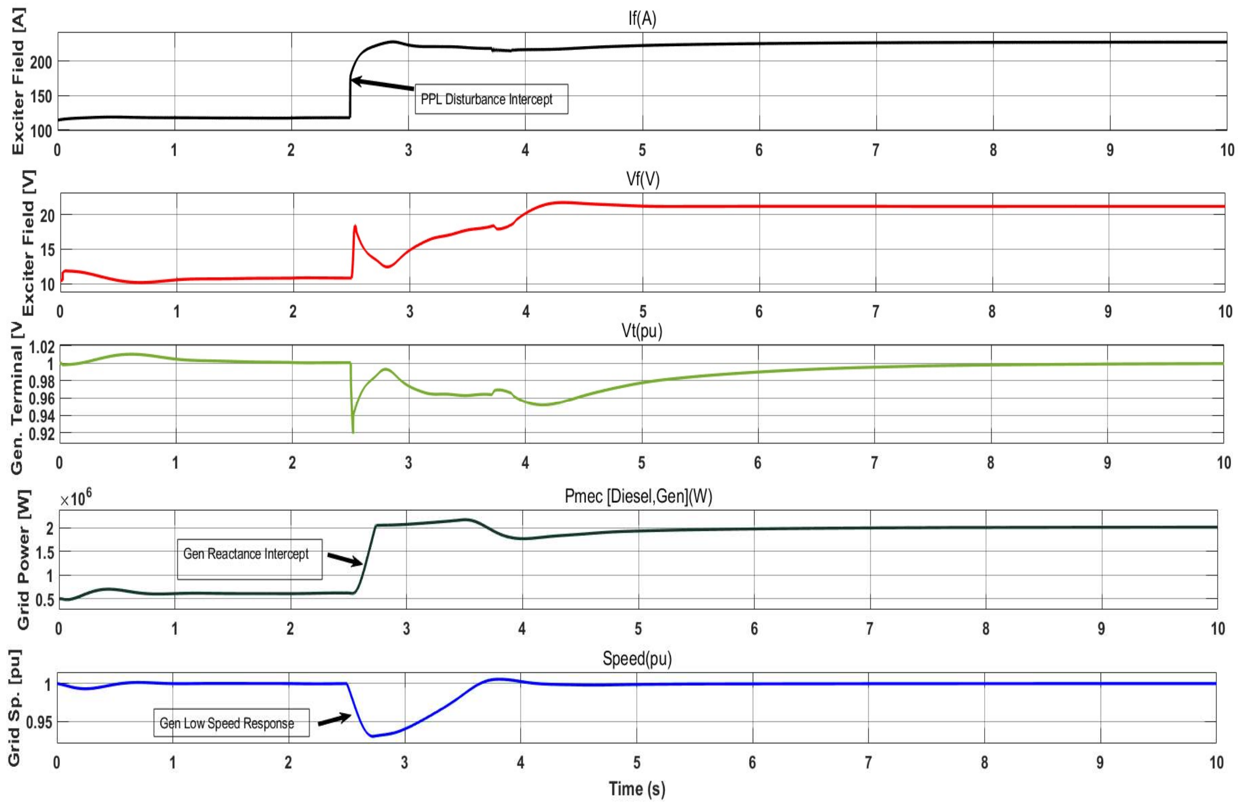

Figure 36: Synchronous Machine and Exciter Parameters under Pulsed load

Case 3: Performance of the shipboard power distribution system with the FESS under pulsed-power load disturbance

In this last step, the simulation was run for 10 seconds. At approximately 2.5 seconds after reaching steady state, a pulsed load was triggered simultaneously with the charge/discharge switch set to the discharge mode. At approximately 4 seconds, the switch was set back to its initial position (charging mode). The results indicate the sequence of the shipboard power system dynamic behavior under the developed FESS. First, as shown in Figure 37 (a) and Figure 37 (b), the grid bus voltage and current display a negligible disturbance when compared to Figure 34 (a) and 34 (b). As for the DC-link voltage, no disturbance is noted except when the charge/discharge switch was set back to its normal position at 4s.

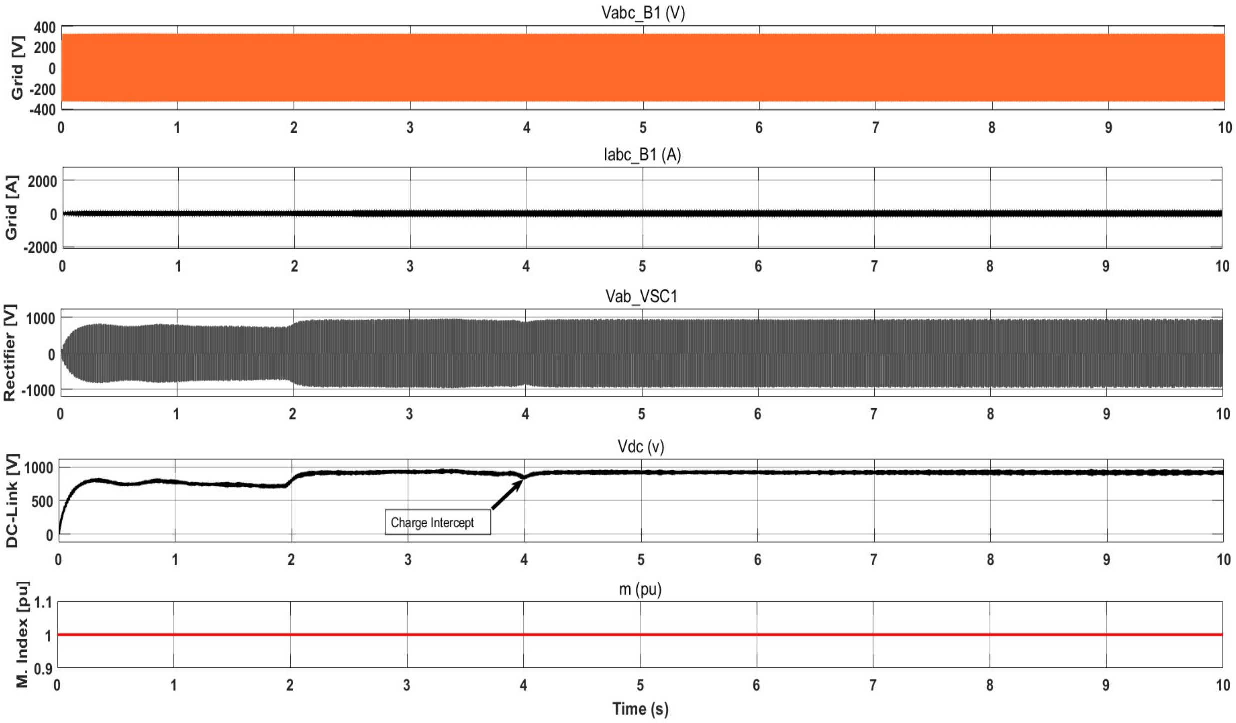

Figure 37 (a): Grid Disturbance under Pulsed-Power Load with FESS

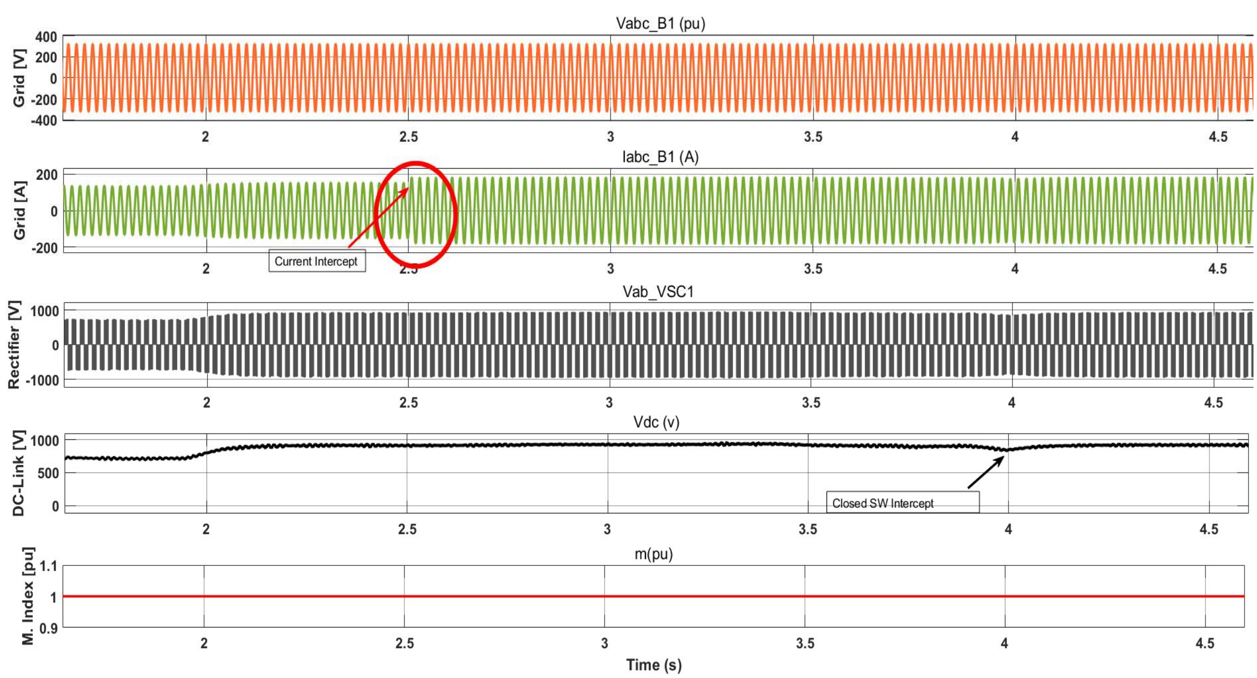

Figure 37 (b): Grid Disturbance under Pulsed-Power Load with FESS

On the flywheel machine assembly, a drop in the FESS speed waveform at 2.5 seconds is noted on Figure 38. Then, at 4 seconds when the switch was set back to its initial position, the FESS recharges the supplied energy. A positive and negative torque in the graph of the PMSG shows that the FESS acted as a motor during the charging mode and as a generator during the discharging mode, which is also seen in the PMSG rotational power plot. The fluctuation shown in both the torque and the power waveforms are normal FESS operation waveforms response.

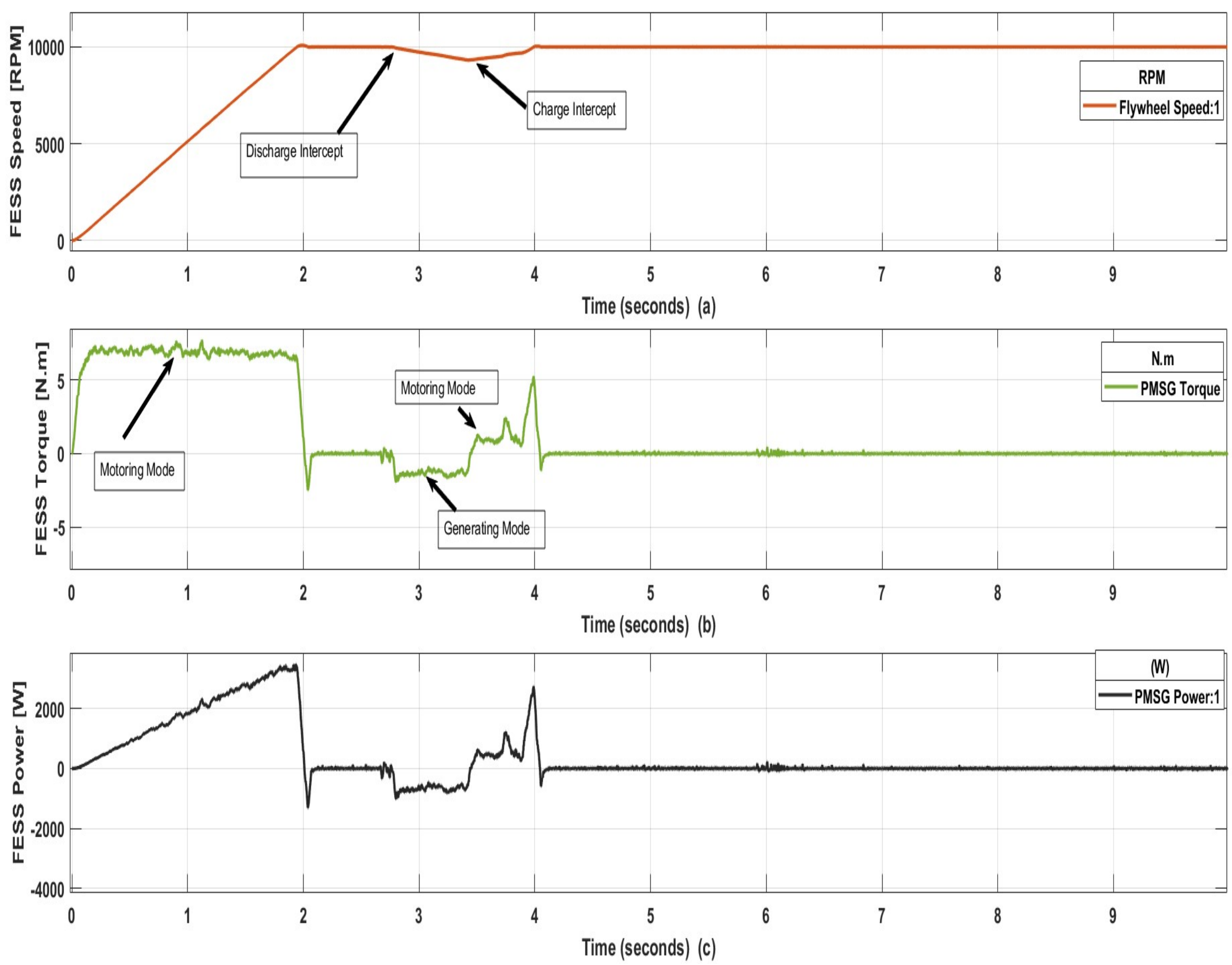

Figure 38: Simulated FEES under Pulsed-Power Load Disturbance

On the grid synchronous machine, as shown in Figure 39, the exciter nominal voltage, current, the machine terminal voltage, mechanical and electrical exhibit a very low disturbance as shown when compared to the system response obtained in Figure 36.

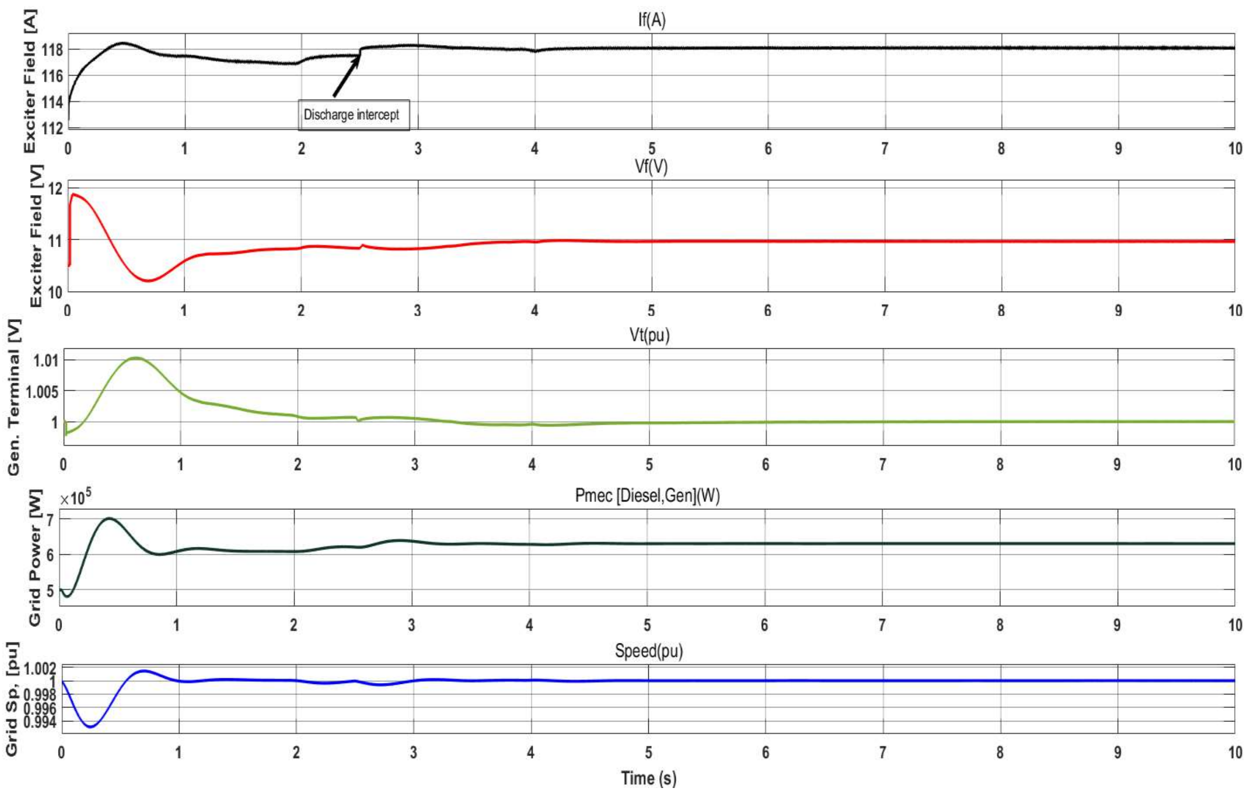

Figure 39: Synchronous Machine and Exciter Nominal Current, Voltage, Terminal Voltage and Mechanical and Electrical Power under Pulsed Load with FESSS

3.4 CONCLUSION

In this chapter, a FESS based on a permanent magnet synchronous machine mathematical equation was derived using a D-Q rotational reference frame transformation. One of the advantages that this D-Q transformation (also called Park transformation) offers is to enable a decoupling grid instantaneous active and reactive current. Thus, system charging/motoring mode is derived from an error signal between the reference speed and the rotor speed. This error signal is used to generate the reactive current needed to generate the desired torque so that the appropriate momentum is created for the targeted kinetic energy. The generating or discharging mode is obtained through the same reactive current as shown above, but from an error between a reference DC-link voltage and a measured DC bus voltage. Grid auto correction or voltage sag function was then replaced by an operator mechanical switch. The developed system performance was verified by comparing the time domain electrical responses with and without FESS operation. The shipboard power distribution system dynamic transient under pulsed-power load with the developed FESS displayed a balanced power, and an enhanced system overall transient stability throughout operation.

CHAPTER 4

MODELING AND PERFORMANCE OF SHIPBOARD MVDC SYSTEMS

4.1 SHIPBOARD MVDC SYSTEMS MODELING

A notional MVDC shipboard power distribution system as shown in Figure 40 consists of a two zone 12 kV distribution bus system. Zonal distribution system 1 consists of one power generation module (PGM) 1, one power conversion module (PCM) 1, a pulsed-power load, four cables section (CS_X), two switchboards (SWB_A and SWB_B), and tow disconnect switches. Zonal distribution system 2 consists of a power generation module PGM2, two propulsion motor modules PMM, one power conversion module PCM2, six cables section, two switchboards (SWB_C and SWB_D), and four disconnect switches. The two zones are linked together by two disconnect switches along the port and starboard side.

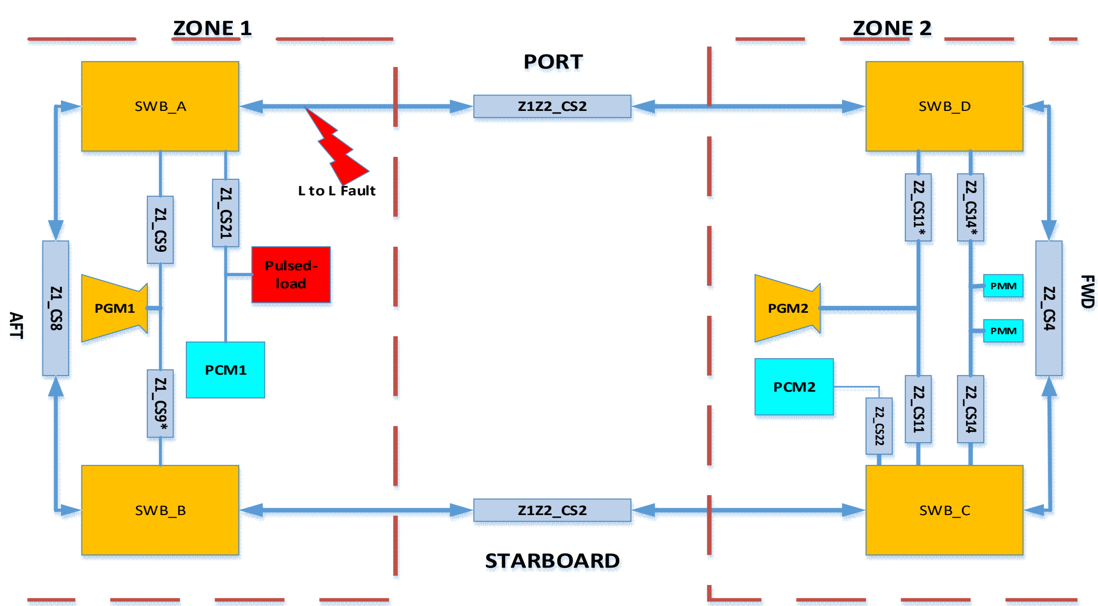

Figure 40: A Notional MVDC Shipboard Power Distribution System

4.1.1 Power Generation Modules

The Power Generation Modules (PGM) are modelled as gas turbine driven synchronous generators rated at 45 MVA, 240 Hz, 6-pulse. Both PGMs are operated at 240 Hz with their apparent power rating gradually increased to 45 MVA to manage the reactive power required by the thyristor-controlled rectifiers (TCR). The synchronous machine controllers used in the distribution system are described in [74], [75]. The machine controller's configuration set-points given in Tables 3 to Tables 5 were derived from those used in [74].

Constant	**Description**	**Setpoint**
PW	Generation Power	72 MW
Mmva	Rated MVA of the Machine	45 MVA
cfqr	Number of Q-axis Rotor Windings	1
Vbsll	Rated Line Voltage	13.8 kV AC
HTZ	Base Frequency	240 Hz
H	Inertia Constant	4 MWs/MVA
D	Synchronous Mechanical Damping	0.04 pu/pu
Xa	Stator Leakage Reactance	0.08 pu
Xd	D-axis Unsaturated Reactance	1.352 pu
Xd'	D-axis Unsaturated Transient Reactance	0.296 pu
Xd"	D-axis Unsaturated Sub-Transient Reactance	0.148 pu
Xq	Q-axis Unsaturated Reactance	0.836 pu

Table 3: Synchronous Machine Constants

Constants	Description	Setpoint
R	Permanent Droop	1e-6 pu
T1	Governor Mechanism Time Constant	0.005 sec
T2	Combustion Chamber Time Constant	0.04 sec
T3	Exhaust Temperature Measurement Time Constant	0.01 sec
AT	Ambient Temperature Load Limit	0.9 pu
Kt	Maximum Turbine Power	2
Vmax	Maximum Turbine Power	0.8 pu
Vmin	Minimum Turbine Power	0 pu
Dturb	Turbine Damping Coefficient	0.03

Table 4: Gas Turbine Constants

Constants	Description	Setpoint
Tr	Filter Time Constant	0.001 sec
Tb	Lead-lag Denominator Time Constant	0.1 sec
Tc	Lead-lag Numerator Time Constant	0.2 sec
Ka	Voltage Regulator Gain	80
VAmax	Maximum Control Element Output	15 pu
VAmin	Minimum Control Element Output	-15 pu
Te	Exciter Time Constant	0.2 sec
Kf	Rate Feedback Gain	0.03 pu
Tf	Rate Feedback Time Constant	1.49 sec
Kc	Rectifier Regulation Factor	1 pu
Kd	Exciter Internal Reactance	0.4 pu
Ke	Exciter Field Resistance Constant	1 pu
E1	Value of E at Se1	4 pu
Se1	Value of Se at E1	0.4
E2	Value of E at Se2	5 pu
Se2	Value of Se at E2	0.5
Cal	Saturation Constant ‘A’ Calculation Method	abs(A)
VRmax	Voltage Regulator Maximum Output	14.99 pu
VRmin	Voltage Regulator Minimum Output	-14.99 pu

Table 5: Exciter Constants

4.1.2 Thyristor Controlled Rectifier

The output of both gas turbine synchronous machines is fed into their corresponding six pulsed TCRs. TCRs are used here because of their ability to control the DC output for voltage regulation. Furthermore, they can provide high power transfer and high voltage switching frequency. In this design, the two zonal TCRs convert the 45 MVA AC input voltage to a 12 kV DC bus voltage, a firing angle for the TCR is chosen along with a firing pulse generator [74]. The TCR configuration set-points given in Table 6 were derived from those used in [74].

Constants	**Description**	**Setpoint**
TMVA	TCR Rating	45 MVA
Vbspr	Rated RMS L-L Primary Voltage	9.8 kV
Freq	Rated Frequency	240 Hz
Rp	Positive Sequence Resistance	0.0 pu
Lp	Positive Sequence Reactance	0.01 pu
SnR	Valve Snubber Resistance	1000 Ω
SnC	Valve Snubber Capacitance	25 μF
RON	Valve ON Resistance	0.001 Ω
ROFF	Valve OFF Resistance	1e9 Ω
RLdc	Output Reactor resistance	0.075 Ω
LLdc	Output Reactor Inductance	790

Table 6: TCR Constants

4.1.3 Power Conversion Modules

In this dissertation the Power Conversion Module (PCM) of each zone is modeled as a constant impedance type with a resistive load directly connected to the 12 kV DC bus. PCM1 is rated at 7.2 MW and PCM2 is rated at 1.44 MW. However, the primary purposes of PCM are to convert input power and to protect in-zone generation bus against system fault (s). PCM can either use their natural built-in property called current limiting mode to protect the generation bus. This is done by limiting the amount of current drawn from the power system to prevent bus voltage to collapse. PCM also protects the generation bus by isolating faulty circuitry or tripping the in-zone circuit breaker. Figure 41 exhibit the PCM used in the design system.

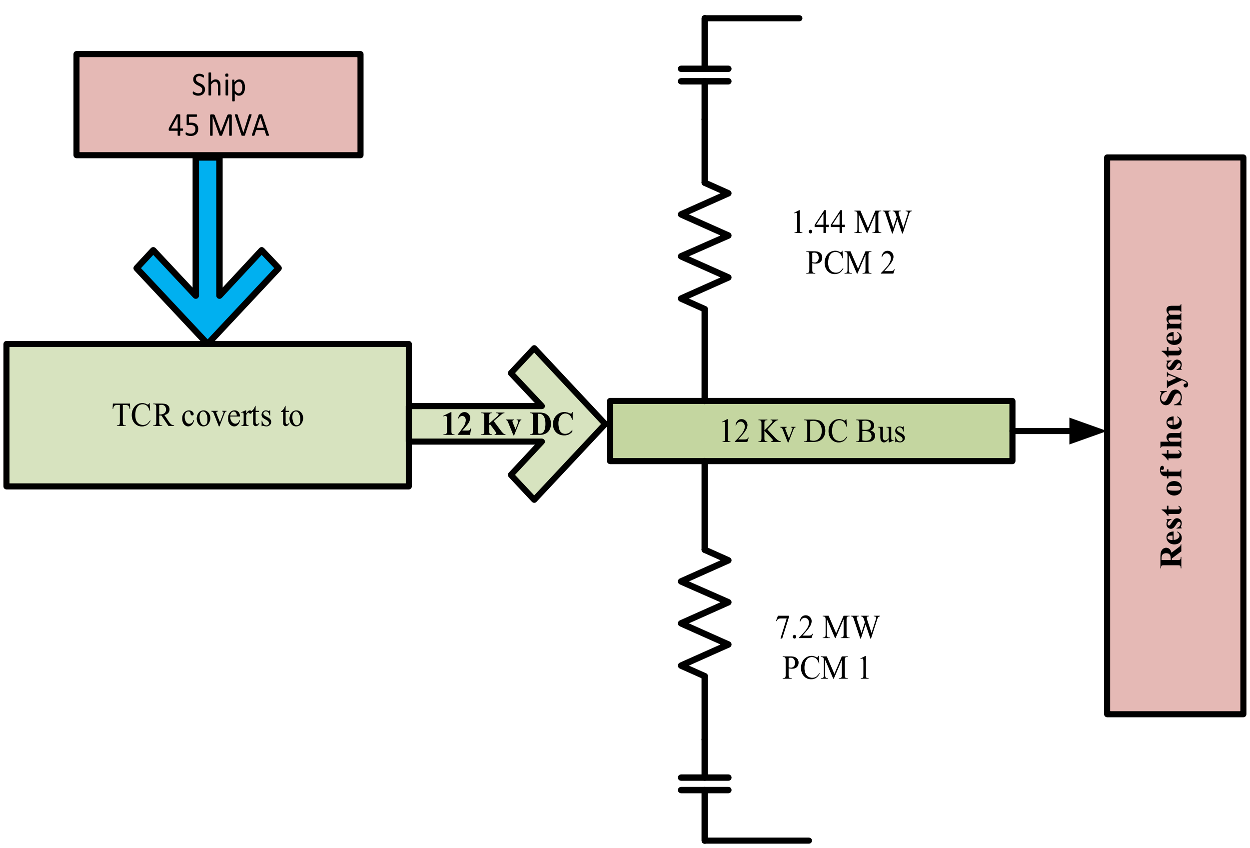

Figure 41: MVDC System PCM Modules

4.1.4 Pulsed-Power Load Module

A 1.44 MW pulsed-power load is implemented in Zone 1 as shown in Figure 42. It is designed as a variable resistive load directly connected to the 12 kV bus. To enable system pulsed studies, load controls have been implemented in the model. Pulsed-load discharge time can be set and applied at any point on the DC bus on demand by a user.

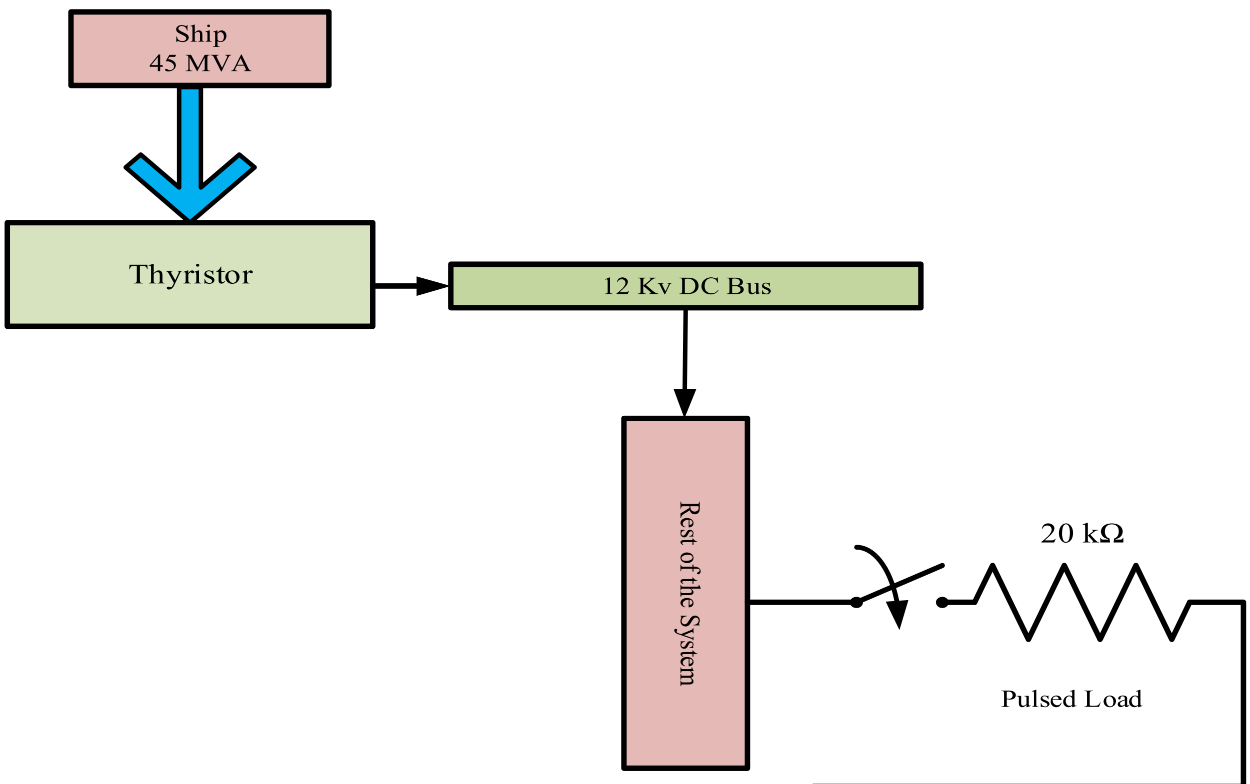

Figure 42: MVDC Pulsed-Power Load

4.1.5 MVDC Systems Fault Control Blocks

To enable fault investigation, two types of fault control blocks have been implemented in the MVDC system. The fault blocks enable the representation of an electrical fault as an instantaneous change in the impedance. Three different mechanisms can be used to trigger a fault using these fault blocks.

- A fault can be triggered at a specific time. In this studied system the fault (s) were triggered after reaching steady state so that the true fault dynamic transient can be captured.
- A fault can be triggered when a predefined bus voltage or current range is exceeded.
- A fault can be triggered when an external trigger signal goes high or low.

During normal operation the resistance value between the two fault block ports is infinity, which means open contacts. Upon occurrence of a fault, the resistance between the two ports change to the default value of 0.003 ohms and the output of the fault block change state from 0 to 1. In this dissertation, a fault block is applied to the 12 KV DC bus line to line and on bus line to ground. A fault block representation used is shown in Figure 43.

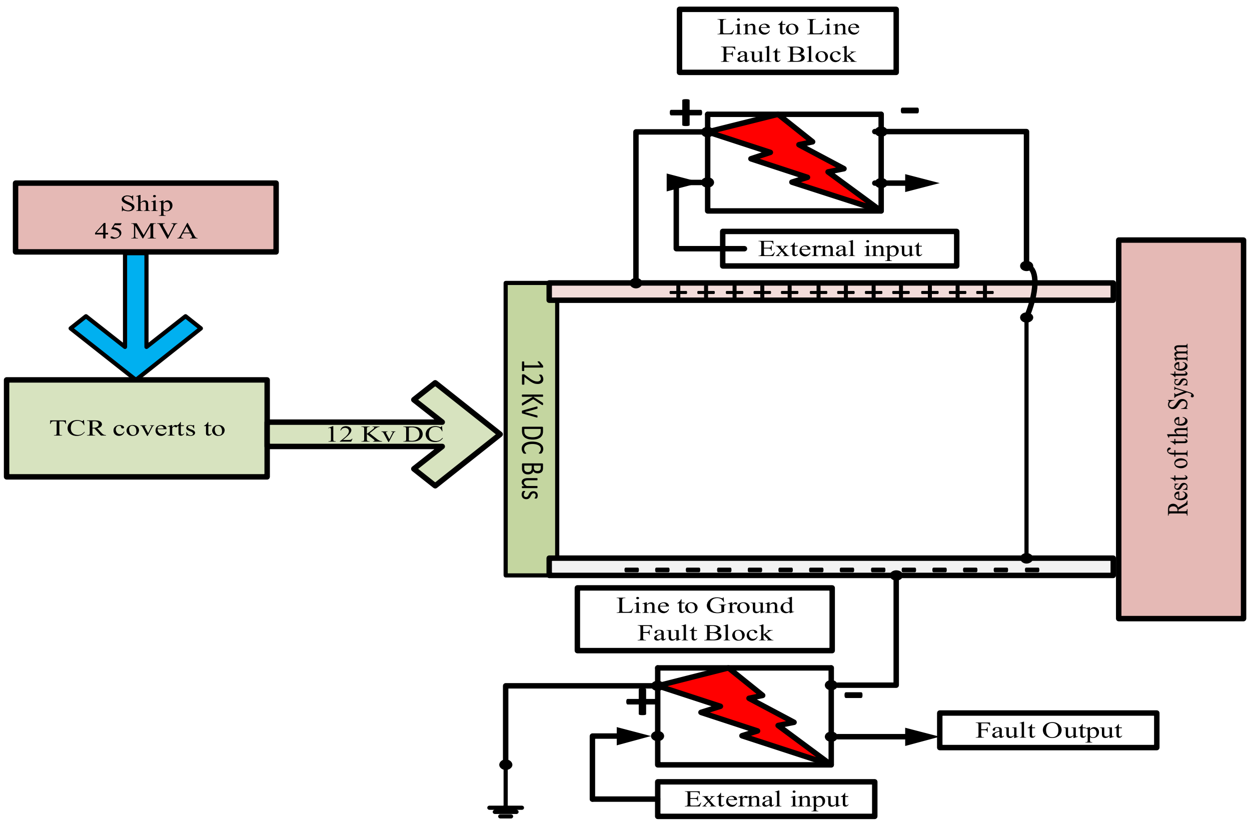

Figure 43: Shipboard MVDC System Faults Blocks Schematic

4.1.6 Propulsion Motor Modules

Two 18 MW Propulsion Motor Modules (PPM) are implemented in Zone 2 as shown in Figure 44. The PPMs are designed as a constant resistive load directly fed from the 12 kV distribution bus. The disconnect switch arrangement allows the PPMs to be fed from either the port or the starboard side. They also enable power to be fed to the PPMs equally from both the port and the starboard side.

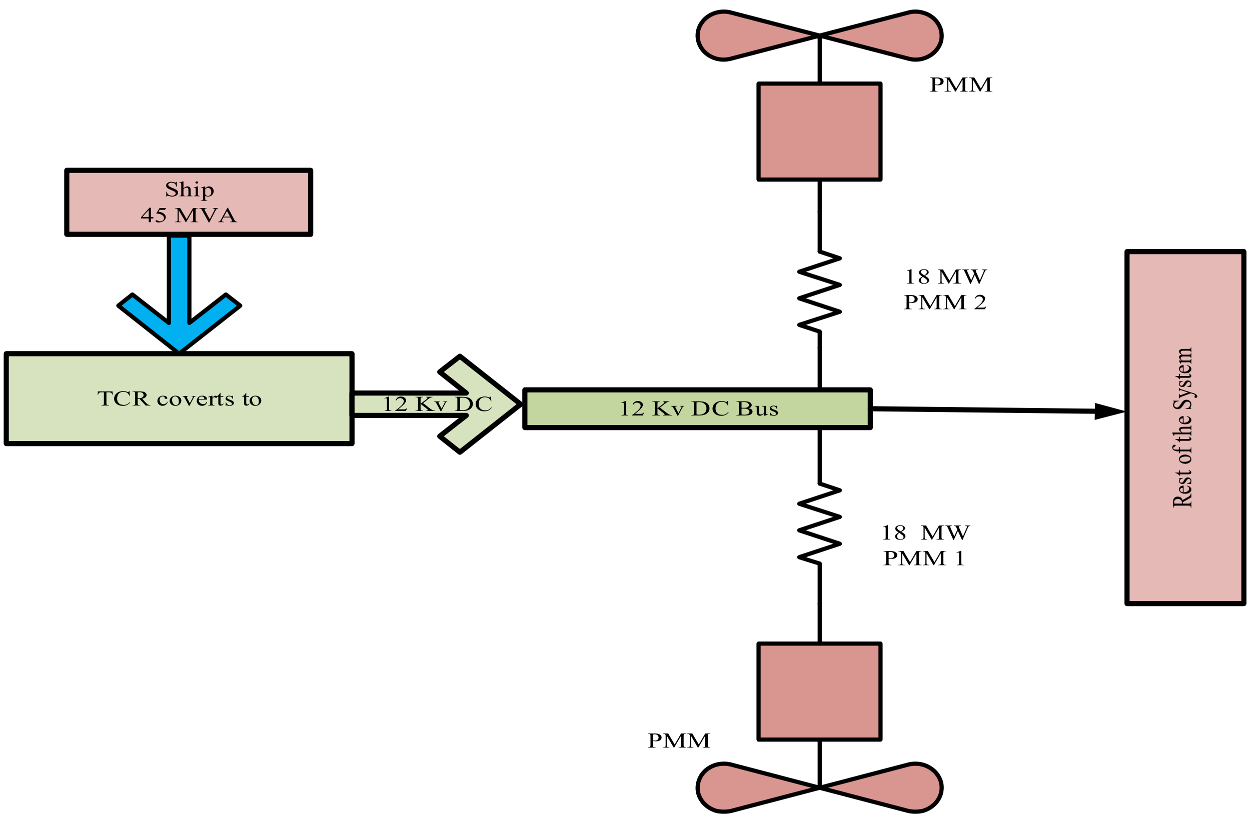

Figure 44: Shipboard MVDC System Zone 2 PMMs

4.1.7 MVDC Systems Cable Sections

The cable sections model is described in [74] with a resistance inductance in series with breakers. The cable impedance set points are derived from reference [76] data and are tabulated in Table 7.

Zone cables	Location	Length (m)	Resistance (mΩ)	Inductance (µH)
Z1Z2_CS2	Port Mid ship	29.5	0.21	3.47
Z2_CS4	Forward (FWD) Center line (CL)	29.5	0.21	3.47
Z1Z2_CS6	Starboard Mid Ship	29.5	0.21	3.47
Z1_CS8	AFT Centerline	41.75	0.3	4.91
Z1_CS9	AFT Port	22.4	0.16	2.63
Z1_CS9*	AFT Starboard	22.4	0.16	2.63
Z2_CS11	FWD Port	45.2	0.32	5.32
Z2_CS11*	FWD AFT	45.2	0.32	5.32
Z2_CS14	FWD Port	29.1	0.21	3.42
Z2_CS14*	FWD Starboard	29.1	0.21	3.42
Z1_CS21	AFT Port	18.2	0.26	4.3
Z2_CS22	FWD Starboard	20.1	0.28	4.73

Table 7: Cable Sections Set Points

4.1.8 MVDC Systems Disconnect Switch

Disconnect switches (Z1Z2_CS2, Z2_CS4, Z1Z2_CS6, Z1_CS8) are implemented in the model as shown in Figure 40 along the 12 kV main bus. The goal is to add a ring bus topology to the zonal distribution system by providing a connect/disconnect switch between the two zones, FWD and AFT as well as port and starboard. Furthermore, through these switches, power can be rerouted on demand. Table 8 provides the ON/OFF set-point of the single-phase disconnect switches.

Disconnect Switch Resistance	Default Set-Point	Min Set-Point	Max Set-Point
OFF	1e9 Ω	0.001 Ω	N/A
ON	0.001 Ω	0.001 Ω	N/A

Table 8: Disconnect Switch Constants

4.2 SHIPBOARD MVDC SYSTEM SIMULATION AND PERFORMANCE

To investigate and analyze the system dynamic transient performance, the MVDC system was subject to some transient disturbances such as pulsed-power load and bus faults. Therefore, in this section, the 45 MVA, 240 Hz, 6-pulse and 12 kV shipboard MVDC system is simulated using the MATLAB Simscape package. The IEEE grounding Standard 1709 midpoint grounding arrangement is adopted in the MVDC system as described in [77]. Thus, the DC bus negative and positive voltage lines are each tied to a 2.5kΩ ground resistor and parallel to the capacitors as shown in Figure 45. This will enable a reference point for the MVDC bus to establish voltage balancing. Without a DC path to ground, the presence of even small leakage currents can cause an unpredictable DC offset. One advantage of the midpoint grounding system is that the equipment requires an insulation level of half voltage to ground. Another advantage, if the system is properly designed, the system can operate in emergency at half power with one of the buses out of services.

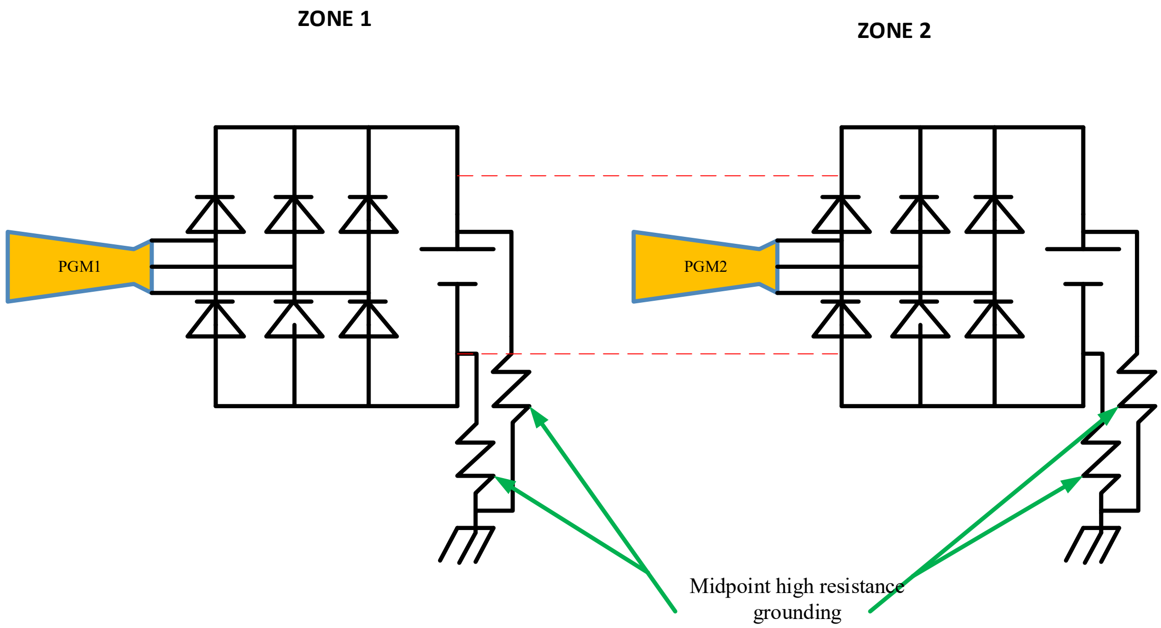

Figure 45: MVDC Midpoint Grounding System

Case 1: Normal Operation Run

The simulation was run for 3 seconds, and the grid side power generation module three-phase voltages and current responses were captured and displayed in Figure 4.6. The DC bus voltage looks very clean which implies a heavy filtering by either the choke or the capacitor. The current signatures for both generation units were also captured and presented in Figure 47. They show slide voltage notching distortions because of the rectification of the machine AC voltage.

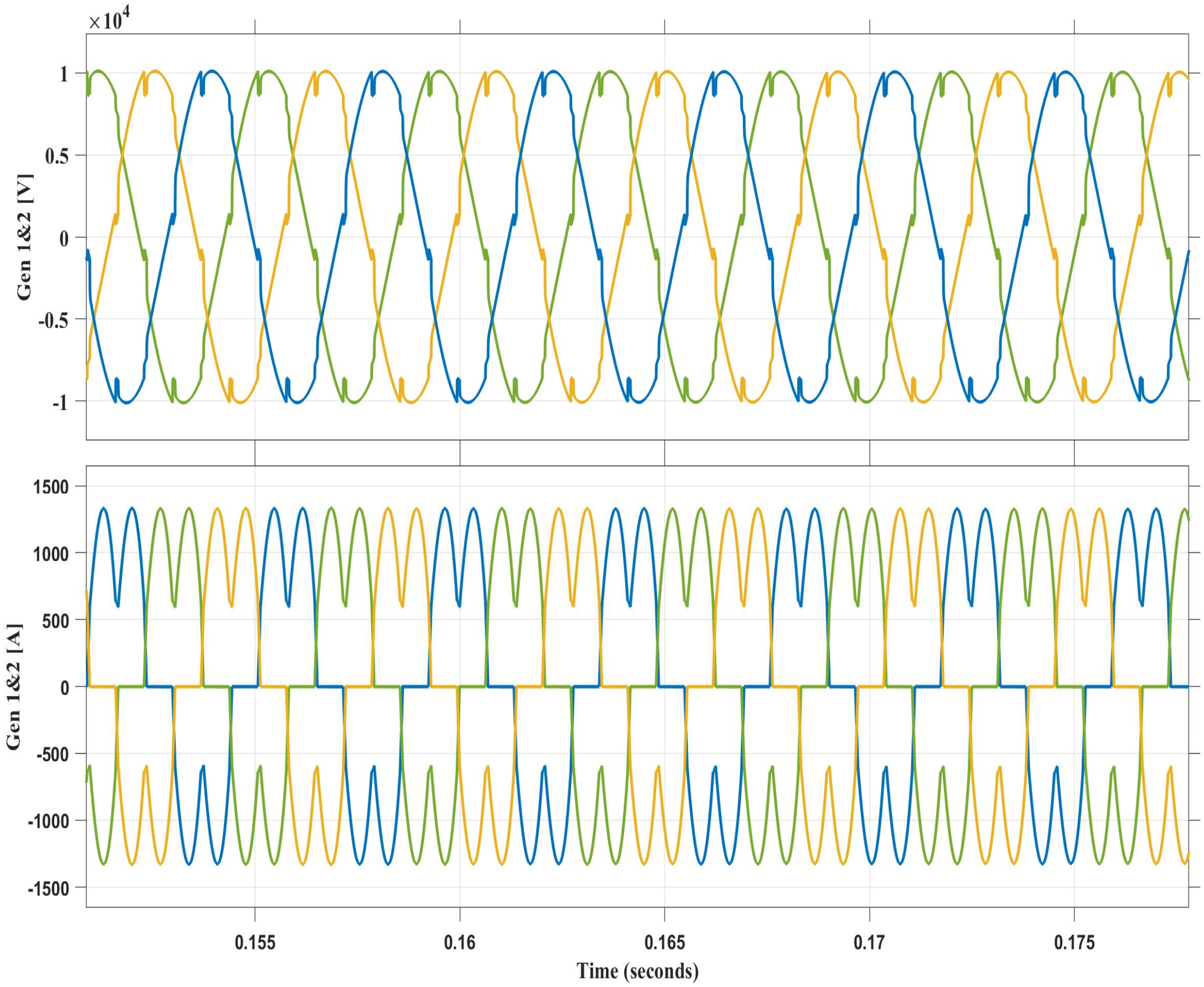

Figure 46: MVDC Generator Voltage & Current Normal Operation

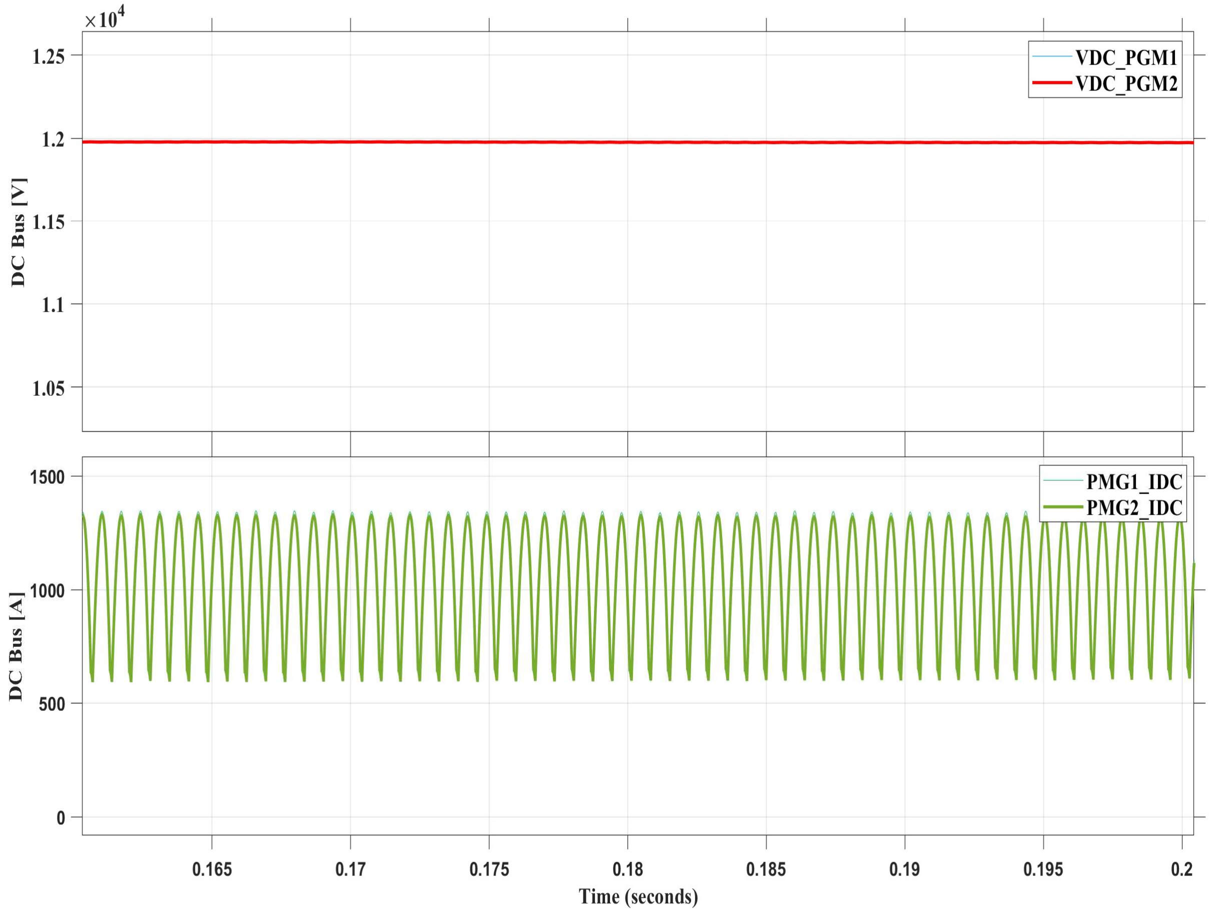

Figure 4.7: Zonal MVDC System Bus Voltage & Current Normal Operation

Case 2: Pulsed-Power Load Signatures

To understand the impact of pulsed-power load on the system, a second run was performed. During the simulation, the pulsed load was triggered at 2 seconds. Figure 48 shows a momentary grid voltage and current distortion because of the pulsed load. The drop in the voltage is justified by the generator's natural response to an increase in the system loading. Generators tend to slow down which is usually shown in their RPM so that more torque can be picked up in reaction to a load increase. The spike shown on the grid current is the torque response applied to the engine rotor. The 5ms distortion time is a result of the generator's quick response to the pulsed load. The aim of this research is not to investigate the impact of PPT on grid side, but to show 1) PPT effectively contributing short duration power injection for PPT and 2) to advise future work to investigate on increased pulsed-power time constant in order to study current and voltage distortion impacts and duration.

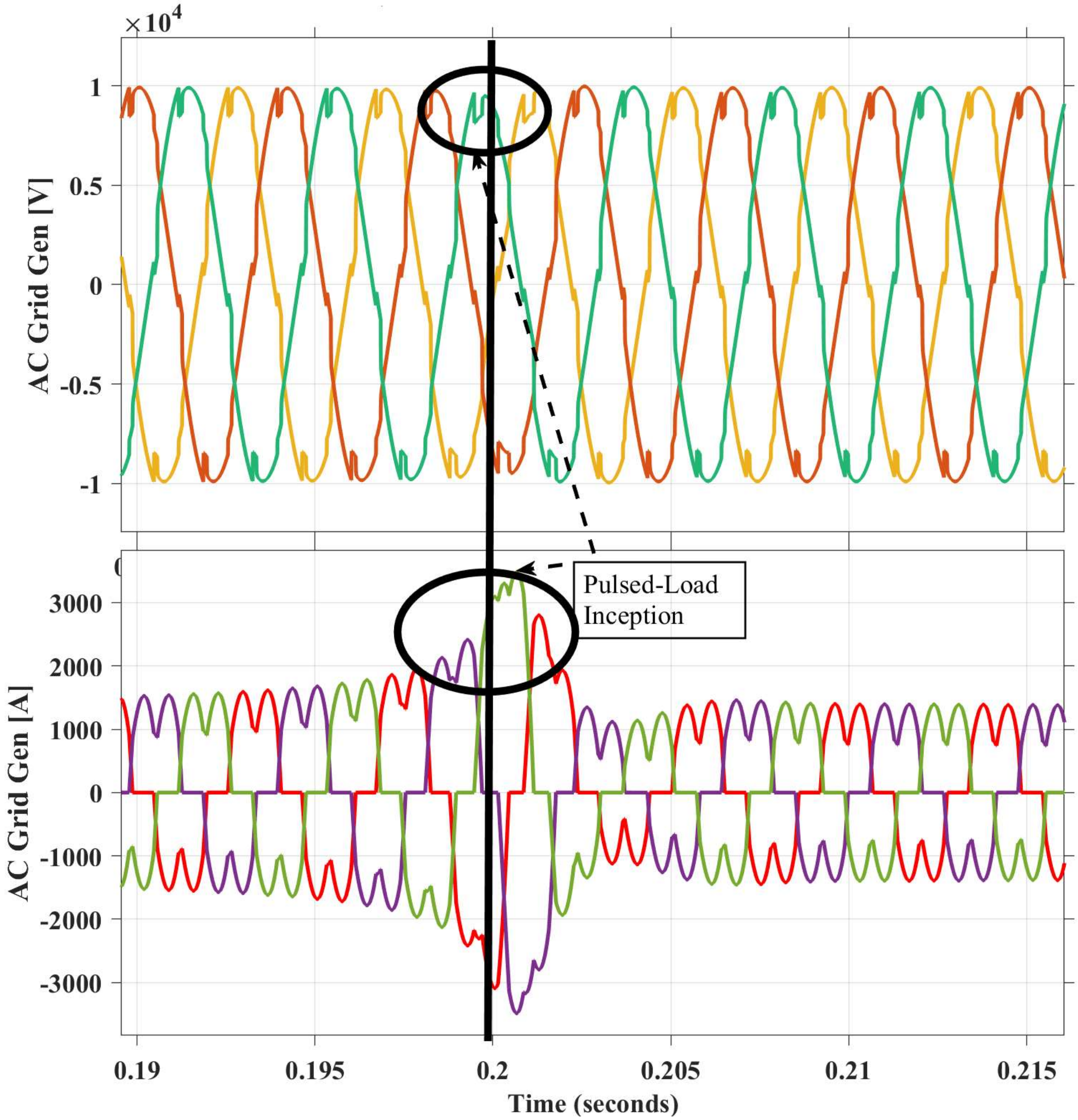

Figure 48: Pulsed-Load Signature on the Grid Generator

On the DC bus side, bus voltage and current disturbance were also noted as displayed in Figure 49. This is an expected system response since no energy storage is tied into the DC bus. An interesting factor here was noted. It took the bus voltage about 0.106 second to stabilize while it only took the bus current 0.061 seconds.

This is an unexpected discovery because it is not observed in typical shipboard power distribution systems between grid voltage and current settling time. A pulsed-power load disturbance on a conventional (AC) shipboard power distribution system is defined by a short bus voltage drop and a short bus current spike. Generally, the settling time difference between the disturbed bus voltage and current is not noticeable. In the proposed technique, a numerical error of about 4.5% is noted with a lagging voltage settling time. In AC systems, transformers are used to interface loads and to provide galvanic protection. On MVDC distribution systems, these transformers are replaced with power electronics. Power electronics do not provide galvanic protection, but they do have their own built-in natural protection, which entails switching between voltage or current limiting modes. Therefore, the numerical error recorded between the bus voltage and current on the MVDC system may have been a result of:

- The thyristor switching from a voltage limiting mode to current limiting mode to try to protect the DC distribution system against the current surge.
- A slow response induced by the rectifier PI controller while waiting for the error signal.
- The system time constant $\left(T = \frac{L}{R}\right)$.
- The grid side AVR system.

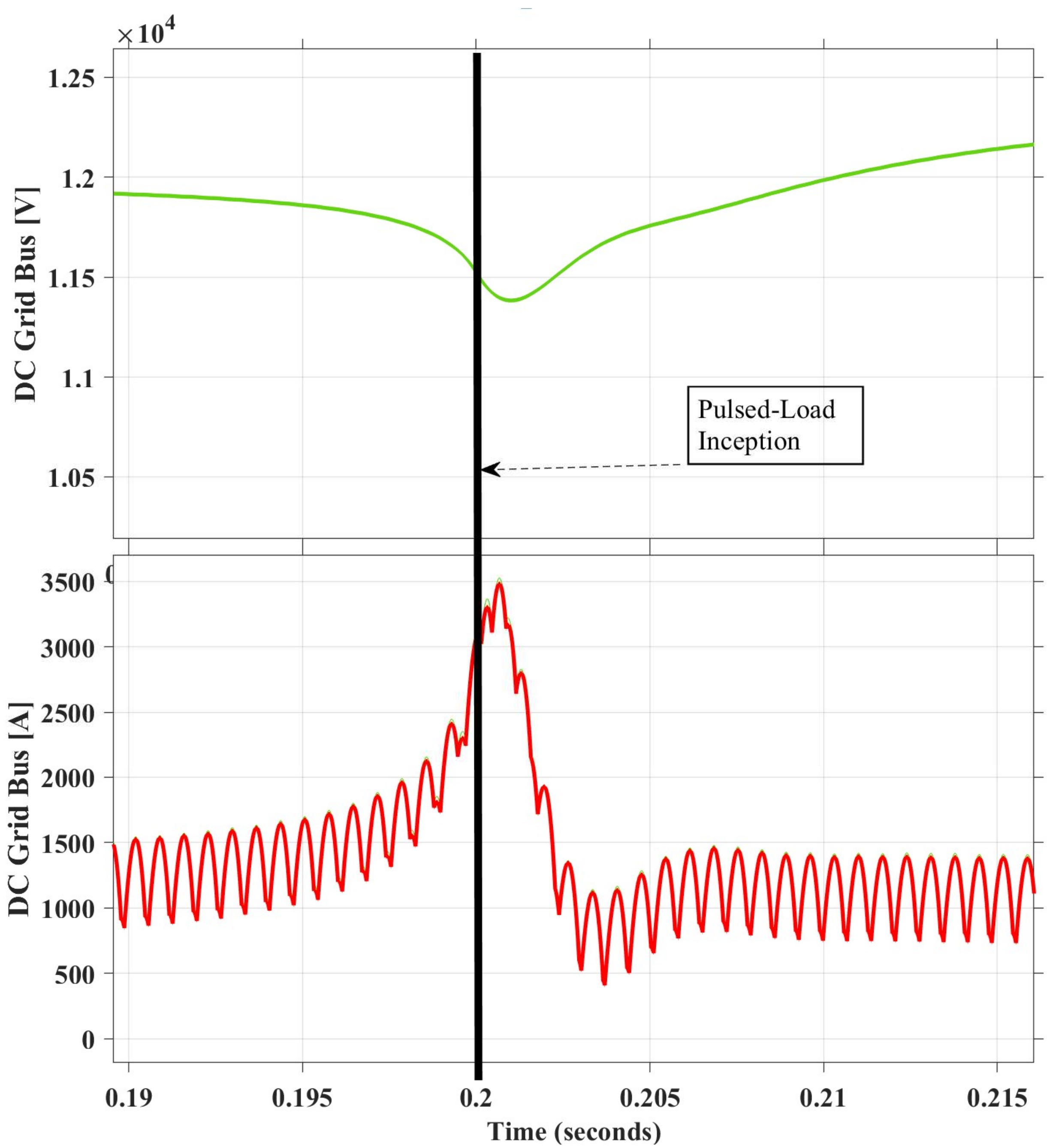

Figure 49: Pulsed-Load Signature on the DC Bus Voltage & Current

Case 3: Pulsed-power load profile at 100-, 300-, and 1000-Kw Signatures

In this section, the shipboard MVDC system was subject to different pulsed-power load profiles. The dynamic transient disturbances recorded are depicted from Figure 50 to 55. This transient response shows that both the AC and DC grid voltage and current disturbances are directly proportional to a PPL profile. As the loading increases, the disturbance amplitude of both the voltage and current increases.

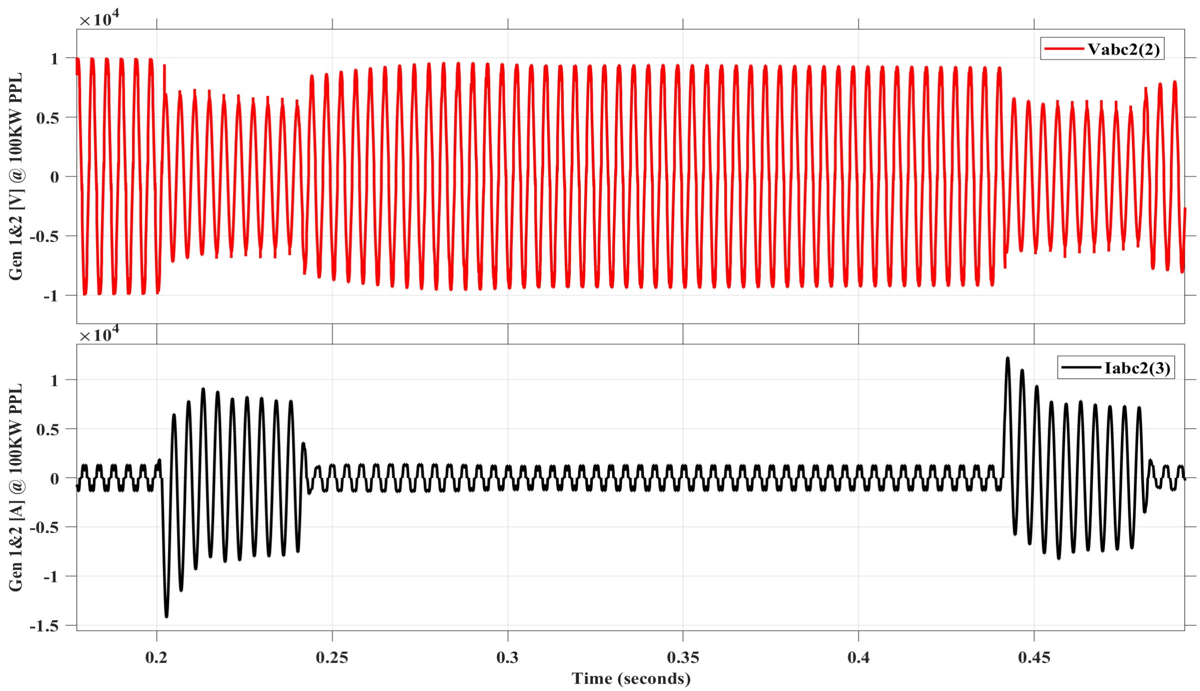

Figure 50: Pulsed-Load Signature on the Grid Generator at 100 Kw

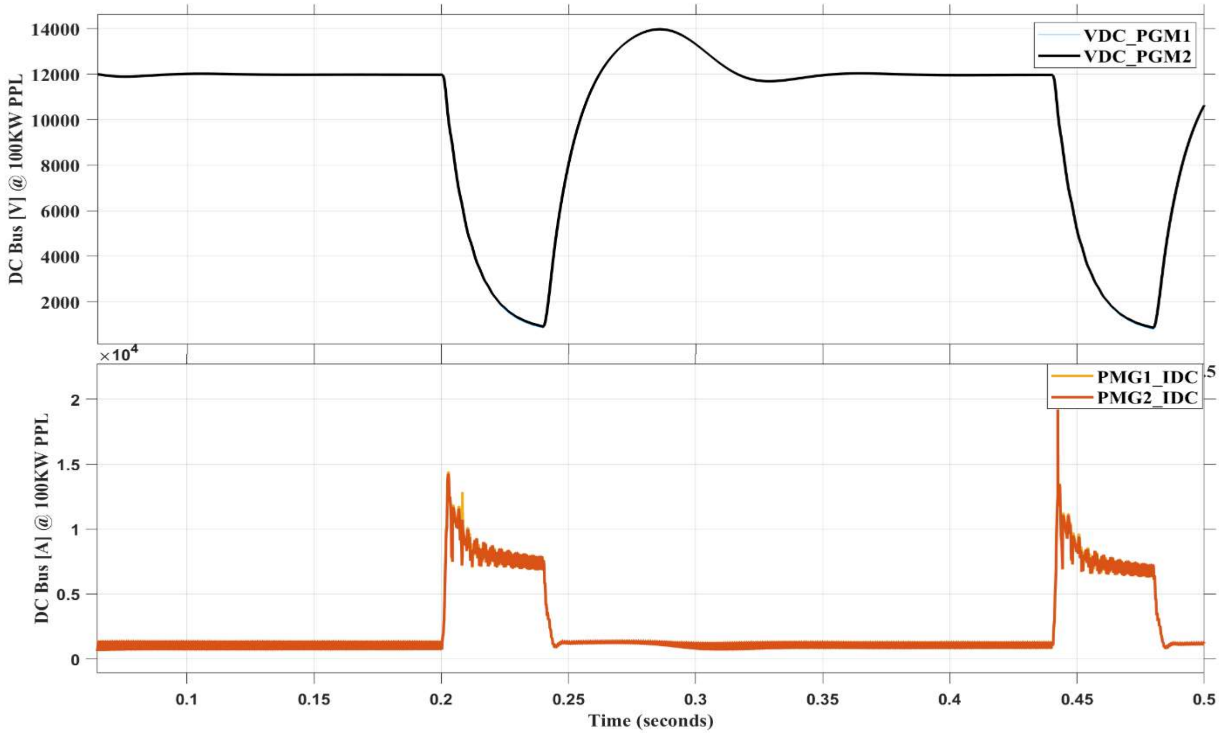

Figure 51: Pulsed-Load Signature on the DC Bus Voltage & Current at 100 kW

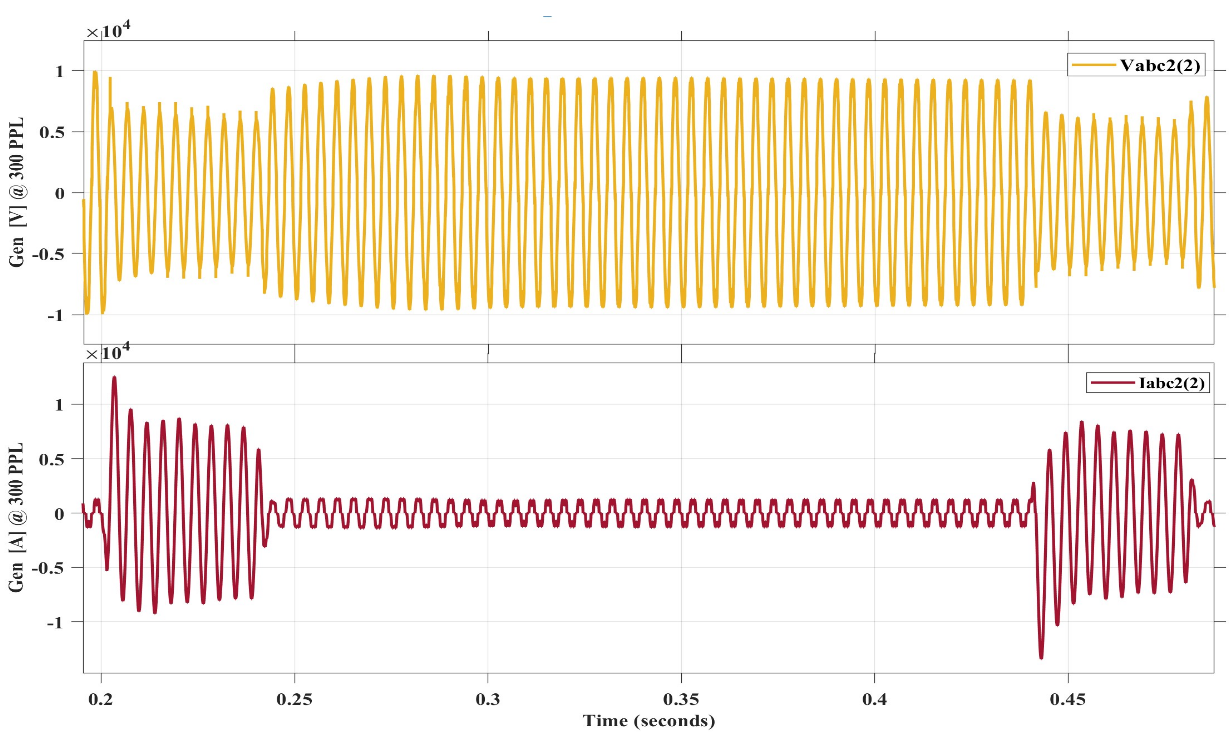

Figure 52: Pulsed-Load Signature on the Grid Generator at 300 KW

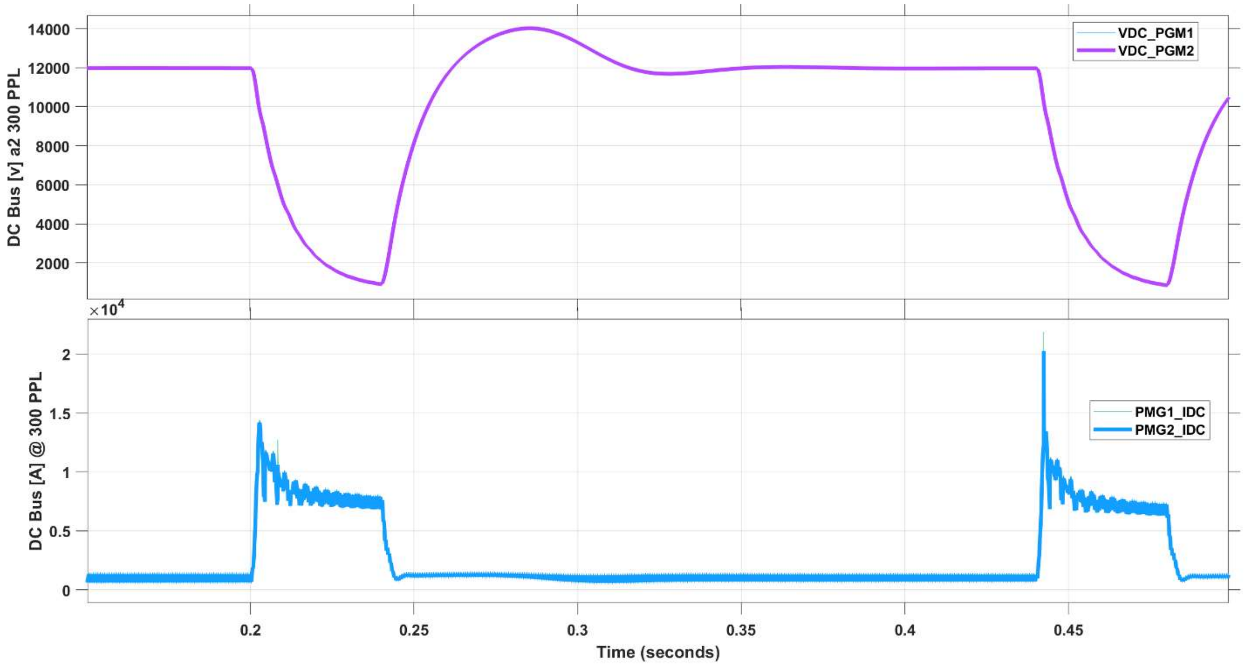

Figure 53: Pulsed-Load Signature on the DC Bus Voltage & Current at 300 Kw

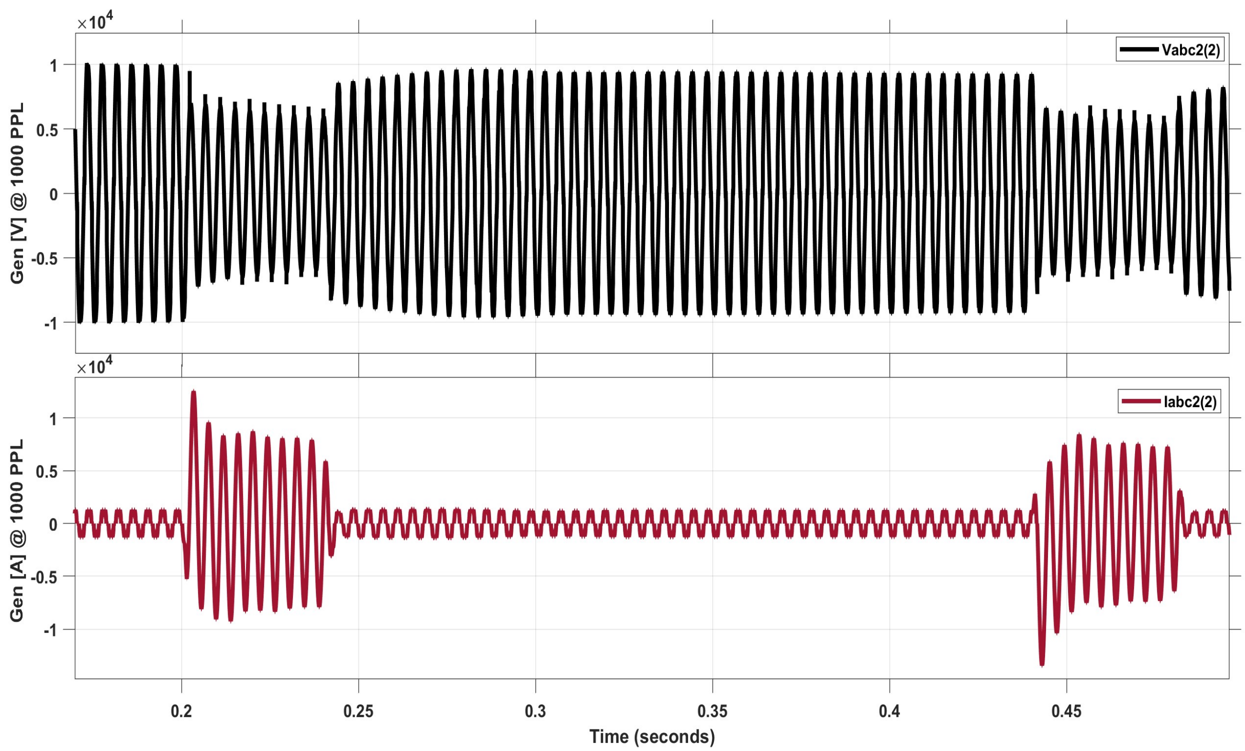

Figure 54: Pulsed-Load Signature on the Grid Generator at 1000 KW

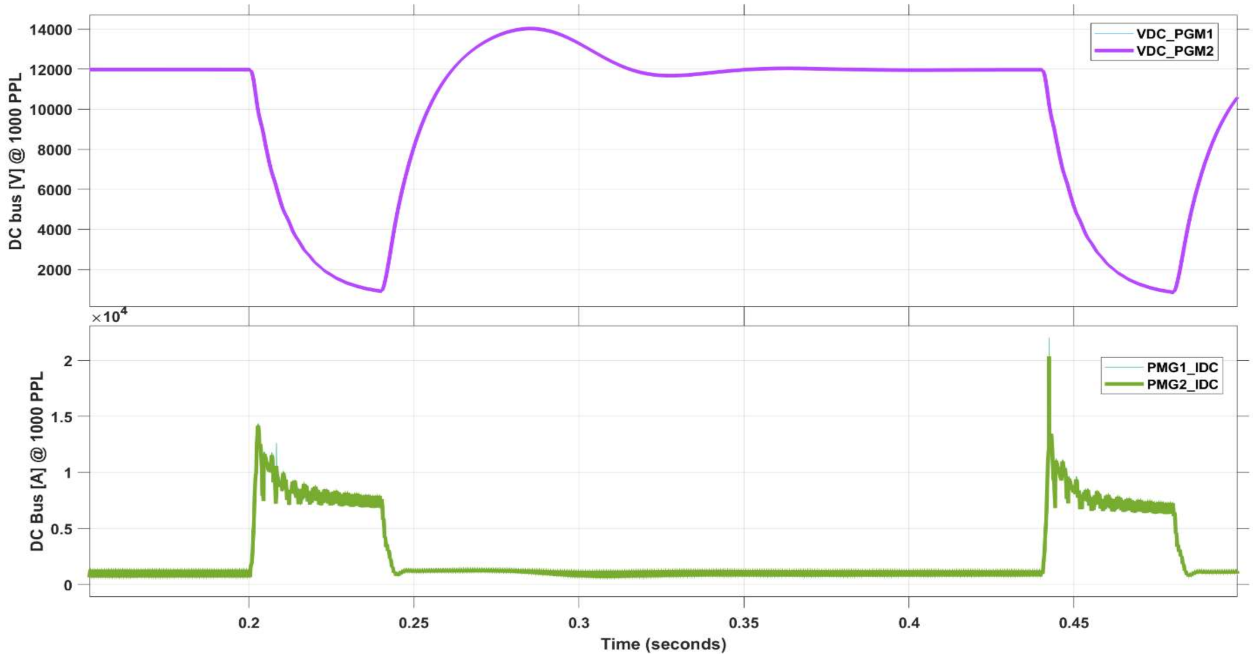

Figure 55: Pulsed-Load Signature on the DC Bus Voltage & Current at 1000 KW

Case 4: Line to Line Fault on The DC Bus

To investigate the impact of both lines to ground fault signature on the DC bus, a second run was performed on the MVDC system. A bus fault was triggered at 2 seconds, therefore shorting both lines to ground. The grid side disturbance was defined by a drop in the AC voltage and a spike in the AC current as shown in Figure 56. DC offset theory is key in explaining the current and voltage fault intercept [78]. Based on the description given in [78], one can conclude that the fault intercept occurs when voltage phase A was at 90°, which is the result of the displayed voltage and current shapes.

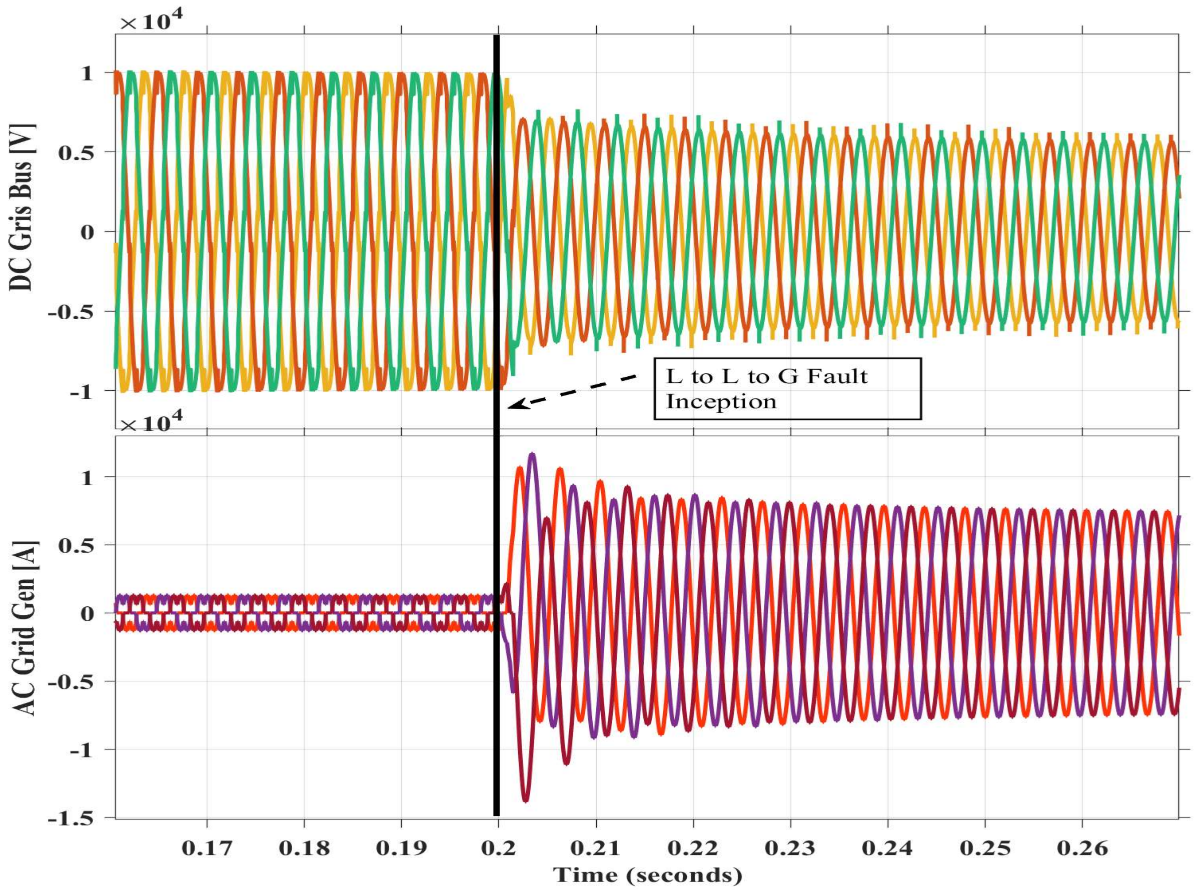

Figure 56: Line-to-Line Signature on the Grid Generator

The DC bus voltage and current system response to the line-to-line fault are displayed in Figure 57. The DC bus voltage is characterized by a voltage drop followed by an exponential decay toward infinity. This fault signature can only be justified by the fact that the rectifier, which was operating originally as a voltage source mode, went into a current-limiting mode. Power converters tend to limit fault current well below the detection threshold of protection relays, which makes it difficult to detect. These are some of the operational properties of power converters, which complicates the fault transient signature and protection system performance. The bus current is defined by a sudden rise, a distortion and then a decay different from the bus voltage decay. The fault signature here is a contribution of two factors: the discharge of the bus capacitor represented by the fast current peak, and the inductors discharge represented by a slow decaying.

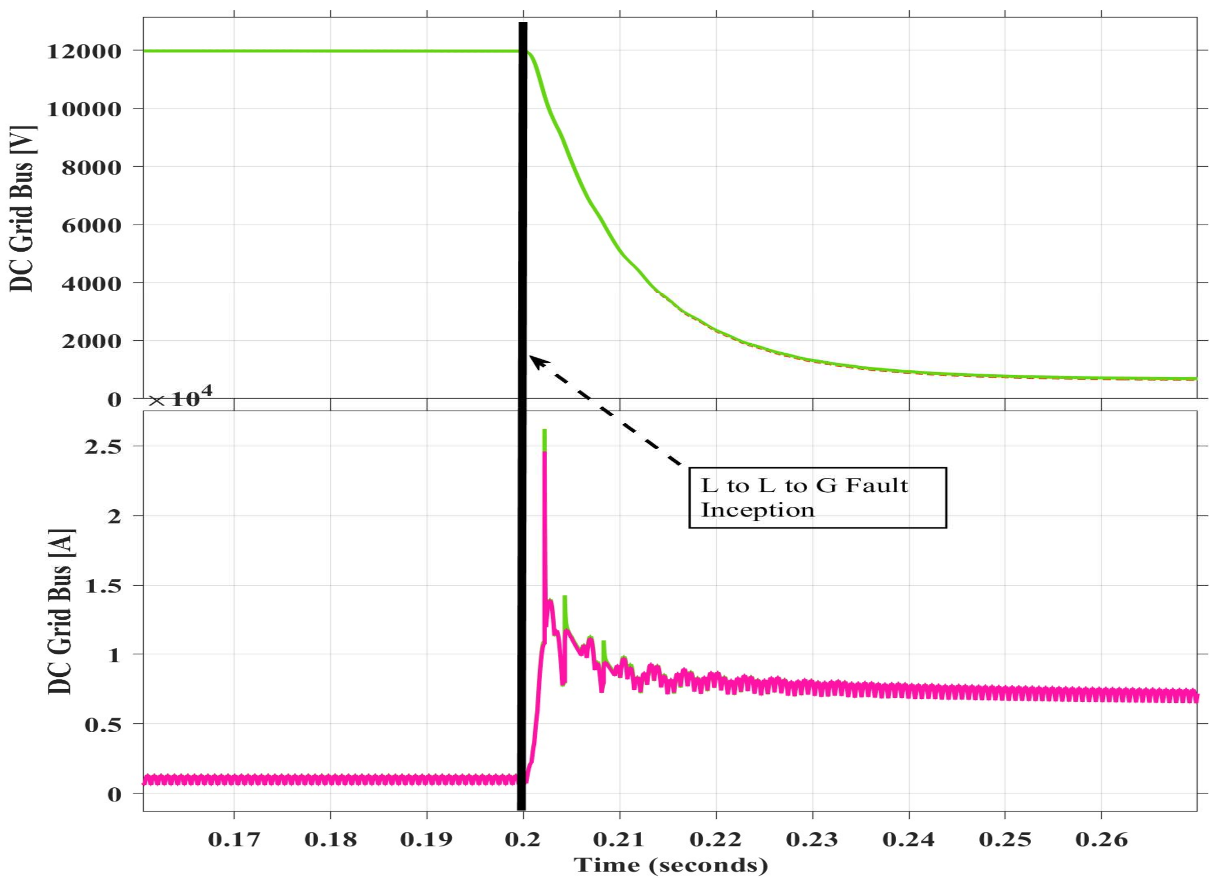

Figure 57: Line-to-Line Signature on the DC Bus Voltage & Current

Case 5: Line-to-Ground Fault on The DC Bus

A simulation was performed with only the negative line to ground faulted to demonstrate the difference between a double line-to-ground fault and a single line-to-ground fault. Interesting system responses were observed (as shown in Figure 58, and Figure 59). On the grid side, the generator phase voltage exhibits distortions and a positive phase shift toward the positive y-axis. During normal MVDC operation conditions, DC lines balance their voltage with respect to ground depending on each line resistance. If the system is symmetrically built, each line to ground will carry half of the total voltage. Consequently, during a line-to-ground fault, the unfaulty line may be subject to full bus voltage. The corresponding phase current is defined by an increase on the current magnitude and a distortion on the upper part of the current waveform. The AC current waveform is also noted to be non-sinusoidal and highly asymmetrical. Converters do not decouple the AC grid from the DC grid, and in some cases due to the absence of transformers current may damp back through generator's neutral point resistor, which may cause a distortion (shown in the AC current waveform in Figure 56). A second simulation run was carried out with the positive line to ground faulted. The system response obtained on the voltage was the opposite of what was described above with the negative line-to-ground fault. A distorted voltage with a voltage phase shift toward the negative y-axis were noted. However, the three-phase current waveforms distortion remained the same. On the DC bus, for both simulations, a very low voltage drop is noted because line to ground fault on DC bus voltage are of low impact. However, the DC current waveform disturbance, which very much looks like a three-phase half-wave converter current signature could be a result of current being forced to go through only half of the converter bridge.

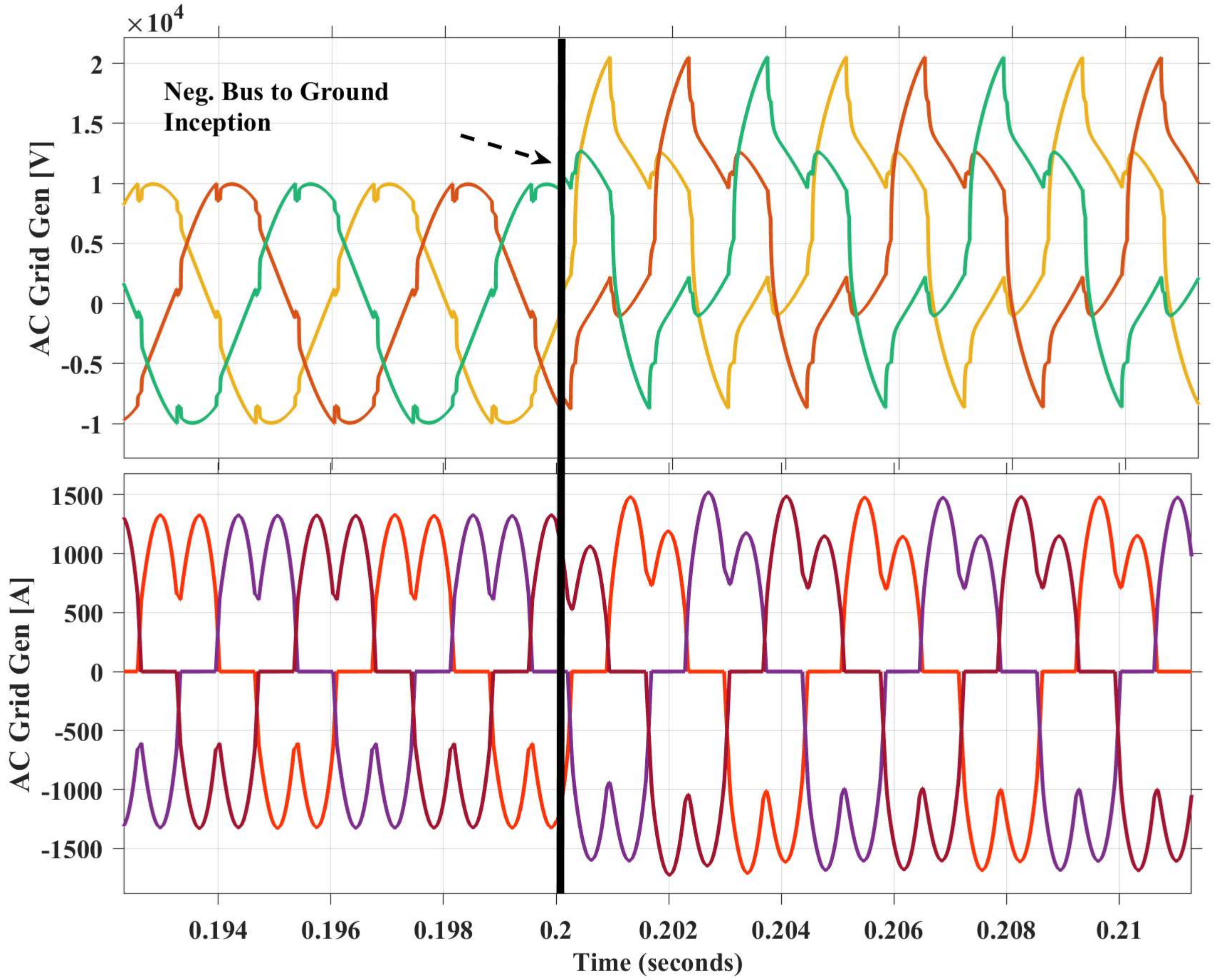

Figure 58: Line-to-Ground Signature on the Grid Generator Voltage & Current

On the DC bus, in both simulations, a very low voltage and a distortion on the DC current waveform is observed below.

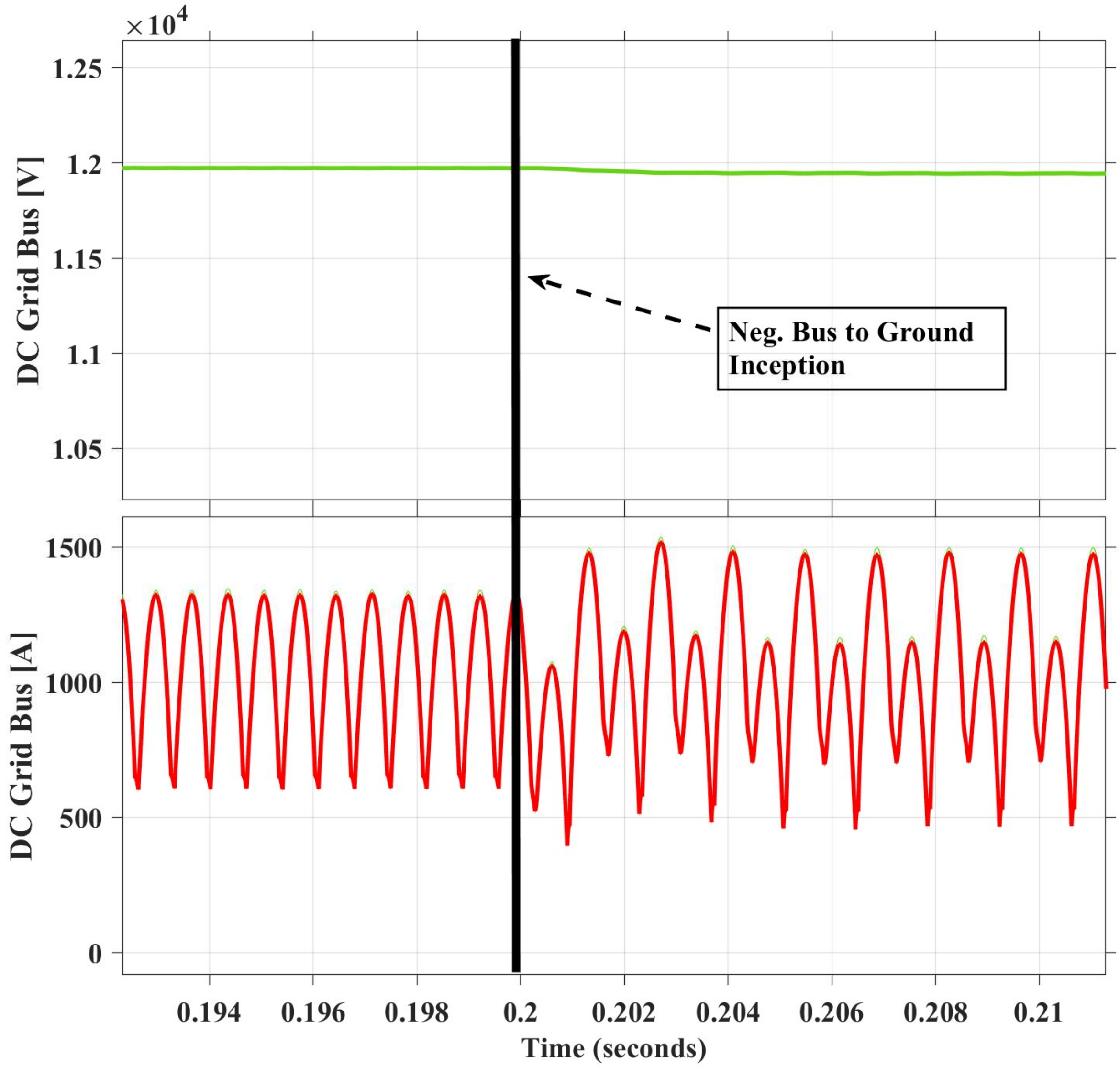

Figure 59: Line-to-Ground Signature on the DC Bus Voltage & Current

Case 6: Line-to-Line Fault Combined with a Pulsed-Power Load on The DC Bus

In this simulation, the line-to-line fault and the pulsed-power load were initiated at 0.2 seconds to investigate and comprehend their interactive impact on the MVDC system. The system response that was observed was the same as described in the line-to-line fault for both the grid and DC bus side (as shown in Figure 60 and Figure 61). The conclusion drawn here is that no matter the amount of the pulsed load if a line-to-line fault occurs, the system response will mimic the fault behavior.

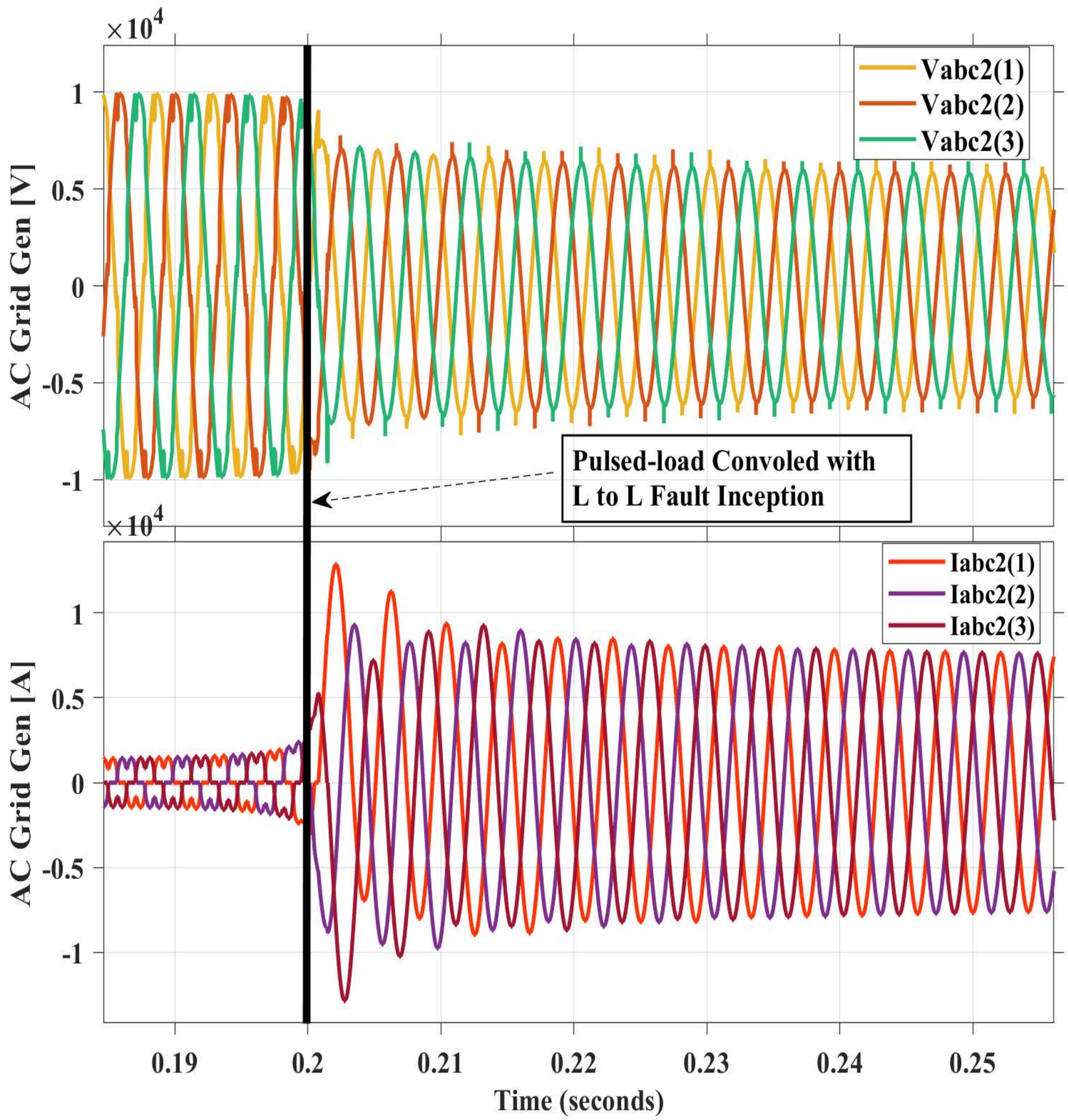

Figure 60: Line-to-Line and Pulsed-Load Signature on the DC Bus Voltage & Current

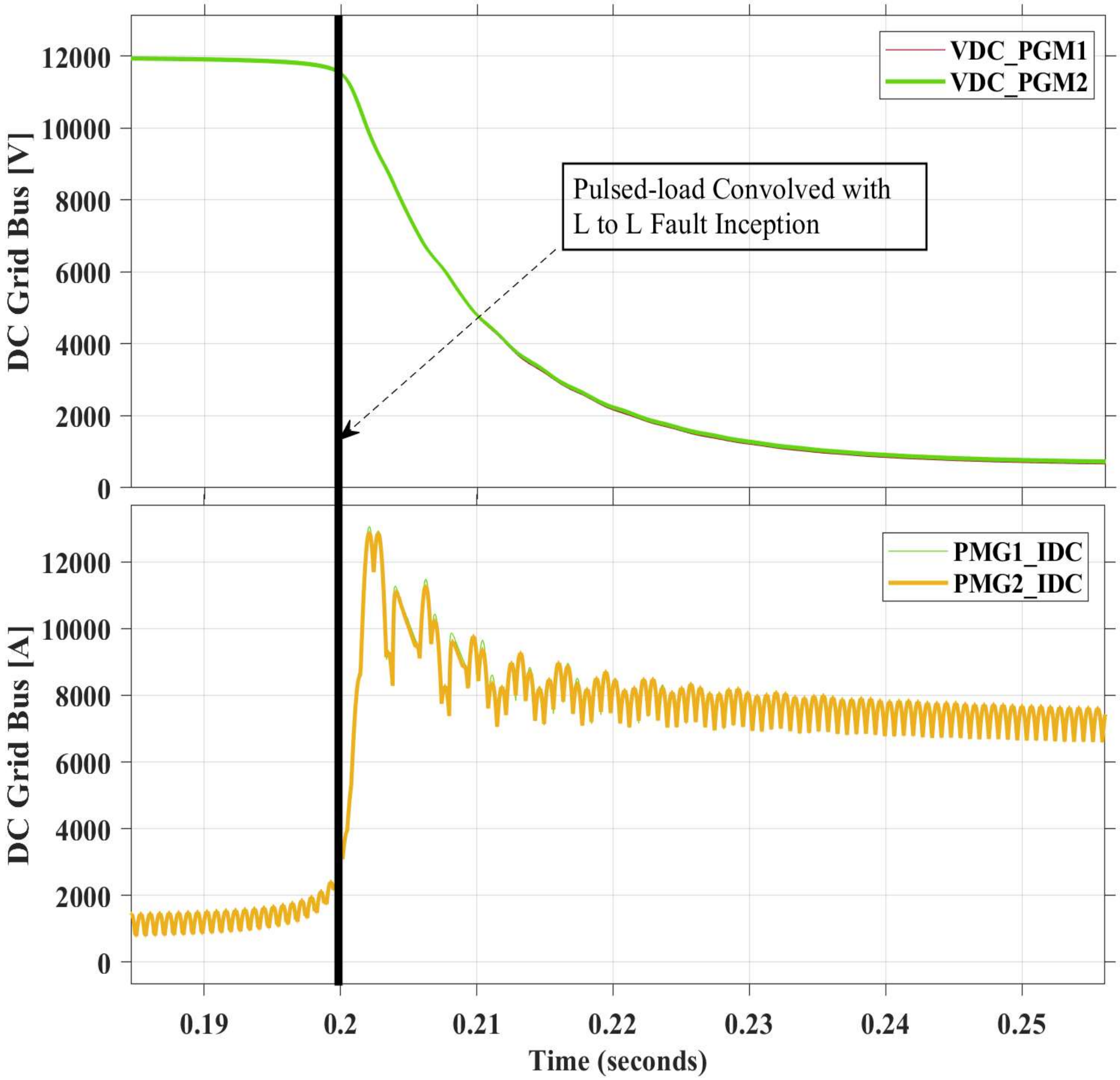

Figure 61: Line-to-Line and Pulsed-Load Signature on the DC Bus Voltage & Current

4.3 ARC FAULT ASSESSMENTS

A fault in the MVDC systems can be triggered by a minor conductor (steel screw, copper wire) across the bus and the ground. It can also be a result of a small animal bridging the conductors or even a condensation of water over an insulator. The resultant effect can quickly grow into a long-lasting arc due to the absence of the natural zero-crossing in DC grid.

In this section, the calculation of the arc fault is conducted in one of the MVDC system modular branch, following the IEEE Standard 1564-2002 [79]. It is vital to understand that the IEEE 1584 equations are valid solely for certain conditions. These conditions for the test data are tabulated in Table 9.

Parameter	**Set point**
System Voltage (KV)	12000 KV
Grid Frequency (Hz)	60 HZ
Bolted Fault Current (KA)	24.1 KA
Gap Between the Electrodes (mm)	1 to 200 mm
Equipment Enclosure Type	Closed air
System Grounding Type	High resistance Grounded
Type of Fault	Line to Line

Table 9: MVDC Applicable Set Point for Use of the IEEE 1584 Calculation Method

4.3.1 Characteristics of Arc Fault Using the Shipboard MVDC System

An arc consists of three regions—node, cathode, and plasma region—as shown in Figure 62.

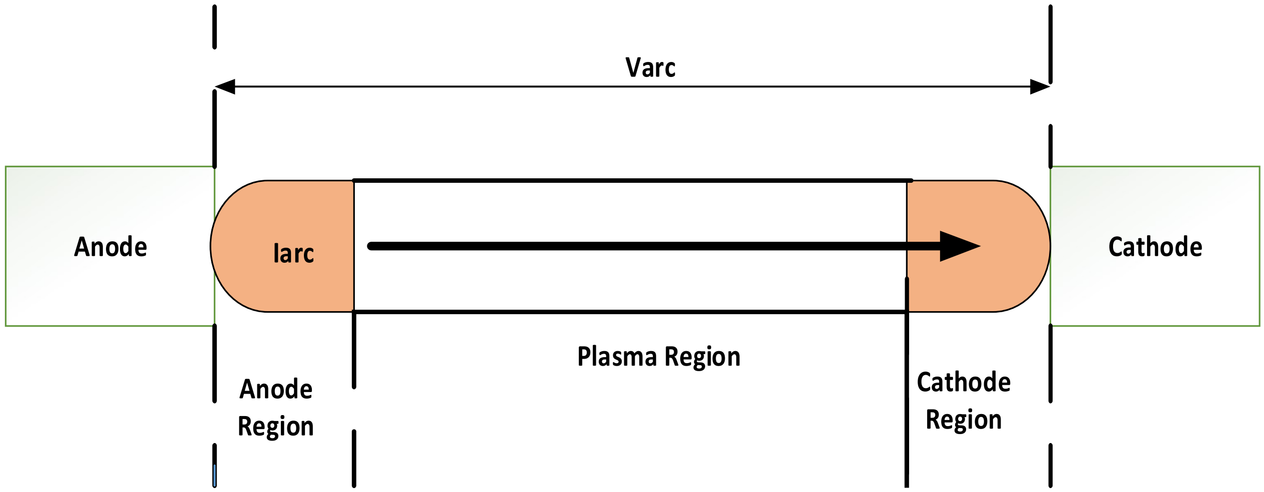

Figure 62: Arc Fault Regions Representation

The voltage slope across the arc plasma depends on the actual length of the arc. The arc can sometimes deviate from the gap width between the electrodes (as shown in Figure 63).

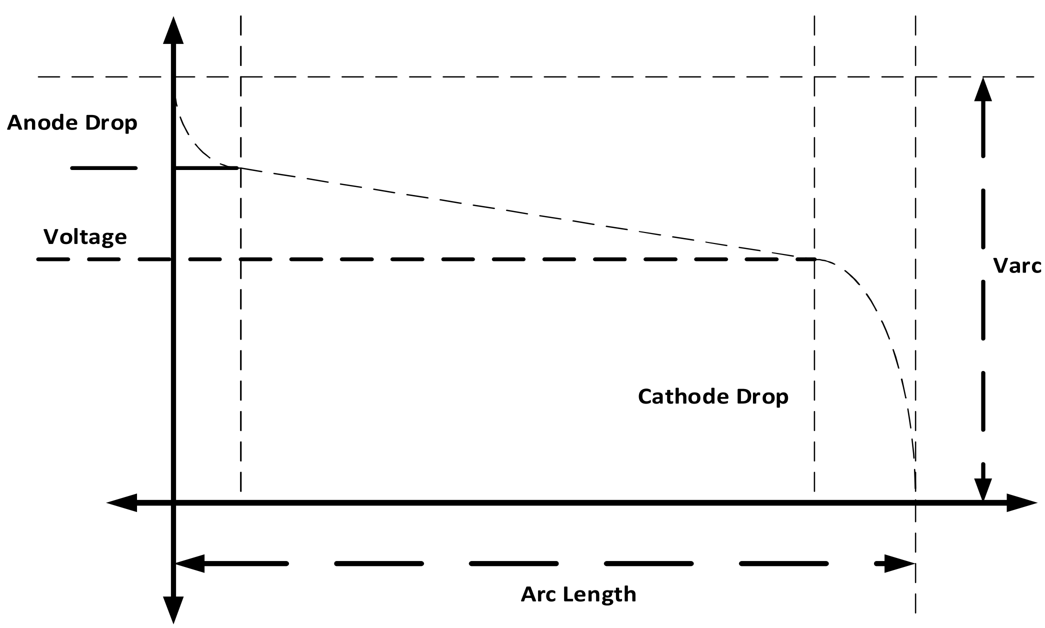

Figure 63: Arc Fault Voltage Slope Deviation

Note that the deviation length is directly proportional to the gap widths. It is also worth mentioning that the voltage slope in the plasma region is nearly independent from the arc current— for current magnitude above 50A for open air arc [80].

4.3.1.1 Maximum Power Method ARC Assessment on The Shipboard MVDC System

The two-zone MVDC system bus anode and cathode were connected across a Simscape fault block. The standard working distance D = 18" or 45.72 cm and the T_{arc} = 2s were chosen to compute the incident energy. The arc fault across the line were triggered by a change in the instantaneous resistance.

$$V_{arc} = 0.5V_{dc} \quad = 0.5 * 12000 = 6000\,V, \tag{4.1}$$

The arc current is estimated to be

$$I_{arc} = 0.5I_{bf} = 0.5 * 2.41 * 10^4 = 12050\,A, \tag{4.2}$$

The incident energy

$$IE = 3 * 0.02 * V_{arc} * I_{arc} * \frac{T_{arc}}{D^2} = 4{,}150.6\frac{cal}{cm^2}\,, \tag{4.3}$$

4.3.1.2 Arc Resistance Method ARC Assessment on The Shipboard MVDC System

Using Equations (2.7) and Equation (2.8) and the empirical arc formulas for arc current$100A < I_{arc} < 100\,KA$ [81], the shipboard MVDC arc fault voltage and resistance are tabulated in Table 10 for different electrode gap value.

Electrode Gap (mm)	Arc Voltage (V)	Arc Resistance (Ω)
1	32.823	0.003
5	102.619	0.009
10	77.161	0.006
20	119.895	0.010
50	175.495	0.015
100	329.071	0.034
200	628.947	0.052

Table 10: MVDC Arc Voltage and Resistance Computation Using the Resistance Method

4.3.2 Arc Voltage and Resistance VS Electrode

In this section, the studied shipboard MVDC system fault analysis arc fault voltage and resistance tabulated in Table 10 above were plotted against the electrode gap. The calculation incorporates the Resistance Method that can feed an electric arc flash without blowing a fuse. This is to anticipate potential hazards from DC arc flashes transient behaviors on future shipboard MVDC systems. From the below Figure 64 (a) and (b), it can be concluded that there is a direct relationship between the electrode gap and the arc flash voltage and resistance. Therefore, as the gap between the anode and cathode increases or decreases the corresponding arc flash voltage or arc resistance increases or decreases. This highlighted the practicable consideration that can be taken in designing some of the future circuit breakers, disconnect switches or even relays for shipboard MVDC systems.

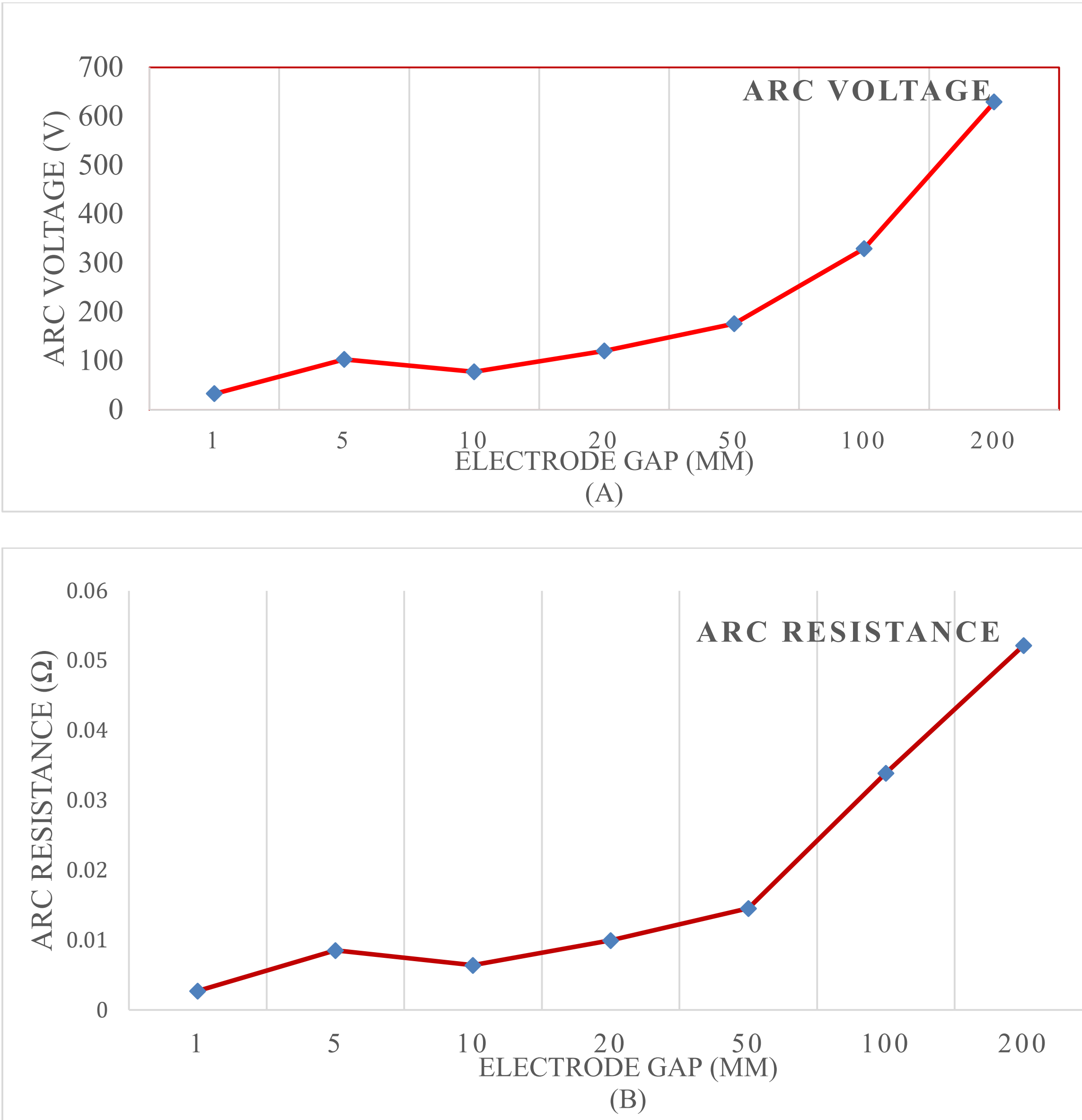

Figure 64: Electrode Gap Impact on the Arc Voltage or Arc Resistance

4.3.3 Arc Resistance VS Arc Current

The arc resistance versus the arc current of the shipboard MVDC system test results is plotted here to examine how the arc current is impacted as the arc resistance is increased or decreased. Figure 65 shows that they are inversely proportional—as the resistance is decreased, the arc current is increased.

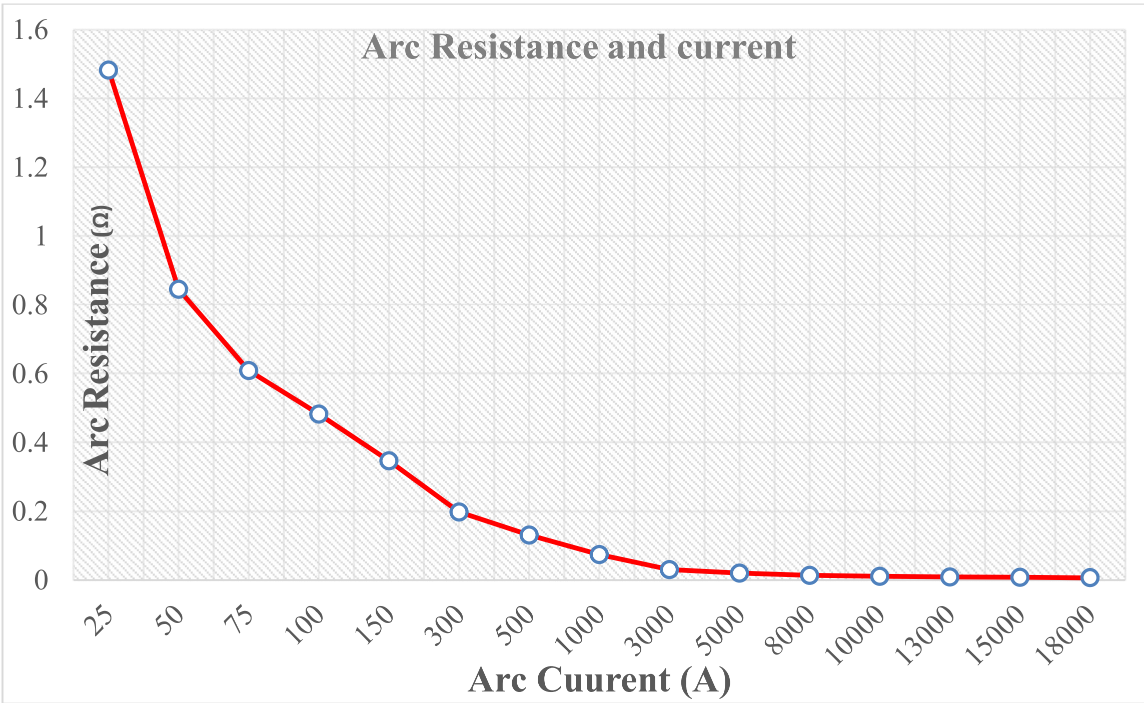

Figure 65: Arc Resistance Impact on the Arc Current

In addition, the above figures clearly highlighted another important fact about personal and equipment safety. Equipment should be designed for safe testing and maintenance. Test points should be included and easy to access so that voltage and current testing can be accomplished while reducing exposure to arc flash hazards. Switchboards, load centers, transformers and distribution panels should be designed with arc flash-proof shielding. High rated breakers should be arc vacuum-proof. Finally, personnel should be well equipped with arc-proof Personal Protecting Equipment (PPE), arc-proof clothing. They also should participate in some recurring arc flash awareness classes.

4.4 CONCLUSION

In this Chapter, the proposed shipboard MVDC system was modeled and simulated in the MATLAB Simscape package. Through the MVDC system, a variety of generator and DC bus fault dynamics and pulsed-power load were addressed and partially analyzed through different case scenarios. The intent is to gain a better understanding of potential issues that future smart DC-based micro grids may present. Note that MVDC systems are still under development even though the literature presented in Chapter 2 has shown significant advantages of using MVDC over MVAC. In the next chapter, a fault detection and isolation technique will be developed for the shipboard MVDC studied above. This fault detection and isolation technique will be derived based on the simulation responses conducted in this chapter.

CHAPTER 5

FAULT PROTECTIONSYSTEM FOR THE SHIPBOARD MVDC SYSTEM

5.1 BACKGROUND

In this chapter, based on the proposed shipboard MVDC short-circuit fault(s) and disturbances and PPL transient system responses, a communication-based fault detection and isolation system controller that extends upon AC directional overcurrent relay protection system principles is developed and proposed. The controller is designed to discriminate between system dynamic short-circuit fault(s) and bus current transient disturbances due to a PPL. To validate the effectiveness of the proposed protection controller, different bus current disturbances are studied using the PPL system at different ramp rates, pulse widths, power levels, and locations.

5.2 PROPOSED PROTECTION SYSTEM

Shipboard power system is isolated and distributed over a short distance depending on the distribution techniques: radial, ring or zonal distribution system. Therefore, it is vital to have a secure and reliable power flow during operation—especially at sea. For instance, current trends [49], [55], [82], [83] highlight significant research interest in MVDC distribution systems. One of the important aspects of MVDC shipboard power system design is developing a secure, robust, and reliable protection system [44]. As stated in [84], protection problems in MVDC distribution systems involve fault detection, localization, and isolation. The literature has revealed five different types of fault protection techniques applicable to MVDC distribution systems. These techniques along with their differences are summarized in Chapter 2, Table 1.

As a result, a communication-based fault detection, localization and isolation system controller that mimics a directional overcurrent relay protection system is developed and proposed. The controller is designed to segregate between system dynamic short-circuit fault and bus current disturbance due to a PPL. To validate the effectiveness of the proposed protection controller, different bus current disturbances are triggered using the PPL system at different ramp time rates, pulse widths, power levels, and locations.

5.2.1 Background on Overcurrent Protection Relaying

Overcurrent Relay (OCR) is traditionally defined based on an electromechanical relaying protective device, which operates only when the current value in a given circuitry exceeds a predetermined set value, also known as the pickup, for a given amount of time. As displayed in Figure 66, OCR takes a single instantaneous input in the form of AC current. It has a normally open-contact output port which changes states to shut whenever the relay trips. The time settings shown on the figure decides the operation duration of the OCR while the plug setting decides the current required for the OCR to pick up [84].

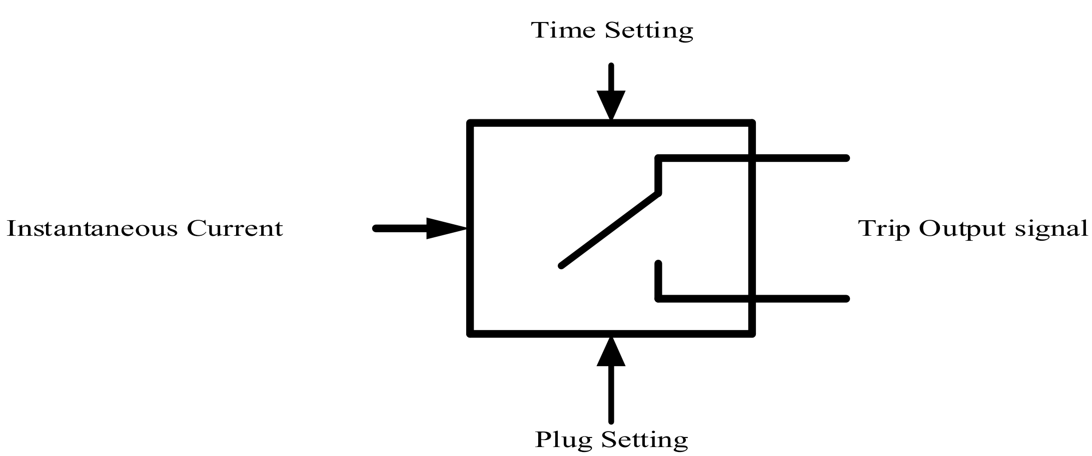

Figure 66: Overcurrent Relay Diagram

The time taken by an OCR to trip a breaker for a range of over current conditions is define the Time-Current Characteristic Curve (TCCC) as shown in Figure 67.

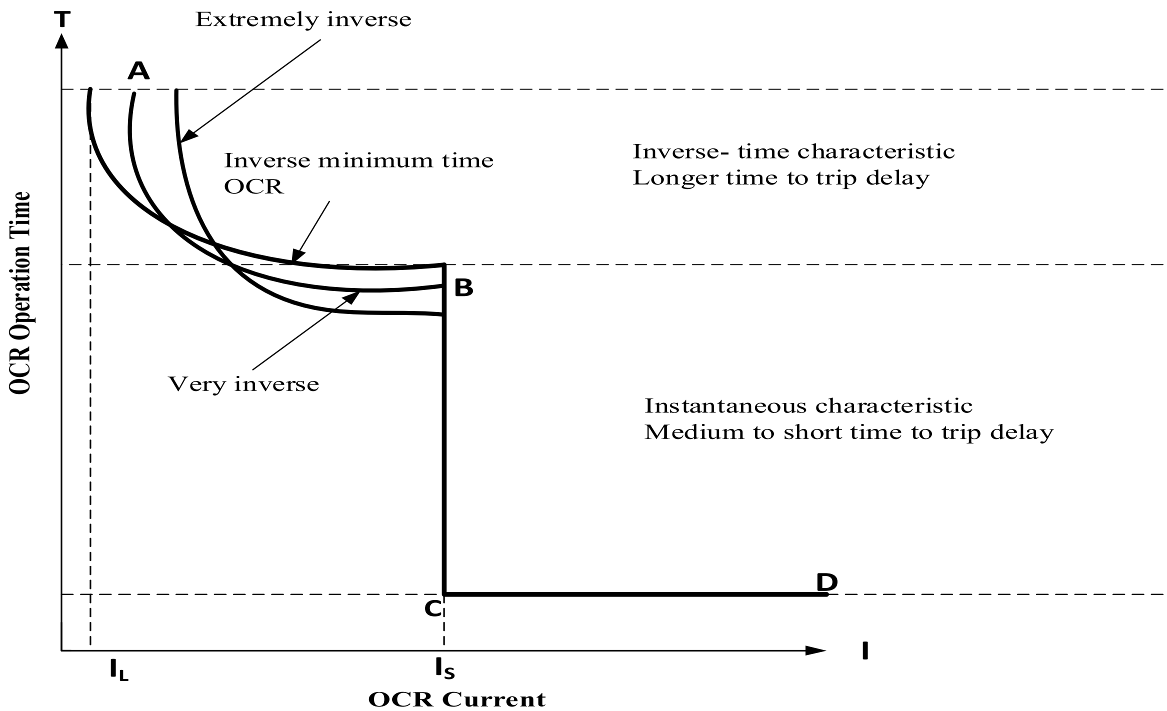

Figure 67: Time-Current Characteristic Curve for OCR

The x-axis of the TCCC describes the fault current flow level and the y-axis describes the time taken by the relay before initiating a trip action. The A-D slope represents the OCR inverse characteristic and tends to a definite minimum operating time as the current becomes severe. The requirement of operating in this segment is that the more severe the short-circuit gets, the faster it should be extinguished. The reason behind that is if the overcurrent is permitted to sustain for a longer period it may cause grave damage to the apparatus. The B-C segment represents the OCR instantaneous characteristic, also known as the high-set. The time delay taken by the relay in sending the trip signal when operating in this segment should be shorter than the previous segment.

The C-D slope represents the OCR-definite, minimum-time characteristic. Normally, no intentional time delay should be taken when operating in this segment. However, it may be necessary if the relay is to coordinate with downstream protection elements (such as fuses). The generic equation of the OCR inverse-time characteristics is given as [72], [85], [86]:

$$T_{op} = \frac{TMS * \beta}{\left(\left(\frac{I_L}{I_S}\right)^{\alpha} - 1\right)}, \tag{5.1}$$

where TMS (time multiplier setting) and β are two constants used to determine the function of the relay, α is the constant that determines the inverse characteristic. I_L is the load current or the instantaneous DC current, and I_S the setting or pickup current. The coefficients of Equation (5.1) determine different standard characteristics (such as the normal inverse, very inverse and extremely inverse characteristics defined by the IEEE, American National Standards Institute (ANS)I, IEC and other standards).

Conventional AC protection relay uses fundamental frequency phasor Root Mean Square (RMS) values of two AC quantities to detect the existence of a fault. These quantities are in most cases the protecting zone bus voltage and current. During the process, all the harmonics are typically filtered out in digital relays which lead to the loss of some useful information. For instance, under an arc fault scenario, the value of the resistive component of the faulty bus impedance will increase to change the impedance angle. Since the protected bus is made up of inductance (X) and resistance (R), its fault angle depends on the relative values of the operating frequency, X and R. Consequently, under resistive conditions, a protective relay with a characteristic angle equivalent to the bus angle will underreach.

5.2.2 Proposed Protection Controller Algorithm

The proposed MVDC protection controller was designed based on the dynamic performances conducted in Chapter 4, Section 4.3. In Section 4.3, it was demonstrated that the DC-link current signatures under PPL disturbance and the DC short-circuit fault are quite similar as shown in Figures 50 & 52. This problematic issue has been highlighted [87] as stated previously, where there is difficulty in distinguishing the coexistence of a short-circuit fault and a PPL disturbance in the design of an MVDC protection system can result in an unnecessary breaker trip or overlooking a genuine fault. Consequently, the overall shipboard MVDC system becomes unreliable. For these reasons, a suitable protection system should be sensitive to dynamic interaction during transients and to distorted fault waveforms as summarized in Table 2. In this work, under the protection system domain, a technique that detects and distinguishes these issues has been developed and tested.

5.2.3 Proposed Controller Fault and Disturbance Segregation Technique

During operation of the system under test, the current flow in each power system cable section is supervised by a local communication-based protection controller. When the load current I_L is greater than or equal to the set current I_S ($I_L \geq I_S$), the section cable breaker is flagged, and the disturbance identification process is initiated. The $\left(\frac{I_L}{I_S}\right)^{\alpha}$ relation from Equation (5.1) determines the operational time of the proposed protection controller. In the design of the protection controller, I_S is a pre-set value, and I_L varies. I_L varies due to system disturbance from either a short-circuit fault(s) and/or an increase in the system loading. In Chapter 2, Figure 52, it can be seen that the disturbance caused by a short-circuit fault on the DC grid bus current has a peak current that is almost double the PPL current disturbance peak shown in Figure 57. Thus, to distinguish between the two disturbances, during operation, $\left(\frac{I_L}{I_S}\right)^\alpha$ component is integrated and then compared to $TMS * \beta$. As long as $\left(\frac{I_L}{I_S}\right)^\alpha$ integration remains under $TMS * \beta$, no action will be taken by the controller. This logic is backed up by a directional algorithm, which delays the trip signal until it verifies that the DC grid bus voltage falls below some set threshold as displayed in Figure 50.

Once the DC grid bus voltage drops below the set threshold, the trip signal is released, and the corresponding breaker(s) is tripped which isolate the section cable(s). The isolated section(s) remains isolated from the rest of the distribution system as long as the fault remains. A feedback reset algorithm is set to constantly monitor the tripping logic. Whenever one or both tripping logic changes state, the reset algorithm resets the process. A close signal is then automatically sent to the corresponding breaker(s) and the isolated section(s) is brought back online. The overall protection system controller flowchart is given in Figure 68 below.

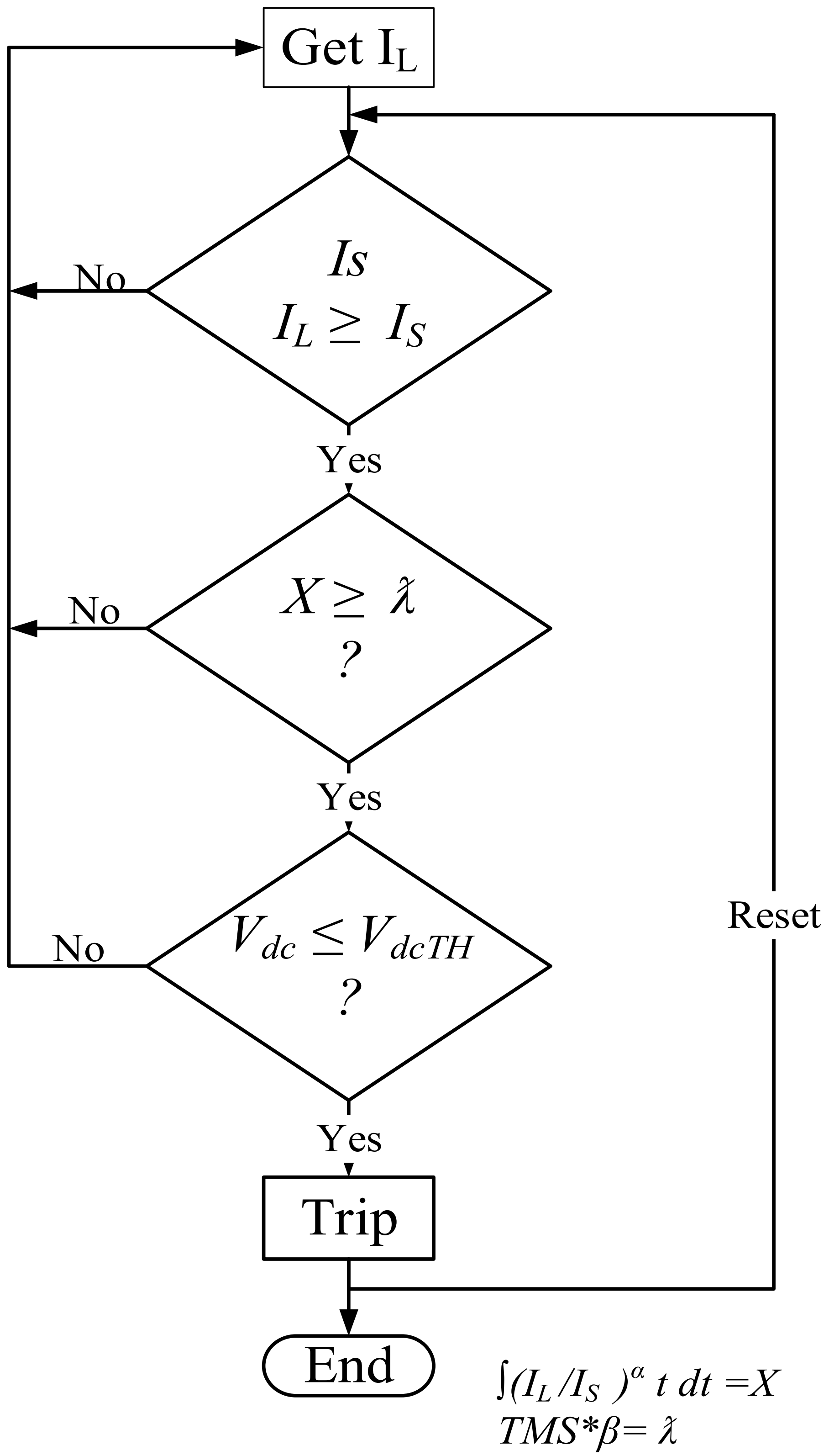

Figure 68: Proposed Protection Controller Flowchart

5.2.4 Proposed Controller Performance and Test Validation

The proposed controller performance and validation are studied here for different disturbance conditions on the shipboard MVDC system presented in Figure 45. The parameters discussed above are used during the simulation run as follow Table 11:

α	β	TMS	I_s
0.14	0.02	8572	450 A

Table 11: Proposed Controller Coefficient Set Points

Case 1: The system was first run for 0.5s to reach steady state, after which a line-to-line-to-ground short-circuit fault was triggered at 0.2s on Z1CS21 section cable (Figure 45). As displayed in Figure 69(a), the fault protection controller was able to detect and isolate the faulty section within 50ms. Furthermore, the DC grid bus voltage was also recovered within the same time frame. In the second situation, an additional fault was also triggered on Z2CS14 0.03s after triggering the fault on the Z1CS21 section. The protection controllers on both sections were able to detect and isolate their corresponding section. Since the second short-circuit fault was triggered before the clearance of the first fault, an additional 45ms-tripping delay was noted on the second controller Figure 69(b). As a result, it took the DC grid bus voltage a longer time to recover when compared to the first iteration.

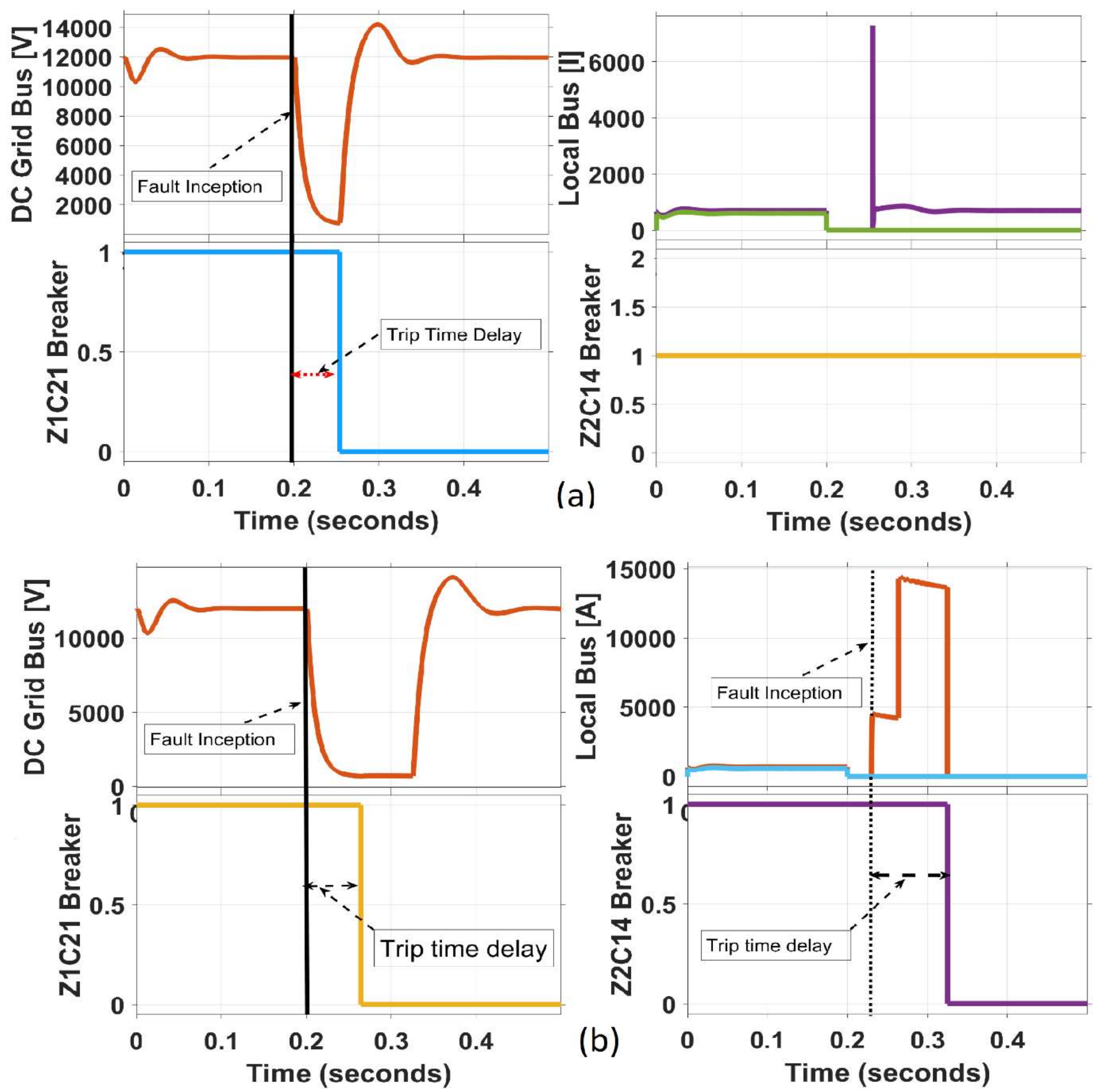

Figure 69: Proposed Protection Controller Short-circuit Response
(a) Fault on Z1C21 Section
(b) Fault on Both Z1C21 and Z2C14

Case 2: To validate the ability of the proposed protection controller to distinguish between short-circuit fault(s) and system bus disturbance, the following scenarios have been simulated:

- A 100 kW PPL is applied to the shipboard MVDC system at Z1CS21 section. DC grid bus voltage and current waveform disturbances have been captured and displayed in Figure 70(a). No trip response was initiated by either controller.
- In the second simulation, the power level was increased from 100 kW to 500 kW and the pulsed duration from 1ms to 4ms. The DC bus voltage and current waveforms as shown in Figure 70(b) exhibit a severe disturbance. The disturbances are quite like the double line-to-ground, short-circuit response captured in Chapter 2, Figure 52. However, the disturbances did not cause the proposed protection controllers to send a tripping command (and thus the system is secure from a false trip).
- In this final iteration, both the 100 kW and 500 kW PPL system were triggered on the shipboard MVDC system. The DC bus voltage and current waveforms—as shown in Figure 70(c)—exhibit a more severe disturbance than the second iterations. However, the proposed protection system was able to discriminate between the PPL disturbance from a short-circuit. As a result, no tripping command was sent by the protection controllers.

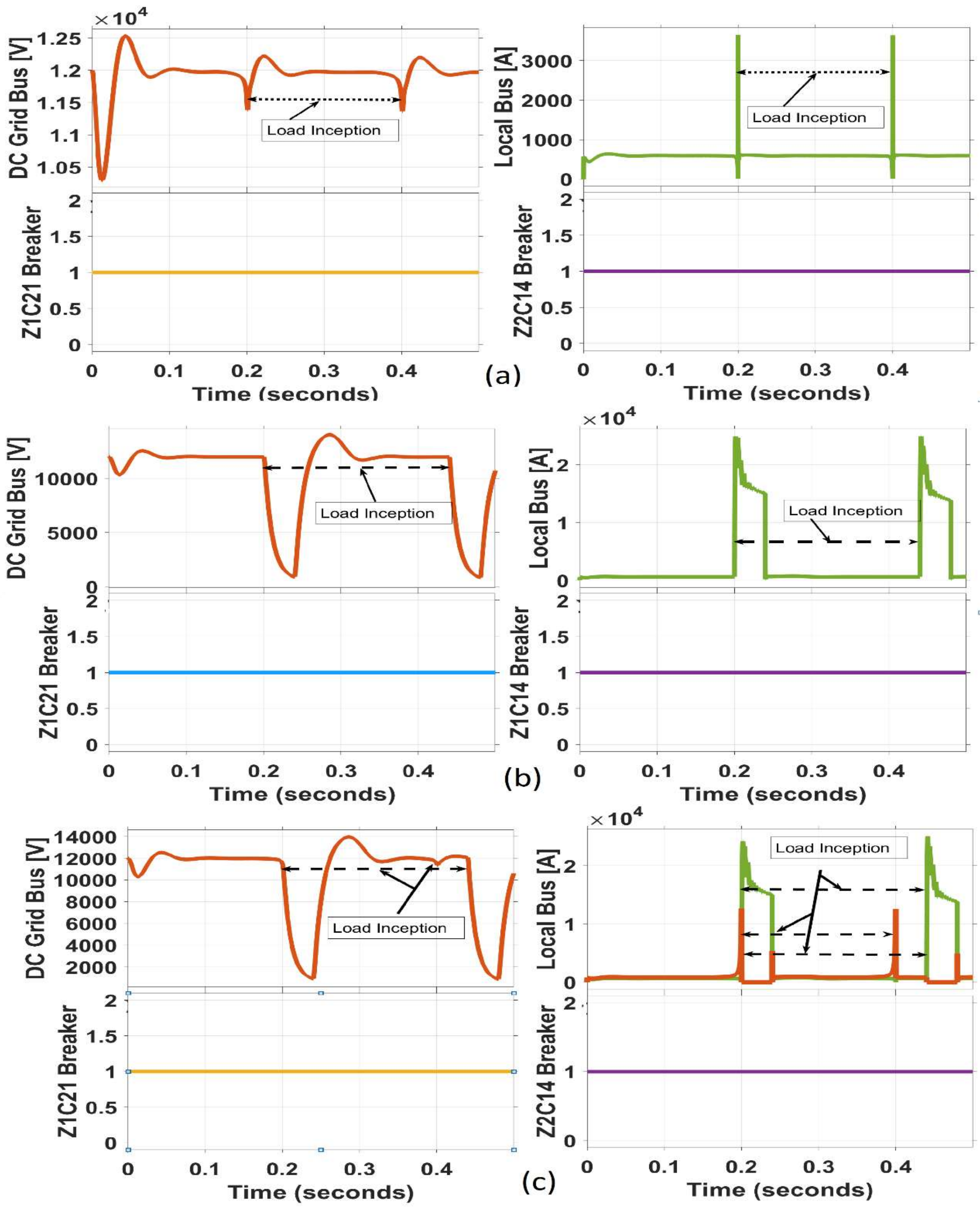

Figure 70: DC Grid Disturbances Under PPL Loads
(a) 100 kW PPL Disturbance with 1ms Pulse Width
(b) 500 KW PPL Disturbance with 4ms Pulse Width
(C) 100 kW and 500 kW PPL Disturbances at 1ms and 4ms

5.3 CONCLUSION

- A comprehensive investigation and analysis were undertaken on various types of shipboard MVDC system dynamic faults and disturbance behaviors. MVDC short-circuit faults—such as positive or negative bus to ground, both positive and negative buses to ground, and pulsed-power load(s) disturbances—were the fault modes investigated along with PPL dynamics.

The main conclusions of this study are as follows:

- Based on the system responses, a novel communications-based fault protection control algorithm was designed. The proposed protection controller was designed as a solution to distinguish between system dynamic faults and transient bus disturbances such as PPL.
- The effectiveness of the novel protecting scheme to respond to short-circuit fault(s) is validated in two steps. Short-circuit faults were triggered at Z1CS21 cable section and at Z1CS21 and Z2CS14 cable sections respectively. The proposed protection system has correctly responded by detecting, localizing, and isolating the faulty section(s) in both scenarios.
- The protection scheme ability to discriminate between a short-circuit fault(s) and a PPL is also validated using PPL disturbances at different ramp-time rates, pulse widths and power levels. Even though the shipboard MVDC system has experienced severe disturbances under these circumstances, the protection-system, trip-command response remained unaffected.

The work offers a new approach to protecting future MVDC shipboard systems, which are being heralded as the next generation of power systems for naval vessels. The results shown are encouraging in that the proposed protection system can function reliably under highly dynamic mission load profiles, offering better discrimination between future pulsed-power loads and genuine faults.

CHAPTER 6

CONCLUSIONS AND FUTURE WORK

6.1 CONCLUSIONS

The challenges associated with two key components of integrated shipboard power generation and distribution systems are addressed in this dissertation. As discussed above modern flywheel energy storage and medium voltage DC power distribution systems input energy by emanating from a rectification of an AC voltage into a DC voltage. For the FESS, one of the breaking points between the systems occurs when the DC link voltage is controlled by the machine side converter, which then feeds inverted energy to the machine flywheel assembly. As for the MVDC, the DC voltage can either be controlled or uncontrolled by the grid side converter. In this work, a thyristor is used to rectify and control the grid energy to a 12 kV DC voltage. Regardless of whether the controlled or uncontrolled method is used, the DC voltage of the MVDC system is rectified and fed to a common DC bus, which serves as a platform for many DC voltage processes. Both in-depth investigation and attention have been given to this DC-link in this dissertation in order to improve upon the available techniques.

For the FESS, unlike relying on the traditional system automation as the only path of discharging energy back to a grid through the DC-link, a mechanical discharged path is proposed in this dissertation. Through an exhaustive mathematical derivation in D-Q reference, a backup charge/discharge path is proposed. The reason behind using the D-Q (also called Park and Clark Transform) is to:

1. Reduce the system mathematical complexity by transforming the grid voltage and current into a synchronous rotational frame so that all the signals are transformed into two-phase DC components.
2. Decouple the PMSG output current into its active and reactive current so that each current can be controlled independently which enable the implementation of a three-way mechanical switch into the proposed design.

The mechanical discharge path is a combination of the three-way mechanical switch and a PI controller that takes as input an error signal, which emanates from a reference and a desired DC voltage. In addition, the same three-way mechanical switch can be used to recharge the FESS once the system's normal operational conditions are restored. The FESS mathematical derivation is presented in Chapter 3. In Chapter 4, the derivation is simulated and validated using MATLAB Simscape package. This part of the dissertation addresses the critical redundancy factors in military conditions (such as if the automation control or logic fails during operation). Furthermore, through this work, future and more reliable FESS systems can effectively be developed and proposed.

For the MVDC system, in response to the high inclination of the US Navy adopting DC distribution systems for future state-of-the-art fleets, the DC-link voltage is used as a distribution bus system that feeds a DC grid instead of a machine/flywheel assembly. The system has been simulated using MATLAB Simscape package. Through the DC-link distribution bus, a comprehensive study on various types of plausible shipboard MVDC system dynamic faults and disturbance behaviors have been observed and discussed. In Chapter 4, different combinations of the system short circuit to ground are carried out. Furthermore, a PPL disturbance with and without system dynamic fault (s) was also analyzed. Some of the key findings are:

1. The combination of positive and negative buses to ground carries a more severe disturbance than solely a positive or a negative bus to ground.
2. When a PPL coexists with short-circuit faults on the same DC-link distribution system, the system dynamic transient disturbance mimics the short-circuit behaviors.
3. The DC current dynamic fault transient of the short-circuit fault is almost identical to the PPL disturbance without a fault current transient. This is the most important finding that was unaddressed in the literature but resolved in this dissertation.

Based on these findings, a novel communications-based overcurrent fault protection controller was developed and proposed. The proposed protection controller algorithm aims to distinguish between system dynamic faults and transient bus disturbances such as PPL. It is worth mentioning that MVDC systems are currently still under development, but until recently, no standard protection system had been implemented in AC systems. The proposed fault protection system is simulated using MATLAB Simscape package. The system performance and validation are presented and discussed in Chapter 5.

6.2 FUTURE WORK

It was shown in this dissertation that a DC-link voltage can be used to supply a FESS and a DC distribution system. Both systems are key components of an integrated shipboard power system. However, improvement of the power quality vulnerability on the system stability should be an ongoing battle. For this reason, further analysis should include the following:

1. Developing a simulation and or an experimental shipboard distribution system that integrated both the developed alternate and auto power sag correction systems. The new system can be tested for dynamic PPL and short-circuit fault disturbance. Furthermore, a

consideration should be given at the time delay it will take each system to correct the power sag. An anticipated higher trip time delay can be attributed to the manual discharge because it requires manpower to flip a switch, and there is also the time delay it will take the switch to close and send the signal.

2. Developing a simulation and or an experiment shipboard MVDC system that integrate an alternate and or auto FESS. The performance of the distribution system can be tested following the steps used in Chapter 3 and 4. Proposing a fault protection system such as the technique developed in Chapter 5 can be considered. Improvements on the available fault protection and voltage sag correction systems can be made by merging both issues on the same platform.
3. A global communication dependent backup protection can be added to improve the proposed controller. In case of the proposed system failure during a short-circuit fault, the communication dependent global controller can trigger a trip. Furthermore, Artificial or Computation Intelligence (ACI) can also be used to improve the robustness of the proposed protection controller (but at the cost of slower system response, which is due to complexities related to ACI and memory requirement).

REFERENCES

[1] T. Ericsen., "The ship power electronic revolution: Issues and answer," *55th IEEE Petroleum and Chemical Industry Technical Conference,* Sept.2008, pp 1-11.

[2] Sitzman, A *et al.* Surls, D *et al.* Mallick, J. "Modification and Testing of a Battery Inductor Repetitive Pulsed Power Supply for a Small Rail gun," *Plasma Science, IEEE 34th International Conference*, pp. 1014-1014, 2007.

[3] M. C. Such and C. Hill, "Battery energy storage and wind energy integrated into the Smart Grid," 2012 *IEEE PES Innovative Smart Grid Technologies (ISGT)*, 2012, pp. 1-4, doi: 10.1109/ISGT.2012.6175772.

[4] M.Y, El-Shark, "*A* Fuzzy Evolutionary Programming-Based Methodology for Maintenance of Generation and Transmission Systems,*" Tuscaloosa: University of Alabama* 2002.

[5] G. F. Reed, B. M. Grainger, A. R. Sparacino, E. J. Taylor, M. J. Korytowski, Z. H. Mao, "Medium Voltage DC Technology Developments, Applications, and Trends," University *of Pittsburgh US.*

[6] A. Sanchez-Ruiz, J. J. Valera-García, I. Legarra, I. Torre, S. Telleria and I. Atutxa, "Modeling of MVDC Multidrive Systems for Power Quality Analysis," *IEEE Transactions on Industrial Electronics*, vol. 68, no. 7, pp. 5507-5516, July 2021, doi: 10.1109/TIE.2020.2996143.

[7] Naval Sea Systems Command (1998), Naval *Ship Technical Manual Chapter 320, Electric Power Distribution Systems,* S9086-KY-SMT-010/CH-320R2, 21 April 1998.

[8] U. Agarwal, N. Jain, M. Kumawat and J. K. Maherchandani, "Weibull Distribution Based Reliability Analysis of Radial Distribution System with Aging Effect of Transformer," 2020 *21st National Power Systems Conference (NPSC),* 2020, pp. 1-6, doi: 10.1109/NPSC49263.2020.9331850.

[9] Q. Yu, *et al.* N.N Schuz, *et al.* A.k, Srivastava, "Multi-agent Based Reconfiguration of AC-DC Shipboard distribution Power System," *IOS Press* 17, pp. 347-357, 2010.

[10] A. Sitzman, D. Surls, and J. Mallick, "Modification and testing of a battery-inductor repetitive pulsed power supply for a small railgun," *IEEE 34th International Conference on Plasma Science (ICOPS),* pp. 1014–1014 June 2007.

[11] M. C. Such and C. Hill, "Battery energy storage and wind energy integrated into the smart grid," *IEEE PES Innovative Smart Grid Technologies (ISGT),* pp. 1–4, Jan 2012.

[12] In-Wha Jeong, Jong-Soo Kim, G. I. Gusev, and Geun-Hie Rim, "Design of 35 kJ/s 25 kV capacitor charging power supply for pulsed power systems," *in 30th Annual Conference of IEEE Industrial Electronics Society,* 2004. IECON 2004, vol. 3, pp. 2860–2863 Nov 2004.

[13] K. Gong, J. Shi, Y. Liu, Z. Wang, L. Ren, and Y. Zhang, “Application of smes in the microgrid based on fuzzy control,” *IEEE Transactions on Applied Superconductivity,* vol. 26, no. 3, pp. 1–5, April 2016.

[14] M. I. Daoud, A. S. Abdel-Khalik, A. Massoud, S. Ahmed, and N. H. Abbasy, “On the development of flywheel storage systems for power system applications: A survey,” *International Conference on Electrical Machines,* pp. 2119–2125 Sep. 2012.

[15] S. Kulkarni and S. Santoso, “Impact of pulse loads on electric ship power system: With and without flywheel energy storage systems,” *IEEE Electric Ship Technologies Symposium*, pp. 568–573, April 2009.

[16] E. Dierks, I. R. McNab, J. A. Mallick, and S. Fish, “Battery–inductor parametric system analysis for electromagnetic guns,” *IEEE Transactions on Plasma Science*, vol. 39, no. 1, pp. 268–274, Jan 2011.

[17] A. T. Adediran, H. Xiao and K.L. Butler, “Fault Studies of an U.S. Naval Shipboard Power System,” *NAPS, Univerity of Waterloo, Canada,* pp 1-18 to 1-25, October 2000.

[18] G. Genta, “Energy Storage: Theory and Practice of Advanced Flywheel Systems,” *Butterworth Heinemann Ltd. London, UK*, 1985.

[19] A P. R. S. Shelke, D. G. Dighole, “A Review paper on Dual Mass Flywheel system,” *Int. J. Sci. Eng. Technol.* Res. 5, pp. 326-331 2016.

[20] A. Ruddell, "Investigation on Storage Technologies for Intermittent Renewable Energies: Evaluation and recommended R&D strategy, INVESTIRE Network, ST6 Flywheel Report", *CCLRC-Rutherford Appleton Laboratory,* Didcot, UK, June 2003.

[21] Z. Guo, X. Mu, Z. Bai, B. Cao, “Research on the control of flywheel battery*”. J. Appl. Sci. 7*, pp. 3312–3316, 2007.

[22] Q. Guo, C. Huang, Z. Xue, Y. Yin, W. Liang and X. Sheng, "Research on Energy Storage System Participation in Primary Frequency Regulation of Large-scale Wind Turbines," 2019 *1st International Conference on Industrial Artificial Intelligence (IAI)*, 2019, pp. 1-6, doi: 10.1109/ICIAI.2019.8850837.

[23] Kuo-Chi Lin, Jihua Gou, Chan Ham, S. Helkin and Young Hoon Joo, "Flywheel energy storage system with functionally gradient nanocomposite rotor," 2010 *5th IEEE Conference on Industrial Electronics and Applications*, 2010, pp. 611-613, doi: 10.1109/ICIEA.2010.5517040.

[24] K. Wei, X. Dai and P. Liu, "Model and balance of flywheel energy storage system with composite flywheel and rolling bearings," 2017 *IEEE Conference on Energy Internet and Energy System Integration (EI2)*, 2017, pp. 1-6, doi: 10.1109/EI2.2017.8245342.

[25] E. A. Kuschenko, E. P. Kurbatova, T. A. Zolotarev and M. A. Sysoev, "Magnetic Bearing with HTS Tapes for Flywheel Energy Storage System," 2021 *3rd International Youth Conference on Radio Electronics, Electrical and Power Engineering (REEPE)*, 2021, pp. 1-4, doi: 10.1109/REEPE51337.2021.9388062.

[26] L. Zhen, S. Miao, Y. Zhou and Z. Guo, "Bearingless high temperature superconducting flywheel energy storage system," 2019 *IEEE Sustainable Power and Energy Conference (iSPEC)*, 2019, pp. 1227-1232, doi: 10.1109/iSPEC48194.2019.8974851.

[27] "EPRI-DOE Handbook of Energy Storage for Transmission & Distribution Applications," *Final Report, Cosponsor, U. S. Department of Energy,* December 2000.

[28] G. Cimuca, S. Breban, M. M. Radulescu, C. Saudemont, B. Robyns, "Design and Control Strategies of an Induction-Machine-Based Flywheel Energy Storage System Associated to a Variable-Speed Wind Generator," *IEEE Transactions Energy Conversion,* vol.25, no.2, pp. 526-534, June 2010.

[29] J.G. De Oliveira, “Power Control Systems in a Flywheel based All-Electric Driveline,” Ph.D. *Thesis,* Uppsala Universitet, Uppsala, Sweden, 2011.

[30] V. Kale, M. Secanell, “A comparative study between optimal metal and composite rotors for flywheel energy storage systems,” *Energy Reports*, Vol. 4, pp. 576 – 585, November 2018.

[31] R. Pena-Alzola, R. Sebastián, J. Quesada, A. Colmenar, “Review of Flywheel based Energy Storage Systems,” *In Proceedings of the 2011 International Conference on Power Engineering, Energy and Electrical Drives,* Malaga, Spain, pp. 11–13 May 2011.

[32] M. E. Amiryar, K. R. Pullen “A Reiveiw of Flywheel Energy Storage System Technologies and Their Applications” *School of Math., Comp. Sci. and Eng*., University of London EC1V 0HB, UK March 2017.

[33] H. Darrelmann, "Comparison of high-power short time flywheel storage systems," *Telecommunication Energy Conference,* 1999.

[34] D. Cross, J. Hilton," High Speed Flywheel Based Hybrid Systems for Low Carbon Vehicles," *Flybrid Systems LLP, Silverstone Technology Park, Silverstone Circuit, Northants, NN12 8GX,* UK. *(www.flybridsystems.com)*.

[35] M. I. Daoud, A. S. Abdel-Khalik, A. Massoud, S. Ahmed, N. H. Abbasy, “On The Development Of Flywheel Storage Systems For Power System Applications: A Survey,” *In Proceedings of the 20th International Conference on Electrical Machines (ICEM),* Marseille, France; pp. 2119–2125, 2–5 September 2012.

[36] T. Siostrzonek, S. Pirog, M. Baszynski, "Energy storage systems the flywheel energy storage," *Power Electronics and Motion Control Conference, 2008. EPE-PEMC 2008. 13th*, vol., no., pp. 1779-1783, 1-3 Sept. 2008.

[37] S. Samineni, B. K. Johnson, H. L. Hess & J. D. Law, "Modeling and Analysis of a Flywheel Energy Storage System with a Power Converter Interface," *International Conference on Power Systems Transients-IPST in* New Orleans, USA 2003.

[38] T. Greigarn, M. Garcia-Sanz, "Control of Flywheel Energy Storage Systems for wind farm power fluctuation mitigation," *Energytech, 2011 IEEE,* vol., no., pp.1-6, 25-26 May 2011.

[39] S. R. Holm, H. Polinder & J. A. Ferreira, "Analytical Modeling of a Permanent-Magnet Synchronous Machine in a Flywheel," *IEEE Transactions Magnetics,* vol.43, no.5, pp.1955-1967, May 2007.

[40] J. G Oliveira, A. Larsson & H. Bernhoff, "Controlling a permanent magnet motor using PWM converter in flywheel energy storage systems," *Industrial Electronics, 2008. IECON 2008. 34th Annual Conference of IEEE,* vol., no., pp. 3364-3369, 10-13 Nov. 2008.

[41] J. Lv, X. Jiang and G. Gong, "A Novel Flywheel Array Energy Storage System with DC Series Connection," IECON 2020 *the 46th Annual Conference of the IEEE Industrial Electronics Society,* 2020, pp. 1740-1743, doi: 10.1109/IECON43393.2020.9254641.

[42] J. B. Wu, J. Y. Wen, H. S. Sun, & S. J. Cheng, "Research on dynamic operation characteristics of a doubly-fed induction machine with a flywheel energy storage system," *Sustainable Power Generation and Supply, 2009. SUPERGEN '09. International Conference on,* vol., no., pp. 1-6, 6-7 April 2009.

[43] H. A. Gabbar, A. M. Othman, F. Pino and M. Repetto, "Improved Performance of Flywheel Fast Charging System (FFCS) Using Enhanced Artificial Immune System (EAIS)," *in IEEE Systems Journal*, vol. 14, no. 1, pp. 824-831, March 2020, doi: 10.1109/JSYST.2019.2892002.

[44] P. Cheetham et al., "High Temperature Superconducting Power Cables for MVDC Power Systems of Navy Ships," 2019 *IEEE Electric Ship Technologies Symposium (ESTS)*, 2019, pp. 548-555, doi: 10.1109/ESTS.2019.8847830.

[45] E. C. Mathew and A. Das, "Integration of renewable energy sources with MVDC network," 2020 *IEEE International Conference on Power Electronics, Drives and Energy Systems (PEDES)*, 2020, pp. 1-6, doi: 10.1109/PEDES49360.2020.9379756.

[46] D. Salomonsson, L. Soder, and A. Sannino, "Protection of low-voltage DC microgrids," *IEEE Transactions on Power Delivery*, vol. 24, no. 3, pp. 1045-1053, July 2009.

[47] R. Cuzner and G. Venkataramanan, "The status of DC micro-grid protection," *Industry Applications Society Annual Meeting,* pp. 1–8, 5-9 Oct. 2008.

[48] N. Doerry, 'Next Generation Integrated Power Systems for the Future Fleet', *Corbin A. McNeill Symposium,* United States Naval Academy. Annapolis, 2009.

[49] Q. Deng, “Fault Protection in DC Microgrids Based on Autonomous Operation of All Components,” *Doctoral dissertation, University of South Carolina,* 2017.

[50] U. Javaid, F. D. Freijedo, D. Dujic and W. van der Merwe, "MVDC supply technologies for marine electrical distribution systems," *in CPSS Transactions on Power Electronics and Applications*, vol. 3, no. 1, pp. 65-76, March 2018, doi: 10.24295/CPSSTPEA.2018.00007.

[51] U. Javaid, F. D. Freijedo, D. Dujic, & W. V. D. Merwe, “MVDC Supply Technologies for Marine Electrical Distribution Systems,” *CPSS Trans. On Power Electronics and Applications,* Vol. 3, No. 1, March 2018.

[52] N. H. Doerry and K. McCoy, “Next generation integrated power system: NGIPS technology development roadmap,” *Tech. Rep.,* 2007.

[53] J. D. Park, J. Candelaria, L. Ma and K. Dunn, “DC Ring-Bus Microgrid Fault Protection and Identification of Fault Location,” *IEEE Transactions on Power Delivery,* vol. 28, no. 4, pp. 2574-2584, October 2013.

[54] Z. Li and L. Ren, "Current-Limiting Performance of Three Types of SFCL in Shipboard MVDC IPS," 2020 *IEEE International Conference on Applied Superconductivity and Electromagnetic Devices (ASEMD)*, 2020, pp. 1-2, doi: 10.1109/ASEMD49065.2020.9276156.

[55] J. D. Park, J. Candelaria, L. Ma and K. Dunn, “DC Ring-Bus Microgrid Fault Protection and Identification of Fault Location,” *IEEE Transactions on Power Delivery*, vol. 28, no. 4, pp. 2574-2584, October 2013.

[56] ABB circuit breakers for direct current applications, *ABB,* 2010.

[57] P. S. Moses and J. N. Jiang, "Fault Dynamics in a Multi-Generator MVDC Marine Power System Architecture," 2018 *IEEE Power & Energy Society General Meeting (PESGM*), 2018, pp. 1-5, doi: 10.1109/PESGM.2018.8586549.

[58] NFPA 70E, Standard for Electrical Safety in the Workplace, 2012 Edition.

[59] CSA Standard Z462-12, Workplace Electrical Safety, January 2012.

[60] J. Yuventi, "DC Electric Arc-Flash Hazard-Risk Evaluations for Photovoltaic Systems*," IEEE Transactions on Power Delivery*, vol. 29, no. 1, pp. 161-167, Feb. 2014, doi: 10.1109/TPWRD.2013.2289921.

[61] A. D. Stokes and W. T. Oppenlander, “Electric arcs in open air,” *J. Phys. D, Appl. Phys.*, vol. 24, no. 1, pp. 26–35, Jan. 1991.

[62] C. Yuan, M. A. Haj-ahmed, & M. S. Illindala, “Protection Strategies for Medium-Voltage Direct-Current Microgrid at a Remote Area Mine Site,” *IEEE Trans. On Industry Applications,* vol. 51, no. 4 July/AUG. 2015.

[63] M. E. Baran, S. Teleke and S. Bhattacharya, "Overcurrent Protection in DC Zonal Shipboard Power Systems using Solid State Protection Devices," 2007 *IEEE Electric Ship Technologies Symposium*, 2007, pp. 221-224, doi: 10.1109/ESTS.2007.372089.

[64] X. Lin, F. Zhao, G. Wu, Z. Li and H. Weng, "Universal Wavefront Positioning Correction Method on Traveling-Wave-Based Fault-Location Algorithms," *IEEE Transactions on Power Delivery*, vol. 27, no. 3, pp. 1601-1610, July 2012, doi: 10.1109/TPWRD.2012.2190108.

[65] Q. Li, J. Liang, “Design Issues and Practical Application Challenges of DC Shipboard Distribution System Protection,” *Electric Ship Technologies Symposium (ESTS), 2015 IEEE,* pp. 403-408, 21-24 June 2015.

[66] P. Jafarian and M. Sanaye-Pasand, “A traveling-wave-based protection technique using wavelet/PCA analysis,” *IEEE Transactions on Power Delivery,* vol.25, no. 2, pp. 588–599, Apr. 2010.109.

[67] T. Takagi, Y. Yamakoshi, M. Yamaura, R. Kondow, and T. Matsushima, “Development of a new type fault locator using the one-terminal voltage and current data,” *IEEE Transactions on Power Application Systems,* vol. PAS-101, no. 8, pp. 2892–2898, Aug. 1982.

[68] M. Alamuti, H. Nouri, R. Ciric, and V. Terzija, “Intermittent fault location in distribution feeders,” *IEEE Transactions 0n Power Delivery,* vol. 27, no. 1, pp. 96–103, Jan. 2012.

[69] C. Apostolopoulos and G. Korres, “A novel algorithm for locating faults on transposed/untransposed transmission lines without utilizing line parameters,” *IEEE Transactions on Power Delivery*, vol. 25, no. 4, pp. 2328–2338, Oct. 2010.

[70] Y. H. Lin, C. W. Liu and C. S. Chen, “A new PMU-based fault detection/location technique for transmission lines with consideration of arcing fault discrimination—Part II: Performance evaluation*,” IEEE Transactions on Power Delivery*, vol. 19, no. 4, pp. 1594–1601, Oct. 2004.

[71] J. Shi, R. Amgai, S. Abdelwahed, “Modelling of shipboard medium-voltage direct current system for system level dynamic analysis,” *IET* doi:10.1049/iet-est.2014.0033.

[72] M. Monadi, C. Gavriluta, A. Luna, J. I. Candela and P. Rodriguez, "Centralized Protection Strategy for Medium Voltage DC Microgrids," *IEEE Transactions on Power Delivery,* vol. 32, no. 1, pp. 430-440, Feb. 2017, doi: 10.1109/TPWRD.2016.2600278.

[73] L. Tang & B. T. Ooi, “Locating and Isolating DC Faults in Multi-Terminal DC Systems,” *IEEE Transactions on Power Delivery,* vol. 22, no. 3, July 2007.

[74] H. Ravinda, M. Stanovich, M Steurer, "Documentation for a Notional Two Zone Medium Voltage DC Shipboard Power System Model implemented on the RTDS™," *Center for Advanced Power Systems FSU* www.esrdc.com, December 2016.

[75] RTDS™ User Manual, *RTD Embedded Technologies, inc.*, 2017.

[76] N. Doerry and J. Amy, Jr, "MVDC Shipboard Power System Considerations for Electromagnetic Railguns," *in Proceedings of the DoD Electromagnetic Railgun Workshop,* Laurel, MD, Sep. 2015.

[77] "IEEE Recommended Practice for 1 kV to 35 kV Medium-Voltage DC Power Systems on Ships," *IEEE Std 1709-2010*, vol., no., pp. 1-54, 2 Nov. 2010, doi: 10.1109/IEEESTD.2010.5623440.

[78] *https://relaytraining.com/what-is-dc-offset-ask-chris/*

[79] IEEE Guide for Performing Arc-Flash Hazard Calculations, *IEEE Standard 1584-2002*, *IEEE*, 2002.

[80] A. P. Strom, "Long 60-cycle arcs in air," *Trans. Amer. Inst. Elect. Eng*., vol. 65, pp. 113–117, 1946.

[81] J. Paukert, "The arc voltage and arc resistance of LV fault arcs," *in Proc.7th Int. Symp. Switching Arc Phenom.* pp. 49–51, 1993.

[82] H. Mirzaee, S. Dutta and S. Bhattacharya, "A medium-voltage DC (MVDC) with series active injection for shipboard power system applications," 2010 *IEEE Energy Conversion Congress and Exposition*, 2010, pp. 2865-2870, doi: 10.1109/ECCE.2010.5618184.

[83] C. Heinrich and H. Schmitt, "Integration of new switching technologies in medium-voltage systems," *16th International Conference and Exhibition on Electricity Distribution, 2001. Part 1: Contributions. CIRED. (IEE Conf. Publ No. 482)*, 2001, pp. 5 pp. vol.5-, doi: 10.1049/cp: 20010866.

[84] Y. G. Paithankar and S. R. Bhide "Fundamentals of power system protection," *Prentice-Hall of India Pvt. Ltd*, 2004.

[85] *IEEE standard for inverse-time characteristics equation for overcurrent relays in IEEE std C37.112-2018 (Revision of IEEE std C37.112-1996), vol., no.,* pp. 1-25, 5Feb. 2019, doi:10.1109/IEEESTD.2019.8635630

[86] A. Tjahjono et al., "Modeling Characteristic Curves of Digital Overcurrent Relay (DOCR) for User-Defined Characteristic Curve Using Artificial Neural Network," 2016 *International Conference on Computational Science and Computational Intelligence (CSCI)*, 2016, pp. 478-483, doi: 10.1109/CSCI.2016.0097.

[87] J. M. Thomas, “Naval power and energy development road map,” 2019, *https://www.navsea.navy.mil/Portals/103/Documents/2019_NPES_TDR_Distribution_A_Approved_Final.pdf?ver=2019-06-26-132556-223*.

VITA

Marounfa Djibo

231 Kaufman Hall
ECE Department
Old Dominion University
Norfolk, VA 23529

Education

2021	Ph.D.	Electrical and Computer Engineering	Old Dominion University, Norfolk, VA
2013	M.A.	Electrical and Computer Engineering	University of South Alabama, Mobile, AL
2010	B.S.	Electrical and Computer Engineering	University of South Alabama, Mobile, AL

Selected Peer Reviewed Publication

1. M. Djibo, P. S. Moses, I. Flory, "Fault Protection Considerations for MVDC Shipboard Power Systems Operating with Pulsed-Power Loads," *WEAS Journal,* 2021

Selected Publications & Research

1. M. Djibo and P. Moses, "Integration of Energy Storage and Pulsed-Power Technologies in Shipboard Power Systems," 2020 *Intermountain Engineering, Technology and Computing (IETC)*, 2020, pp. 1-6, doi: 10.1109/IETC47856.2020.9249091.
2. M. Djibo, "Protection and Disturbance Mitigation of Next Generation Shipboard Power Systems," *Old Dominion University, Norfolk, VA*, 2021 (In Progress)
3. P. S. Moses, M. Djibo, J. N. Jiang, and E. Kevric, "Microgrid experiences in marine power and energy systems: stability issues in power electronic interfaces," *in Proc. 2017 50th Frontiers of Power Conference, Stillwater*, Oklahoma, 2017
4. M. Djibo, P. Moses, "Integration Flywheel Energy Storage System and Pulsed-Power Load in Shipboard Power System," (Under review)
5. M. Djibo, P. Moses, "Review on Shipboard Power System Components," (Under review)
6. M. Djibo, Thesis: "Electric Maintenance Scheduling Using Fuzzy-Immune System," *University of South Alabama*, Mobile, AL, 2013

Employment History

Newport News Shipbuilding: Electrical Test Engineer, (2012 to Present)
United States National Guard: Non-Commission Officer, 91D (2011 to 2017)
University of South Alabama: Teacher Assistant, (2010 to 2012)

Professional Experience

Lead Electrical Test Engineer (2017 to Present):

1. Ford Class Aircraft Carrier Steam Driven Main Turbine Generator (MTG)
2. Ford Class Aircraft Carrier Electric Diesel Generator (EDG)
3. Ford Class Aircraft Carrier Main Propulsion Unit (MPU)

Electrical Test Engineer (2012 to 2017):

1. Ford Class Aircraft Carrier Propulsion Plant Monitoring and Control (PPMC)

Research Interests:

1. Flywheel Energy Storage System (FESS)
2. Medium Voltage Direct Current (MVDC) Platform Protection and Disturbance Mitigation
3. Power Plant Generators Maintenance Scheduling